NOVA SCHOOL OF SCIENCE & TECHNOLOGY

DEPARTMENT OF PHYSICS

JOSÉ EMANUEL SANTOS BRITO

BSc in Biomedical Engineering

COMPOSITE CRYOGEL FOAMS OF HYDROXY-APATITE NANOWIRES, β-TCP NANOPARTICLES AND CELLULOSE NANOFIBERS FOR BONE REGENERATION

MASTER IN BIOMEDICAL ENGINEERING

NOVA University Lisbon

September, 2024

NOVA SCHOOL OF SCIENCE & TECHNOLOGY

DEPARTAMENT OF PHYSICS

COMPOSITE CRYOGEL FOAMS OF HYDROXYAPATITE NANOWIRES, β-TCP NANOPARTICLES AND CELLULOSE NANOFIBERS FOR BONE REGENERATION

JOSÉ EMANUEL SANTOS BRITO

BSc in Biomedical Engineering

Adviser: Maria do Carmo Henriques Lança, PhD
Assistant Professor, NOVA University Lisbon

Co-advisers: Marta Cristina Parracho Cançado Corvo, PhD
Principal Researcher at the Department of Materials Science, NOVA University Lisbon

Examination Committee:

Chair: Susana Isabel dos Santos Silva Sério Venceslau, PhD

Rapporteurs: Susete Maria Brazão Nogueira Fernandes, PhD

Adviser: Maria do Carmo Henriques Lança, PhD
Assistant Professor, NOVA University Lisbon

Members: Marta Cristina Parracho Cançado Corvo, PhD
Principal Researcher at the Department of Materials Science, NOVA University Lisbon

MASTER IN BIOMEDICAL ENGINEERING

NOVA University Lisbon
September, 2024

Composite cryogel foams of hydroxyapatite nanowires, β-TCP nanoparticles and cellulose nanofibers for bone regeneration

ACKNOWLEDGMENTS

The completion of this significant phase, represented by my master's dissertation, only became a reality thanks to the support and collaboration of many people. Therefore, I express my deepest gratitude to everyone who contributed to helping me reach this point.

Firstly, I would like to thank not only my supervisor, Carmo Lança, but also my co-supervisor, Marta Corvo, for guiding me throughout this long journey, challenging me with suggestions and encouraging me to proceed independently and autonomously, and for always being willing to collaborate whenever necessary to overcome problems.

I would also like to express my gratitude to the departments of Materials, Chemistry, Physics, and CENIMAT, as well as to all the professors and PhD students, especially Maria Morais and Guilherme, for providing not only the necessary equipment and resources but also for assisting me in understanding various protocols and procedures throughout my work.

I extend a word of appreciation to my course and lab colleagues, with special mention to Guilherme and Rodrigo, for keeping me company every day, for the laughs and random conversations that helped ease the stress caused by the thesis.

To my source of extra support, my girlfriend Ana, thank you for always being by my side through the good and bad times, for calming me in moments of panic, and for never stopping believing in me, even when I doubted myself.

Lastly, but certainly not least, a special thank you to my entire family- parents and siblings- for supporting me when I needed it the most, even when I was far from home, for never letting me go without, for not letting me give up when everything seemed impossible, and for believing in my academic abilities until I reached this stage. If there is anyone to whom I owe where I am today, it is to YOU.

“Those who pass by us, do not go alone, and do not leave us alone; they leave a bit of themselves, and take a little of us.” (Antoine de Saint-Exupéry)

ABSTRACT

Bone tissue is a vital component of the human body, providing structural support, protection, and mineral storage, while continuously remodelling to maintain its function. However, in cases of severe damage or disease, the natural regenerative process may be insufficient. The aim of this dissertation focuses on the production of cryogel foams composed by hydroxyapatite nanowires (Hap NW), β-tricalcium phosphate (β-TCP) nanoparticles, and cellulose nanofibers (CNF) for tissue engineering applications.

Hap NW and β-TCP nanoparticles were synthesised using the solvothermal and sol-gel methods, respectively. Subsequently, cryogels were produced from these materials with CNF in different concentrations (mg/mL). The cryogels and their constituents were characterized by SEM, ATR-FTIR, XRD, ICP-OES, and cytotoxicity tests. Additionally, selected cryogels were subjected to bioactivity tests in SBF solution, thermal and structural stability tests, mechanical and porosity/surface area assessments.

The results indicate a uniform distribution of components in the cryogels and non-cytotoxic compositions when using low concentrations of CNF ($\leq$ 2.5 mg/mL) due to the possible absorption of nutrients from the medium, essential for cell survival. There was no evidence of good bioactivity, as no significant variation was observed in the concentration of Ca^{2+} and P^{3-} in the SBF or in the SEM/EDS analyses. DSC-TG results showed that the combination of Hap and β-TCP increased thermal resistance, while CNF compromised its stability. The evidence of macroporosity from the isothermal curves, low Young's modulus (<100 KPa), with variations related to compositions, and low density indicate the presence of a viscoelastic material with flexible and deformable properties, essential for adapting to biological tissues. However, optimizing stiffness, additional tests of biological compatibility, and tissue formation are still required.

Keywords: Bone tissue, bone regeneration, cryogel, hydroxyapatite nanowires, β-TCP, cellulose nanofibers, solvothermal method, sol-gel

RESUMO

O tecido ósseo é um componente vital do corpo humano, fornecendo suporte estrutural, proteção e armazenamento de minerais, enquanto se remodela continuamente para manter a sua função.

No entanto, em casos de danos ou doenças graves, o processo regenerativo natural pode ser insuficiente. O objetivo desta dissertação foca-se na produção de espumas de criogel compostas por nanofios de hidroxiapatite (Hap NW), nanopartículas de β fosfato tricálcico (β-TCP) e nanofibras de celulose (CNF) para aplicação em engenharia de tecidos.

Os Hap NW e as nanopartículas de β-TCP foram sintetizadas pelo método solvotérmico e sol-gel, respetivamente. Seguidamente, foram produzidos criogéis a partir destes materiais com CNF em diferentes concentrações (mg/mL). Os criogéis, e seus constituintes, foram caraterizados por SEM, ATR-FTIR, XRD, ICP-OES e por testes de citotoxicidade. Adicionalmente, os criogéis selecionados foram submetidos a testes de bioatividade em solução de SBF, estabilidade térmica e estrutural, mecânicos e de porosidade/área superficial.

Os resultados indicam uma uniformidade de distribuição dos componentes nos criogeis e composições não citotóxicas aquando do uso de baixas concentrações de CNF (< 2.5 mg/mL) devido à possível absorção de nutrientes do meio, essenciais à sobrevivência celular. Não houve indícios de boa bioatividade por não se verificar variação significativa na concentração de Ca^{2+} e P^{3-} no SBF e no SEM/EDS. Resultados de DSC-TG mostraram que a combinação de Hap e β-TCP aumentou a resistência térmica, enquanto a CNF comprometeu a sua estabilidade. A evidência de macroporosidade pelas curvas isotérmicas, baixo módulo de Young (<100 KPa), com variações relacionadas às composições e baixa densidade indicam a presença de um material viscoelástico com propriedades flexíveis e de deformação essenciais na adaptação aos tecidos biológicos. Contudo, é necessário a otimização da sua rigidez, testes adicionais de compatibilidade biológica e formação de novos tecidos.

Palavras-chave: Tecido ósseo, regeneração óssea, criogel, nanofios de hidroxiapatite, β-TCP, celulose nanofibrilada, método solvotérmico, sol-gel

CONTENTS

LIST OF FIGURES

LIST OF TABLES

ACRONYMS

Hap	Hydroxyapatite
CMC	Carboxymethyl cellulose
TCP	Tricalcium phosphate
β-TCP	β-Tricalcium phosphate
Hap NW	Hydroxyapatite nanowires
α-TCP	α-Tricalcium phosphate
CNC	Cellulose nanocrystalline
CNF	Cellulose nanofibers
CNB	Bacterial nanocellulose
SEM	Scanning electron microscopy
EDS	Energy-dispersive x-ray spectroscopy
XRD	X-ray diffraction
ATR-FTIR	Attenuated Total Reflectance- Fourier transform infrared spectroscopy
ICP-OES	Inductively Coupled Plasma Optical Emission Spectrometer
BET	Brunauer-Emmett-Teller
BJH	Barrett-Joyner-Halenda
DSC	Differential scanning calorimetry
TG	Thermogravimetric analysis
PDMS	Polydimethylsiloxane
ICDD	International Centre for Diffraction Data
SBF	Simulated body fluid
PBS	Phosphate Buffered Saline

IUPAC	International Union of Pure and Applied Chemistry
CAT	Computed Axial Tomography

SYMBOLS

β	Full width at half maximum intensity
κ	Shape factor of the crystallite
τ	Size of the crystalline grains
θ	Degree
Δ	Standard deviation
σ	Experimental standard deviation
λ	Wavelength
ε	Strain
γ	Stress

1

INTRODUCTION

1.1 Bone Tissue Engineering: From Composition to Regenerative Solutions

1.1.1 Bone Tissue

Bone tissue is a specialized type of connective tissue that performs numerous functions of extreme importance in the human body, including mechanical support for locomotion, protection of vital organs, and regulation of mineral homeostasis [1]. In addition, it stands out as the primary storage source of calcium and phosphate, serving as a reservoir for bone marrow [2].

It is a heterogeneous composite material that, from a chemical point of view, consists of 45-60% inorganic minerals, mainly hydroxyapatite (Hap) crystals, $Ca_{10}(PO_4)_6(OH)_2$. These crystals are organized in elongated, rod-like shapes similar to nanowires, contributing for mineral homeostasis and hardness, rigidity, and compressive resistance to bone [3]. It is also important to note the presence of ions such as sodium (Na^+), potassium (K^+), magnesium (Mg^{2+}), fluoride (F^-), chloride (Cl^-), carbonate (CO_3^{2-}), and some trace elements, which provide additional resistance. Bone also contains 20-30% organic materials, predominantly type I collagen (90%), which, as the main structural component of the bone matrix, provides flexibility, resilience and tensile strength, as well as the mediation of cellular adhesion [4]. Hap and collagen work together to maintain a necessary balance in the bones, because while Hap provides rigidity to the bone, collagen allows it to have a certain resilience to tolerate torsions and loads, being neither too flexible nor too fragile [5]. Additionally, bone is also made of non-collagenous proteins (10%), such as growth factors and cytokines, which contribute to matrix mineralization and regulation of osteoclast and osteoblast function. Finally, bone also contains 10-20% of water (H_2O), which ensures flexibility, as well as bioactive factors and cells [2], [6], [7].

Bone exhibits a multiscale structure, differentiating into cortical bone and trabecular (spongy) bone. Cortical bone, located on the surface, contains 99% of the body's calcium (Ca^{2+}) and 90% of its phosphate (PO_4^{3-}), and has a considerable density, with porosity ranging from 5% to 10%, which provides strength and support. In contrast, trabecular bone, located internally, is composed of intertwined lamellar trabeculae containing hematopoietic cells, adipose tissue, and blood vessels. Although it accounts for only 20% of bone weight, its high porosity, ranging from 50% to 90%, and a specific surface

area 20 times greater than that of cortical bone, provide flexibility, shock absorption, and a conductive environment for haematopoiesis [6].

1.1.2 Bone remodelling and regeneration

Bone remodelling is a dynamic and continuous process that occurs in the skeletal system to maintain integrity and adapt bones throughout life. This process requires specialized cells, which includes osteoblasts (form the bone matrix), osteoclasts (resorb bone), osteocytes (maintain bone tissue), and osteogenic cells (stem cells), as seen in Figure 1.1 [2], [8].

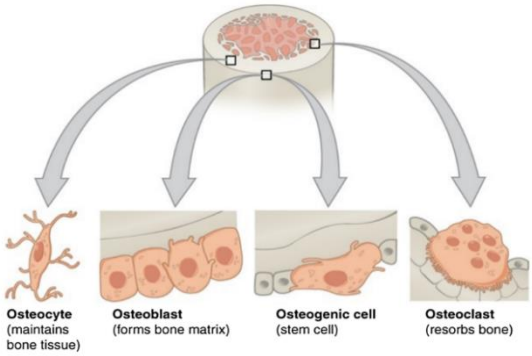

Figure 1.1 - Specialized cells in bone remodelling - osteoblasts, osteoclasts, osteocytes and osteogenic cells. (from Ansari *et al*. (2019) [8]).

This process begins with activation, where osteoclasts are recruited and activated while the lining cells move away from the bone, exposing its surface. Pre-osteoclasts attach to the bone matrix and isolate the area to be resorbed. During the resorption phase, differentiated osteoclasts secrete proteins to dissolve the bone mineral and degrade bone matrix. This stage ends with osteoclast apoptosis, preventing excessive resorption. The newly resorbed bone surface is prepared for the deposition of new bone matrix. Osteoblasts remove the unmineralized collagen matrix, depositing a "cement line" to promote the adhesion of osteoblasts, thus marking the reversal phase. After this step, an osteoid matrix rich in type I collagen is formed, thanks to the osteoblasts that regulate osteoid mineralization. Finally, these osteoblasts undergo apoptosis or differentiate into osteocytes, signalling the end of bone remodelling through the secretion of osteogenesis antagonists [9].

Although bones have the capacity to constantly remodel and repair themselves, in cases of significant bone loss due to hereditary causes, surgery, disease or ageing, this capacity may be insufficient, leading to intense pain, persistent inflammation and structural impairment of the skeleton [2], [7]. In these cases, bone restructuring is essential to promote the growth, proliferation and differentiation of osteoprogenitor cells, ensuring effective repair. For successful bone regeneration, it is crucial to support three key mechanisms: rapid revascularization, induction of osteogenesis and osteoinduction [8].

1.1.3 Bone and Tissue Repairing

One of the most used methods to bridge gaps and replace damaged tissues is the graft implantation, which can restore the normal shape and function of the affected area, However, they can have some limitations, such as potential infections and immune rejection [10].

Tissue engineering has been rebuilding tissues using biocompatible materials to precisely replicate not only the behaviour of biological bone but also the chemical composition and micro and macroscopic architecture, such as scaffolds, polymer-based networks, that offer a promising and effective strategy, particularly in the regeneration of complex and specialized bone and cartilage tissues. Three examples of polymer scaffolds that have shown potential in this area, are cryogels, aerogels and hydrogel [8], [10].

Bone regeneration requires that the biomaterial used provides mechanical support, allows cellular colonization, and supports vascularization. Aerogels are extremely lightweight materials characterized by a solid porous network with nanometric-sized pores (typically less than 100 nm) [11]. Hydrogels are formed by three-dimensional polymeric networks that can absorb large amounts of water, providing a hydrophilic environment. Cryogels have also a porous network but have larger and interconnected pores ranging from 100 to 300 μm, that compared to aerogels and hydrogels, facilitates cellular infiltration and vascularization, which in turn promotes nutrient exchange and blood vessel formation within the material, a crucial point for osteogenesis [12]. Besides that, cryogels also have a pore size more similar to the one considered suitable for bone tissue formation (between 200 and 400 μm) [10], [13], [14].

Additionally, aerogels tend to be more rigid and fragile, since a higher porosity tends to decrease mechanical resistance, which poses as a limitation for their use in biological environments, as they break under pressure. Hydrogels, on the other hand, exhibit high biocompatibility and are therefore commonly used as scaffolds, but their low rigidity prevents them from supporting bone growth, compromising stability. Nonetheless, cryogels present a better balance, having greater flexibility than aerogels, and being more stable and mechanically rigid than hydrogels. Therefore, they offer support for bone growth without compromising flexibility and the ability to adapt to the surrounding tissue [7], [10], [13], [15].

1.2 Cryogels

1.2.1 State of Art

Cryogels have been studied for over 40 years. In the 1980s, Lozinsky *et al.* established the foundations for the cryogelation process, which involves freezing precursor solutions at sub-zero temperatures to form highly interconnected porous structures. They focused on synthesizing cryogels with various solvents and used advanced imaging techniques to characterize the architecture of these materials [16]. In 1989, Lozinsky *et al.* used a polyvinyl alcohol cryogel to immobilize cells and produce an amino acid derivative, demonstrating the potential of cryogels for cell immobilization and inspiring further research in this area to enhance the production of various biochemically important molecules [17].

Recently, cryogels have emerged as valuable materials in tissue engineering for replacing or regenerating damaged tissues, thanks to their ability to recreate a three-dimensional environment that supports cells with minimal immune rejection. The supermacroporous structure facilitates the transfer of nutrients and gases, supporting cell growth and proliferation [18], [19].

In 2016, Odabas *et al.* designed a cryogel system by integrating collagen with carboxymethyl cellulose (CMC) and tricalcium phosphate (TCP). CMC was selected for its capacity to simulate aggrecan, an extracellular matrix protein that imparts gel-like properties to cartilaginous or membranous bone tissues. In contrast, TCP is incorporated to enhance the mechanical strength of scaffolds and to provide osteoinductive capabilities, which refer to the material's ability to encourage the differentiation of cells into bone tissue. Notably, the inclusion of TCP in the cryogels increased their compressive resistance, however these cryogels still fall short of replicating the mechanical characteristics of native bone and cartilage tissues [20].

Another example was the development of a gelatin cryogel composite reinforced with hydroxyapatite nanowires (Hap NW) by Gu *et al.* (2019). The incorporation of Hap NW into the gelatin increased the compressive strength and elastic modulus, mimicking the characteristics of natural bone. The composite also demonstrated excellent biocompatibility, promoting the adhesion, proliferation, and migration of osteoblast-like cells [21].

In the same year, Ferreira *et al.* developed highly porous cryogels made of nanocellulose and bioactive glass. The incorporation of bioactive glass into nanocellulose enhanced the mechanical properties and bioactivity of the cryogel, promoting the deposition of hydroxyapatite, which is essential for new bone formation. The study demonstrated excellent biocompatibility, osteoblast growth, and stimulation of osteogenic markers critical for bone healing [22].

More recently, in 2024, Wang *et al.* investigated the combination of polylactic acid scaffolds with β-tricalcium phosphate (β-TCP) using 3D printing with liquid crystal display photopolymerization for bone tissue engineering. The study showed improvements in mechanical strength, porosity, biocompatibility, as well as enhanced cell attachment and proliferation [23].

Also in 2024, Zhanbassynova *et al.* developed and characterized biomimetic cryogel scaffolds composed of gelatin and oxidized alginate matrix, enriched with Hap, to promote osteoconduction in biomedical materials intended for tissue engineering applications. These cryogels have shown resistance being suitable for bearing mechanical loads typical of bone tissues, enhanced bioactivity, mineralization and bone integration, excellent biocompatibility, nutrient diffusion, cell adhesion and proliferation. So, this study showed the potential of combining natural biopolymers with additives like hydroxyapatite for the fabrication of customized scaffolds for biomedical applications [24].

1.2.2 Structure, properties and formation process of cryogels

As mentioned before, cryogels are polymer-based networks with a macro-porous and interconnected structure, similar to a sponge, that support cell growth and infiltration, providing more space for cells to inhabit the entire scaffold, facilitate the free flow of nutrients and the removal of metabolic waste throughout the cellular life cycle. Besides that, they have high specific surface area, flexibility and high resistance to compression. Additionally, these materials feature three-dimensional structures that can be hydrophilic, hydrophobic, or amphipathic [10], [25].

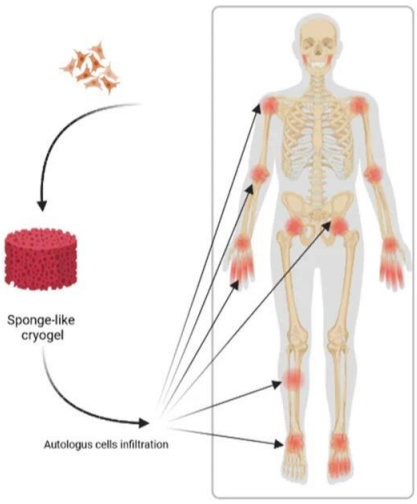

Figure 1.2 - Locations of non-healing bone sites or articular joints were cryogels can be used as scaffold for tissue engineering. (adapted from Carriero *et al.* (2023) [10]).

The cryogelation process (formation of cryogels), that involves a series of steps, is essential to understand pores formation. First, the solution is frozen at temperatures below the solvent's freezing point (typically 10 ºC lower), and then it is kept in the frozen state for a specific period, where the solution remains partly liquid, allowing cross-linking to occur. So, at this stage, solvent forms ice crystals that act as pore-forming agents, and as they grow, they merge with other crystals. Then, the polymeric network solidifies, while expelling the gel precursors into the intercrystalline space. Due to the high pressure created by the growth of the ice crystals, the macropore walls tend to be thin and with low

nano/microporosity. When thawed through sublimation and lyophilization, the ice is removed, creating large, interconnected pores resulting in a flexible porous matrix. The size and connectivity of the pores depend on factors like solvent type, freezing rate, and precursor concentration. This method is versatile and can use various solvents, with water being the most common [12], [19], [25], [26] .

Cryogels can be crosslinked through various methods, resulting in different structures and properties that make them highly suitable for biomedical applications, such as tissue engineering and drug delivery [26]. By adjusting their mechanical and porous properties, they can be used for the replacement or regeneration of damaged tissues, such as fractures or defects in bones and cartilage, as illustrated in Figure 1.2.

1.2.3 Applications of cryogels

Their application focuses on the middle part (diaphysis) and the ends (epiphyses) of long bones, such as the femur and tibia [10]. Raina *et al*. (2016) tested the use of cryogels made of organic/inorganic silk fibroin, chitosan, agarose, bioactive glass, and Hap for the repair of bone defects. A thick layer of cryogels was applied to the outer part of the bone, leading to the formation of new bone in the cortical zone and subsequent progression to the trabecular zone, due to the integration and support, showing excellent biocompatibility [27]. Besides that, cryogels are also applied in craniofacial bones, like mandible and maxilla, as shown in Hixon *et al.* (2017) where cryogels composed of gelatine, Hap, β-TCP were employed in defective rat mandible for 4 weeks, increasing the integration of osteoblasts and osteoclasts, and consequently, the formation of new bone [28]; and in Mishra *et al*. (2014) where a cryogel with polyvinyl alcohol-tetraethylorthosilicate-alginate-calcium oxide was used to repair cranial defects in rats, which demonstrated osteoblast development and consequent bone regeneration [29], [30].

The studies mentioned and other studies have proven the effectiveness of cryogels. Their versatility in modifying cryogel scaffolds with different biomaterials, natural polymers and bioactive molecules to meet specific tissue needs makes them valuable materials in regenerative medicine. Thus, cryogels are expected to continue evolving together with different composites [19].

1.3 Biomaterials used in the composites

This section presents the main biomaterials used in the composites, focusing on their properties, structures, and contributions to enhancing the performance of these materials in bone regeneration and other biomedical applications.

1.3.1 Hydroxyapatite

Hap is an inorganic mineral biomaterial, being chemically defined as a cluster of Ca^{2+} minerals containing phosphate (apatite). It is highly biocompatible, osteoconductive, with non-toxic degradation products (Ca and P) that are absorbable *in vivo* and non-inflammatory in nature, promoting its integration into natural bone and the healing/regeneration process [31]–[36]. Hap bioceramics, commonly used in bone regeneration, are known to have some limitations in fracture toughness, being more fragile when compared to natural bone (which can be confirmed by values in Table 1.1). However, research has

shown that mechanical strength and fracture resistance can be improved significantly by incorporating various materials like carbon fibers, polymers, or other (nano)materials [37].

When compared to other calcium phosphates, Hap is more thermally stable in physiological fluid within a pH range of 4.2 to 8.0. This fact, combined with its low biodegradability, can actually represent a disadvantage in certain applications, such as in cryogels, often requiring it to be combined with other materials. Its hexagonal crystalline structure allows for ionic substitutions of Ca^{2+}, PO_4^{3-}, or hydroxyl ions (OH^-), which affect various parameters such as its crystallinity, solubility and stability. Additionally, Hap is recognized for its stoichiometric Ca/P (calcium/phosphate) ratio of approximately 1.67, which is similar to bone apatite, leading to a higher stability and mechanical strength, the closer the value is to the ratio [34], [38]–[44].

In general, Hap is produced in various one-dimensional nanostructured forms, such as powders, nanoblasts, nanofibers, nanowires, and nanotubes. The versatility of these shapes expands the applications of Hap, as these materials improve the adhesion of osteoblasts, favour their integration, and enhance resorption and bioactivity [45]. When compared to simple Hap produced on a large scale, Hap NW require more complex processes. However, they exhibit better mechanical strength and greater elasticity, due to their ability to form interconnected networks that are less cohesive than powder. Additionally, Hap NW have an extremely high surface area, which allows a better cellular absorption and adhesion, resulting in faster and more effective osteoconduction, and consequently, better integration in bone tissue [46]. Ultralong Hap NW are also characterized by having lengths greater than 100 µm and diameters less than 100 nm, having aspect ratios greater than 1000, which results in high surface activity and an ultrafine structure. They have a morphology similar to Hap in hard human tissues, with high flexibility, toughness, and strength, allowing them to have a porous structure that enables interweaving [36].

In Table 1.1 are presented the main properties of Hap. In Figure 1.3, Hap structure can be observed.

Table 1.1 - Main properties of Hap, depending on the fabrication technique. (adapted from Fiume *et al.* (2021) [44]).

Main Properties of Hap			
Properties	**Value**	**Properties**	**Value**
Density	3.16 g/cm^3	Fracture Hardness	3-7 GPa (dense Hap)
Decomposition Temperature	>1000°C	Tensile Strength	38-300 MPa (dense Hap) 3 MPa (porous Hap)
Dielectric Constant	7.40 – 10.47	Compressive Strength	120-900 MPa (dense Hap) 2-100 MPa (porous Hap)
Thermal Conductivity	0.013 W/cm.K	Young's Elastic Modulus	35-120 GPa
Melting Point	1614°C	Fracture Energy	2.3-20 J/m^2
Bending Strength	38-250 MPa (dense Hap) 2-11 MPa (porous Hap)	Fracture Toughness	0.7-1.2 MPa.m$^{0.5}$ (decrease with porosity)

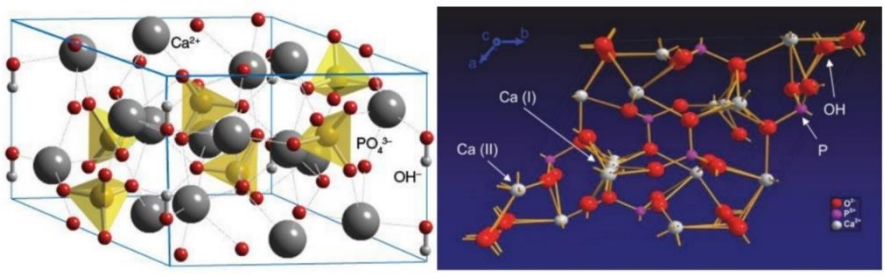

Figure 1.3 - Crystaline Hap structure (from Syafira R.S. *et al.* (2023) [50]).

As previously mentioned, Hap NW have attracted interest due to their properties, being used as coating for orthopaedic prostheses and implants [47], to fill bone defects [48] and for synthetic scaffolds [49].

For that reason, various synthesis techniques have been developed for their production, including the solvothermal method [51], the sol-gel method [52], and the reverse micelle approach [53].

1.3.2 β-tricalcium phosphate

TCP is a brittle inorganic chemical compound that belongs to the calcium phosphate family, with the chemical formula $Ca_3(PO_4)_2$ and, an approximate density of 3.07 g/cm³. In bone regeneration is used in biphasic ceramics, in its β-phase, Hap/β-TCP, to tune the biodegradability rate of the biomaterials. β-TCP has an intragranular porosity of 65% and granule sizes ranging from 150 to 500 μm or between 500 and 1000 μm (according to Choy CS *et al.* (2021) [54]). This results in low mechanical resistance, due to its porous structure, often requiring the combination with other materials to improve its mechanical properties, like metal ions, such as Zn^{2+} that improves resistance, compression and stability, and Mg^{2+} that increases the density and toughness. Besides that, allows proliferation of osteoblastic cells and structural changes in lattice parameters [55].

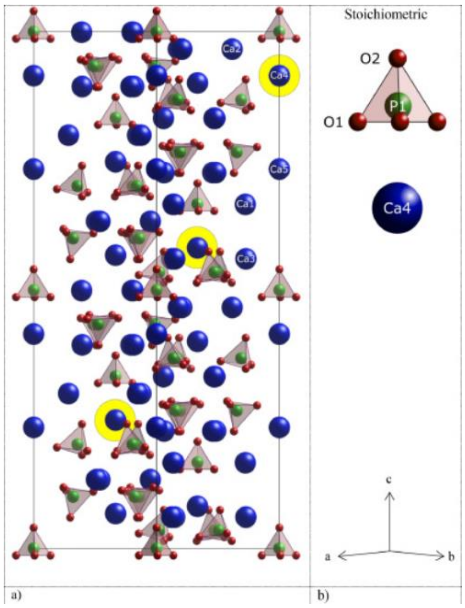

Figure 1.4 - a) β-TCP structure. Colored in blue are Ca^{2+} atoms, in green are P atoms, in red are O atoms. **b) Illustration of the atomic arrangement of Ca_4 and P_1O_4 in the stoichiometric β-TCP crystal model** (adapted from Bohner *et al.* (2020) [62]).

Its chemical composition ensures an ionic balance between the surrounding fluid and the biomaterial. It has a specific crystalline structure composed of two planar domains with different molar Ca/P ratios, one with 1.429 and the other with 1.571, studies confirmed by Matsunaga *et al.* (2015) [56] and Yin *et al*. (2003)[57]. The average Ca/P ratio of 1.5 determines the physical and chemical properties of β-TCP-based scaffolds. When the ratio is close to this value, materials show an effective hardening and controlled degradation, as shown by Vlad *et al.* (2012) [58]. In addition, it indicates an approximation to the natural composition of the bone, showing biocompatibility, as well as a balanced release of calcium and phosphorus ions that are necessary for the formation of new bone tissue, making the material bioactive and facilitating osteoconduction [58].

β-TCP has a rhombohedral structure, containing 273 atoms in a single unit cell, distributed across five calcium, three phosphorus, and ten oxygen sites, as shown in Figure 1.4 [59].This material remains stable at temperatures below 1125 ºC and is the most common form at room temperature. Above this temperature, it transforms into α-Tricalcium phosphate (α-TCP), monoclinic structure, which is thermodynamically less stable at normal temperatures, more disordered, less dense and more reactive, presenting a rapid resorption, degrading before new tissue has sufficiently formed to provide structural support. Furthermore, at 1430°C, α-TCP converts into α′-TCP, which adopts a hexagonal structure [60]. On the other hand, the arrangement of Ca^{2+} and PO_4^{3-} ions in β-TCP facilitates a slower, more controlled resorption and solubility. This is crucial for bone scaffolds, as it allows for gradual degradation while

maintaining structural integrity until it is replaced by natural bone, within 4 to 12 months, as shown by Choy CS *et al.* (2021) [54], [61]. The bone growth occurs within the granules, where the rapid formation of osteoblasts takes place due to the capillary effect of blood [62], [63]. Thus, in the perfect conditions β-TCP is excellent for bone regeneration due to its lack of local or systemic toxicity, its biocompatibility, *in vivo* bioactivity, and its osteoconductive and osteoinductive properties [62], [64].

The characteristics of β-TCP can vary depending on the conditions and the method used for the synthesis. Some examples include solid-state reaction [62], thermal conversion [64], chemical (or aqueous) precipitation [65], co-precipitation [64], and sol-gel [66]–[69].

1.3.3 Cellulose nanofibers

Cellulose is an amphiphilic (has hydrophobic and hydrophilic regions), insoluble polysaccharide polymer with the chemical formula $C_6H_{10}O_5$, that can be extracted from various sources in nature, which can be transformed into nanocellulose through chemical and physical treatments [70]–[72].

Nanocellulose is typically divided into three groups: cellulose nanocrystalline (CNC), obtained solely through acid hydrolysis of cellulose, using commonly sulfuric acid; cellulose nanofibers (CNF), obtained through chemical removal of hemicellulose followed by acid hydrolysis or mechanical treatment, which disaggregates cellulose fibers into nanoscale structures, reducing the amorphous regions (less structured) while preserving the crystalline regions (more ordered and organized); and recently, bacterial nanocellulose (CNB), obtained by biological methods, where a culture of bacteria is used to synthesize cellulose in liquid environments, through the secretion of extracellular cellulose fibers that form a three-dimensional network during fermentation [70], [71], [73]. CNB is highly pure because it has no lignin, hemicellulose or pectin in its composition, which allows it to have a higher degree of polymerization and crystallization. Besides that, is suitable for cell adhesion and immobilization due to its ability to retain water, which resembles that of collagen, being used for wound healing, creation of artificial blood vessels and tissue regeneration, however production costs are very high. CNF has a high specific aspect ratio when compared to rigid CNC, which results in a flexible, strong, and though material that mimics fibrous structure of collagen in bones, crucial for creating scaffolds that can endure mechanical stress. On other hand, CNC, due to its crystalline structure, forms denser and less porous scaffolds, limiting cell infiltration and vascularization, while CNF can form porous and have low density, which is ideal for cell growth and proliferation. Thus, CNF is an excellent material to be used in scaffolds that require flexibility and structural similarity to natural tissues like bone [74]–[76].

In terms of size, CNF is usually less than 100 nm in diameter and several micrometres in length [71], [77]. CNF is formed by crystalline regions contributing to rigidity and elasticity, and amorphous regions contributing to flexibility and plasticity (Figure 1.5). Crystalline domains are less accessible to water, solvents, enzymes, and chemical reagents than amorphous, because of their tightly packed structure that is more difficult to penetrate. In contrast, the loosely organized structure of amorphous regions makes them more accessible and, therefore, more vulnerable to hydrolysis by acids and enzymes. Thus, highly

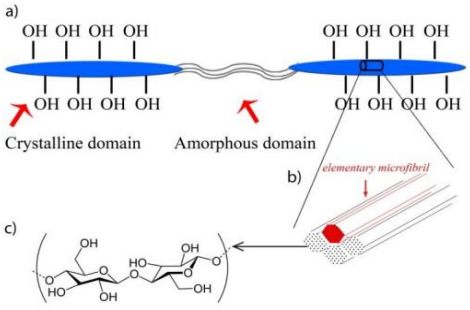

Figure 1.5 - a) Crystalline and amorphous domains of CNF. b) Microfibrils of cellulose. c) Cellulose structure. (from Song *et al.* (2014) [78])

crystalline regions are more resistant and less prone to breakdown [77], [78]. Additionally, the fibrils have a large surface area, a small weight, and contains hydroxyl (-OH) groups that are highly and prone to forming hydrogen bonds. CNF interact with other molecules and with each other, mainly through hydrogen bonds and van der Waals forces. These interactions lead to the formation of an interconnected network, that is supported by their low thermal expansion coefficient and high surface modification capability, offering excellent mechanical properties, as viscoelasticity [79].

All those advantages, as well as the high surface modification capability and biodegradability of CNF, raise its interest, mainly in bone tissue regeneration due to its ability to mimic the extracellular matrix and promote osteogenesis [77].

The presence of hydrogen bonds in the structure of CNF enables its utilization either independently or in conjunction with other polymeric materials. However, when self-assembled, it presents issues with hydrophilicity and poor osteoconduction, which are improved when combined with various organic or inorganic compounds [70].

1.4 Objectives

The main objective of this dissertation was the production of Hap NW composite cryogels incorporating β-TCP nanoparticles and CNF to enhance their properties for biomedical applications in bone tissue regeneration.

In order to evaluate each of the cryogel components individually and the cryogels themselves, different types of characterisations were carried out, according to the diagram in Figure 1.6, where is also described the function of each one.

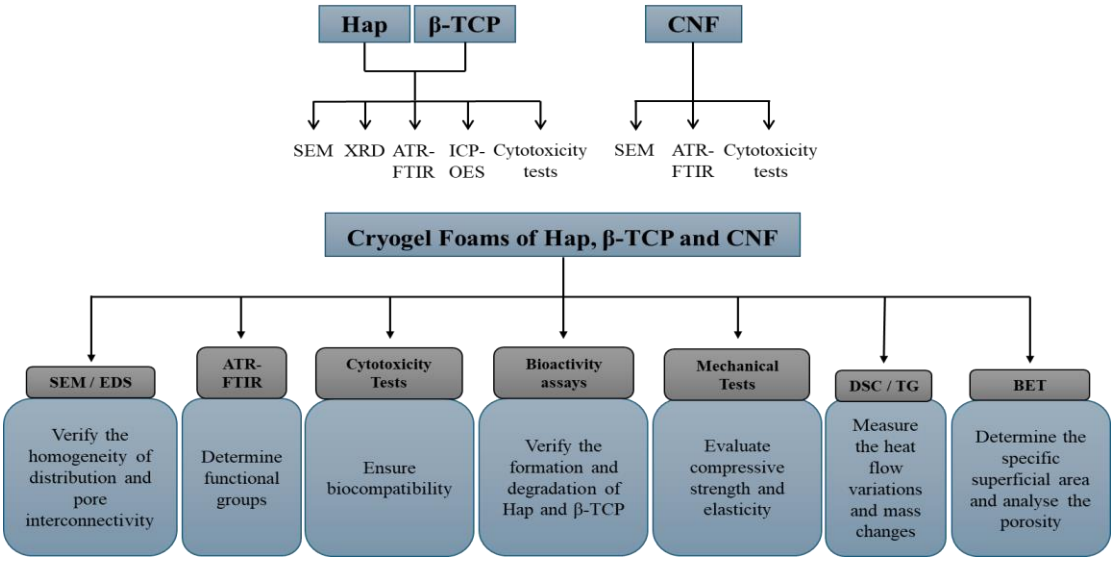

Figure 1.6 - Diagram of different assays performed for the components and the cryogels. SEM/EDS: Scanning Electron Microscopy/ Energy-dispersive X-ray Spectroscopy; XRD: X-ray Diffraction; ATR-FTIR: Attenuated Total Reflectance -Fourier-transform Infrared Spectroscopy; ICP-OES: Inductively Coupled Plasma Optical Emission Spectrometer; DSC-TG: Differential Scanning Calorimetry - Thermogravimetric Analysis; BET: Brunauer-Emmett-Teller

Thus, the studies conducted throughout this dissertation aimed to develop an optimised material that served as a foundation for future investigations about cryogels incorporating other additives or modified properties to improve bone regeneration in advanced clinical contexts.

2

MATERIALS AND METHODS

All the reagents and equipment information can be found in section A.1.

2.1 Cryogel production

The cryogel production was carried out by using Hap and β-TCP in solid phases, in combination with CNF as a polymeric matrix. These materials were integrated according to a protocol that involved the preparation of the solid phases and the subsequent addiction of CNF to form the final structure of the cryogel, ensuring the homogeneity and stability of the compound.

2.1.1 Synthesis of Hydroxyapatite Nanowires

The Hap NW were synthesised using the solvothermal method described and adapted from Zhi-Chao Xiong *et al.* [80]. Firstly, the organic solvent was prepared by mixing, under magnetic stirring at 210 rpm, 11.25 mL of deionised water, 8.75 mL of oleic acid and 5 mL of methanol. Secondly, three separate solutions were prepared: 0.875 g of sodium hydroxide, 0.2775 g of calcium chloride and 0.78 g of sodium dihydrogen phosphate in 12.5 mL, 10 mL, and 15 mL of deionised water, respectively. The first solution was poured into the previously prepared mixture and stirred for 30 min, while the latter two were poured and stirred for only 10 min each, in the order described. Finally, the final volume of the reaction system was transferred to a 125 mL autoclave, sealed and solvothermally treated for 18 h at 180 ºC in a dry oven. After this step and after cooling to room temperature for 2-3 h, the resulting paste was subjected to successive centrifugations of 10-15 min, between 3000 and 6000 rpm, at 5 to 10 ºC (minimizing undesired reactions, keeping the particles more stable and less prone to agglomeration, thereby improving the separation efficiency - cleaner) using the refrigerated centrifuge, being washed with different diluted proportions of ethanol and deionised water to separate the Hap NW from impurities. Then, they were vacuum-dried at 30 ºC and 76 mmHg for 12 to 18 h. The yield was calculated according to the limiting reagent, $CaCl_2$.

2.1.2 Synthesis of β-TCP nanoparticles

The β-TCP nanoparticles were synthesised using the sol-gel method described and adapted by Sanosh K.P. *et al* [67]. Initially, two solutions were prepared: 0.67 M calcium nitrate tetrahydrate and 1 M potassium dihydrogen phosphate both dissolved in deionised water. The calcium nitrate tetrahydrate solution was then added dropwise to the potassium dihydrogen phosphate solution while stirring at 200 rpm. After this step, ammonia was added drop by drop to the above mixture until precipitation was complete and a final pH of 10 was obtained, thus forming a white precipitate. This solution was stirred vigorously for 1 h and then left to rest at room temperature (25 ºC) for 48 h. After resting, the resulting solution was filtered and washed with deionised water to remove soluble by products, such as potassium hydroxide and ammonia. Subsequently, the resulting precipitate was then dried at 40 ºC for 24 h in a dry oven. The dried powder was then calcined at 800 ºC for 30 min using an electric furnace, with a heating rate of 10 ºC/min. Finally, the formed structure was ground using a mortar and pestle. The yield was calculated according to the limiting reagent, $Ca(NO_3)_2 \cdot 4H_2O$.

2.1.3 Cellulose nanofibers and commercial hydroxyapatite

The CNF used in the development of the cryogel was generated from wood-derived fibrils with length in the micrometer (2-3 µm) and width in the nanometric range (10-20 nm) during the biosynthesis of cellulose (Lot #PN01NC0201, crystallinity: 92%). For commercial Hap, Lot #SZBAO480V (micropowder; density: 1g/cm^3; melting point: 1760 ºC) was used for comparations.

2.1.4 Cryogels Formulation

To synthesize the cryogels, the proportions mentioned by Z-C. Xiong *et al.* [81] were optimized, using 15.3 mg of Hap NW in 1 mL of deionised water to achieve a more effective dispersion and modify the final properties of the cryogels, such as porosity and mechanical strength. Besides that, the 15.3 mg total weight of the samples was distributed among Hap NW and the other components: commercial Hap, β-TCP nanoparticles and CNF, depending on the specific cryogel. In a preliminary evaluation phase, several cryogels with different concentrations of Hap, β-TCP, and CNF were tested, as described in Table 2.1:

Table 2.1 - Different cryogels and respective Hap, β-TCP and CNF concentrations (mg/mL) tested. Green colour indicates selected cryogels tested with other characterization methods besides ATR-FTIR and SEM. Yellow colour indicates the control samples (H100 - 100% Hap and C100 - 100% CNF). H-Hydroxyapatite, B-β-TCP and C-CNF

Samples	Concentrations (mg/mL) (Hap: β-TCP: CNF)
H60B40	9.18 : 6.12 : 0
H80B20	12.24 : 3.06 : 0
H90B10	13.77 : 1.53 : 0
H95B5	14.53 : 0.77 : 0
H50C50	7.65 : 0 : 7.65
H67C33	10.25: 0 : 5.05
H85C15	13.00 : 0 : 2.30
H60B7C33	9.18 : 1.07 : 5.05

H75B10C15	11.47 : 1.53 : 2.30
H80B5C15	12.24 : 0.76 : 2.30
H80B13C7	12.24 : 1.99 : 1.07
H100	15.30 : 0 : 0
C100	0 : 0 : 15.30

For each sample, 5-10 replicates were prepared. The preparation was carried out in a 2 mL Eppendorf tube, dispersing the cryogel components, in the previously mentioned proportions, in 0.5-1 mL of deionised water. The dispersion was performed using an ultrasonic processor with a cycle of 1 and 90% amplitude. The paste was placed in polydimethylsiloxane (PDMS) moulds containing perforated wells (8 mm in diameter and 3.5 mm deep), with a glass plate as the base to enhance friction between the two materials. This setup facilitated the targeted freezing of the replicates, as shown in Figure 2.1.a).

The freezing was initially carried out by using liquid nitrogen in a closed styrofoam container, during 5 to 10 min, as illustrated in Figure 2.2.b). The samples were then frozen at -80 ºC for 12 h, followed by lyophilization at -50 ºC and 0.04 Pa for 24 h.

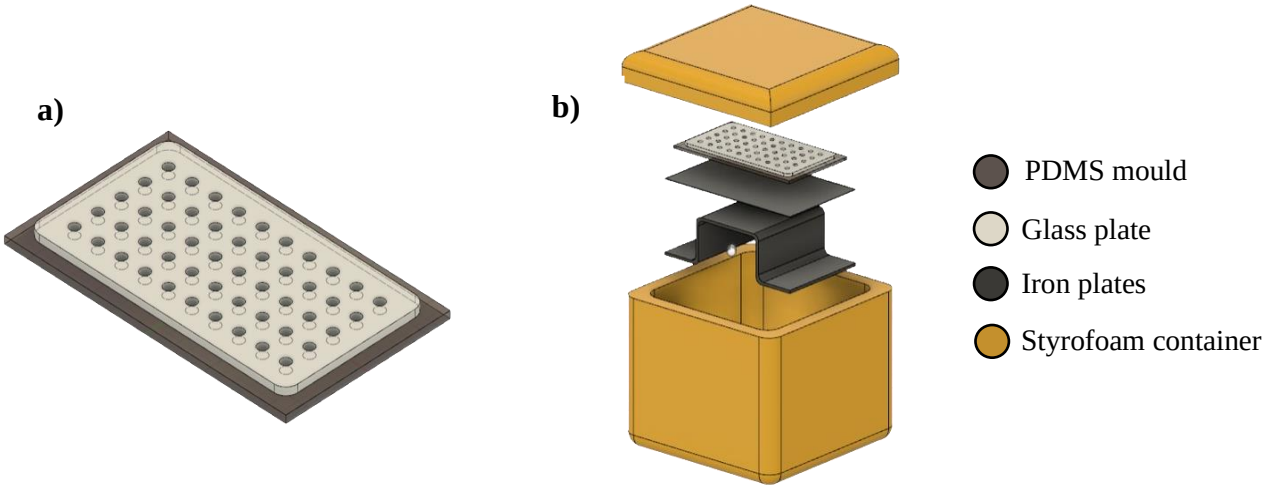

Figure 2.1 – a) Structure used for cryogels formation; b) Setup for targeted freezing.

2.2 Sample Characterization

2.2.1 Structural, Chemical, and Compositional Characterization

X-ray Diffraction (XRD) analysis of the crystallographic structure of Hap NW, commercial Hap, and β-TCP was performed using a diffractometer equipped with the PiXcel detector and CuKα monochromatic radiation source with wavelength of λ= 1.540598 Å. It was generated at 40 kV and 15 mA, over a range of 10º<2θ<90°, with a scanning step size of 0.0217º and time per step of 37.995 s.

The data provided by the spectrum was subjected to a Savitzky-Golay filter followed by subtraction from the baseline obtained initially, in order to smooth out the noise while maintaining the essential characteristics, the peaks and edges, and to obtain a better visualisation and more precise quantification of the existing peaks, such as height and width, respectively. A window of 10, 20 and 50 points

was used for β-TCP, commercial Hap and Hap NW with polynomial order 4 and an 'asymmetric least squares smoothing' baseline mode with a threshold of 0.01 and a smoothing factor of 5 to define the baseline.

The resulting diffraction peaks were compared with the International Centre for Diffraction Data (ICDD) sheets for hexagonal $Ca_{10}(PO_4)_6(OH)_2$ #09-0432, monoclinic $Ca_3(PO_4)_2$ (α-TCP) #009-0348, and rhombohedral $Ca_3(PO_4)_2$ (β-TCP) #009-0169. The presence of impurities in each of the synthesised samples was also verified against the files for hexagonal $CaCl_2$ #026-1053, orthorhombic $NaH_2PO_4 \cdot 2H_2O$ #010-0198, orthorhombic NaOH #035-1009, monoclinic $Ca(NO_3)_2 \cdot 4H_2O$ #026-1406, tetragonal KH_2PO_4 #035-0807, and tetragonal NH_3 #009-0169.

In addition, ATR-FTIR analysis was carried out using a spectrometer, acquiring the spectra between wavenumbers ranging from 400 to 4000 cm^{-1}, to identify the functional groups in Hap, β-TCP, CNF, and compare the various samples produced above.

The Ca/P ratio of Hap and β-TCP produced, the cryogels and Simulated body fluid (SBF) liquids collected after 1, 3, 7, and 14 days of immersion were analysed using an Optical emission spectrometer by ICP-OES. This technique aimed not only to accurately evaluate the stoichiometry of Hap and β-TCP but also to monitor potential changes in ion composition due to the bioactive assays of the cryogels over the time.

2.2.2 Morphological characterization

Morphological observation using Scanning Electron Microscopy (SEM) coupled with Energy-dispersive X-ray Spectroscopy (EDS), was performed to verify the effectiveness of components production, to assess the microstructure of each cryogel, ensure the presence of Hap NW and commercial Hap, and to verify the correct incorporation and dispersion of the nanometric components, such as β-TCP nanoparticles and CNF. All samples were mounted on carbon tape, which was then placed on aluminium plates. Prior to observation, these were coated with gold or titanium by sputter coating in a vacuum chamber, as these materials are non-conductive. The width of 100 replicates of the Hap NW, CNF and the grain size of β-TCP was measured using ImageJ software [82].

2.2.3 Cytotoxicity tests

Colorimetric cytotoxicity assays were carried out not only on the Hap NW, β-TCP, and CNF, but also on the cryogels H50C50, H75B10C15, H80B5C15, H85C15 using resazurin as an indicator, in accordance with ISO-10993-5 norm [83].

First, all samples were sterilised separately in flasks at 120 ºC for 2 h. Extracts were prepared with 1 mL of culture medium (McCoy) in contact with 20 mg for components and 5 mg for cryogels (due to their low mass and large superficial area) selected to a minimum of 24 h at 37 ºC in a CO_2 incubator.

The commercial SaOS-2 cell-line (human osteosarcoma, ATCC HTB-85) were grown in culture flasks, then washed with commercial Phosphate Buffered Saline (PBS) harvested using trypsin and re-suspended in culture medium. Cells stained with trypan blue were counted using a haemocytometer, determining the addition of 9000 cells per well in a 96-well plate. The plate was incubated at 37 ºC with 5% CO_2 for 24 h to allow the cells to adhere to the bottom of the wells. After the incubation period, the

culture medium of extracts in contact with the samples was replaced, the extracts were filtered with a 0.22 µm pore filter and 13 mm diameter, except the extracts containing CNF, and dilutions factors of 1, $^1/_2$, $^1/_4$, $^1/_8$, and $^1/_{16}$ were prepared.

As a positive control (cytotoxic), cells in normal culture medium with 10% dimethyl sulfoxide were added, while as a negative control (non-cytotoxic), cells in complete normal medium were added. For each condition, four replicates were used, as shown in **Figure A.2.1.1**, in section A.2.1, except for the medium control, which has 8 replicates for Hap and β-TCP and 4 replicates for cryogels and CNF. The plate was incubated again at 37 ºC with 5% carbon dioxide (CO_2) for 48 h.

For the viability test, the media were aspirated, and resazurin medium was added: 50% complete culture medium and 50% of a 0.04 mg/mL resazurin solution in PBS. Additionally, a final column corresponding to the medium control was included, using 4 or 8 replicates, where only the resazurin medium was added as mentioned above, to verify if it generates any absorbance signal on its own, without the influence of the cells. The plate was incubated again for a defined period (usually 1 to 4 h) to allow the reduction of resazurin (non-fluorescent blue) to resorufin (fluorescent pink), by metabolically active cells. After this, the absorbance of each well was read and quantified using a microplate reader at 571 and 601 nm, corresponding to the maximum absorbance of resazurin and resorufin, respectively.

Cell viability was assessed by measuring the absorbance in each well and comparing it with the negative control medium. The variation in absorbance is proportional to the number of metabolically active cells. The data treatment it is explain in section A.2.2.

2.2.4 Bioactivity assays

An adapted protocol based on existing methods, ISO/FDIS 23317 [84], as well as Kokubo T. and Takadama H. (2006) [85], were used for the preparation of 1 L of SBF. The reagents listed in the **Table A.3.1**, section A.3were added in the specified order to 750 mL of ultrapure type II water, with magnetic stirring at 37 ºC. The hydrochloric acid (HCl), mentioned in the **Table A.3.1**, was previous prepared using HCl with ≥ 37% of purity.

While keeping the electrode immersed, 1 M HCl was added dropwise until the solution reached a pH value of 7.4 (between 0 and 5 mL). The solution was transferred to a volumetric flask, ultrapure type II water was added to bring the total volume to 1 L and the solution was stored in the refrigerator for up to 1 month and was heated to 37 °C before use.

To determine the minimum volume of SBF, V_S , for the surface area of the cryogel, the calculation was performed using the following equation 2.1:

$$V_S = \frac{S_a}{10} \qquad \textbf{(2.1)}$$

where S_a is the apparent surface area of the cryogel.

For this assay, the samples H50C50, H75B10C15, H80B5C15, H85C15, and H100 were considered. Each sample was placed according to the Figure 2.4 shown below. Since these are cryogels with densities lower than the SBF density, a 100 µm Nylon Cell Strainer (REF 352360, Falcon®) was placed

in each 50 mL Falcon tube, with the top cut off, to ensure that the cryogel remained immersed in the SBF. Each sample was submerged for 1, 3, 7, and 14 days, being maintained at a temperature of 37 ºC inside the incubator without orbital shaking. At the end of each period, the SBF was separated from the sample, which was then washed twice with ultrapure type II water (to remove soluble residues) and left to dry at room temperature. The cryogels were analysed by SEM and EDS mapping and compared with dry cryogel (not immersed) morphologic results. Also, 2 mL of each liquid sample, along with a blank sample containing only SBF, were analysed using ICP-OES.

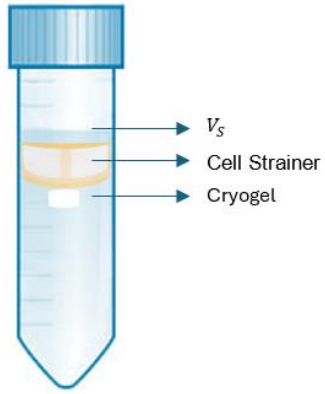

Figure 2.2 - Scheme of a sample in SBF.

The bioactivity of the cryogels mentioned earlier was also analysed using the cryogel surface morphology with SEM and EDS mapping and the percentual evaluation of Ca^{2+} and P^{3-} of SBF through the days mentioned before.

2.2.5 Mechanical Tests

To test and evaluate the mechanical properties of the composites, unconfined uniaxial compression tests were performed on 5 replicates of each cryogel using a universal testing machine. The diameter and height of each sample were precisely measured using a digital calliper. Each sample was subjected to a maximum compression of 6.5 mm and compressed at a rate of 0.2 mm/min until a maximum load cell of 19 N was reached. Five replicates were performed for each condition, and the force and deformation data were collected and converted into stress and strain values, respectively. The Young's modulus, E, was determined by extracting the slope value from the initial linear region of the stress/strain graph obtained and calculated by the follow equation 2.2:

$$E = \frac{\gamma}{\varepsilon} \qquad \textbf{(2.2)}$$

where the γ is stress and ε is strain.

2.2.6 Differential Scanning Calorimetry and Thermogravimetric tests

The heat flow variations and mass changes were measured using DSC and TG, respectively, by heating the samples from room temperature until 550 ºC at a rate of 5 ºC/min with simultaneous thermal analyzer, using 4-5 mg of each cryogel.

2.2.7 Brunauer-Emmett-Teller method

The BET method was carried out, to determine the specific surface area by nitrogen adsorption at 77 K using a gas porosimeter. The samples were degassed beforehand at 100 ºC for >12 h in vacuum. To further assess the porosimetry of the cryogels, an analysis was carried out by using a binocular stereo microscope, equipped with a high-resolution imaging system.

3

RESULTS AND DISCUSSION

This section refers to the characterization of Hap NW, commercial Hap, β-TCP nanoparticles, CNF, and finally, the cryogels of Hap, with and without the elements already mentioned previously.

3.1 Hydroxyapatite nanowires and commercial hydroxyapatite

3.1.1 Hap NW synthesis

Hap NW were successfully produced via solvothermal method [80], which triggered the following reactions between the reagents, using calcium chloride ($CaCl_2$) as the calcium source and precursor, and sodium dihydrogen phosphate ($NaH_2(PO_4) \bullet 2(H_2O)$) as salt and phosphorus precursor:

$$C_{18}H_{34}O_2 + NaOH \rightarrow C_{18}H_{33}O_2Na + H_2O \quad \textbf{(3.1)}$$

$$2C_{18}H_{33}O_2Na + CaCl_2 \rightarrow (C_{18}H_{33}O_2)_2Ca + 2NaCl \quad \textbf{(3.2)}$$

$$NaH_2(PO_4) \cdot 2(H_2O) + 2OH^- \rightarrow PO_4^{3-} + 4H_2O + Na^+ \quad \textbf{(3.3)}$$

$$10(C_{18}H_{33}O_2)_2Ca + 6PO_4^{3-} + 2OH^- \rightarrow Ca_{10}(PO_4)_6(OH)_2 + 20C_{18}H_{33}O_2 \quad \textbf{(3.4)}$$

The formation of calcium oleate is described by equations (3.1) and (3.2). In equation (3.3), an alkaline hydrolysis reaction occurs by reacting $NaH_2(PO_4) \bullet 2(H_2O)$ with hydroxyl ions, derived from the previously added NaOH, resulting in the formation of phosphate anion (PO_4^{3-}), sodium cation (Na^+) and water. Finally, in equation (3.4), hydroxyapatite nuclei are formed, which grow into longer unidirectional crystalline structures, in presence of surfactants such as oleic acid, under high temperatures and pressure over a long period of time [86]. The yield was calculated based on the limiting reagent, with an average value of (59.1 ± 11.2) % obtained from seven performed synthesis. This value is relatively low due to successive washing steps with ethanol and deionized water to remove oleic acid in the final process. The compositional results of 5 samples obtained with ICP-OES (and represented in **Table B.2.1**, section B.2) reveal that the average Ca/P ratio of these Hap NW is (1.96 ± 0.01), which is above the expected ratio of 1.67, although in section 3.1.2, XRD showed that Hap NW was formed. This could be due to the formation of Ca^{2+} oxides or CO_3^{2-} groups (as seen in **Figure 3.3**. a) and b), section 3.1.4),

during the solvothermal method through secondary reactions, which do not contain phosphorus in their composition, resulting in an excess of calcium in the final material [87].

3.1.2 XRD analysis

The diffractograms shown in Figure 3.1 present the diffraction peaks in a) and c), and when converted into percentage, in b) and d), of Hap NW synthesized and commercial Hap, as well as the corresponding data sheet ICDD: 09-0432 (e). These were studied with the aim of comparing and analyzing their crystalline structure in terms of phase, lattice parameters, purity and structural variations.

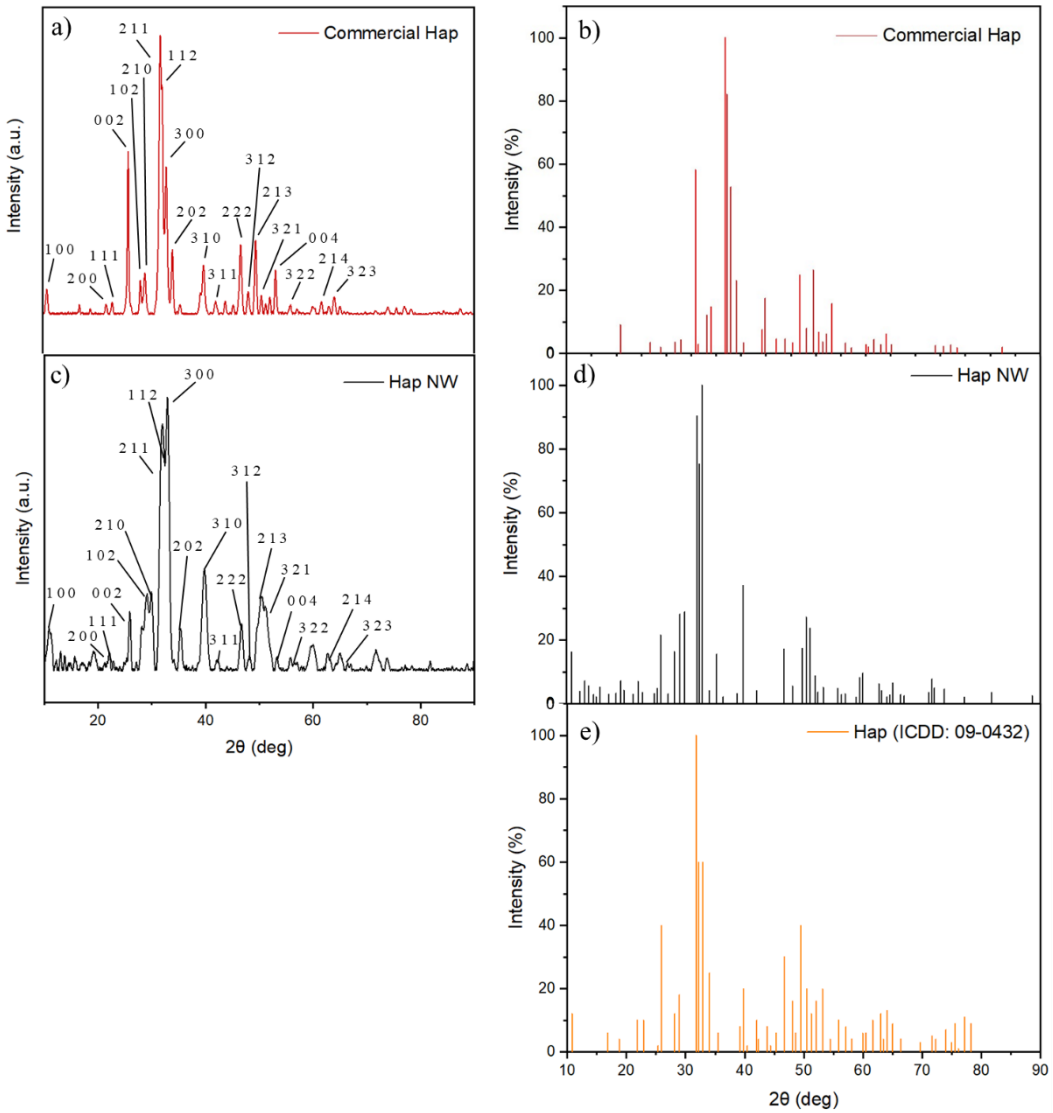

Figure 3.1 - Diffractograms of the diffraction peaks (left) and when converted into percentage (right) of commercial Hap, a) and b), respectively; Hap NW, c) and d), respectively; and data sheet Hap ICDD: 09-0432, e).

By comparing with the ICDD sheet of $Ca_{10}(PO_4)_6(OH)_2$, we can confirm that both commercial Hap and Hap NW exhibit the characteristic peaks of crystalline Hap with a hexagonal phase, as represented respectively in Figure 3.1 a) and c), although there are some differences in their intensities relative to the data sheet. One difference is the higher intensity of (3 0 0) plane, corresponding to 2θ=32.9º,

compared to the (2 1 1) plane in the case of Hap NW. This can be explained by the preferential alignment of crystals along the longitudinal direction of the nanowires (anisotropic morphology) and perpendicular to the referred plane, due to the synthesis process used, which can improve the mechanical strength of the material, crucial for biological applications. Additionally, the presence of sharper and more defined diffraction peaks in the commercial Hap indicates a higher crystalline order compared to Hap NW.

When comparing the diffraction patterns of $CaCl_2$, $NaH_2PO_4 \cdot 2H_2O$, and NaOH, we can identify peaks from $CaCl_2$, notably at 2θ=13.05º (1 0 0), and from $NaH_2PO_4 \cdot 2H_2O$, at 2θ =14.55º (1 1 0), 15.64º (0 1 1), 19.70º (1 1 1), 29.16º (2 1 0), and 29.94º (1 3 1) indicating that the reaction was incomplete, and these substances were not incorporated into the Hap NW lattice, but remained present after washing.

The crystallite size, τ, was calculated for the XRD peak corresponding to the Miller index (2 1 1), using the Debey–Scherrer equation 3.5 represented below:

$$\tau = \frac{\kappa\lambda}{\beta \cos\theta} \qquad \textbf{(3.5)}$$

And, for the calculation, a wavelength of the Cu-Kα radiation of λ =1.540598 Å was used, along with a shape factor of the crystallite, κ, of 0.9, with the angle, 2θ, and the full width at half maximum, β (FWHM), represented in the Table 3.1 for each type of Hap.

Table 3.1 - Crystallite size for Hap NW and commercial Hap according to the Debey–Scherrer equation

Sample	FWHM, β (rad)	Standard error (β)	Peak, 2θ (°)	Standard error (2θ)	Crystallite Size, τ (nm)	Uncer-tainty (nm)
Hap NW	17.6×10^{-3}	2.0×10^{-4}	31.912	0.005	8.17	0.09
Commercial Hap	9.6×10^{-3}	2.4×10^{-4}	31.824	0.008	15.0	0.4

3.1.3 SEM analysis

Considering the images shown in Figure 3.2.a1) and a2), it is possible to observe the successful presence of ultralong nanowire networks resulting from synthesis at a temperature of 180ºC for 18h and in Figure 3.2.a3) and a4), the morphology presented by commercial Hap.

The Hap NW, appear slightly fused in certain areas, with diameters ranging from 200 to 2000 nm (using Figure 3.2.a1 and represented in Figure B.1.1, section B.1, appendix B) and with lengths of several hundred micrometers, thus exhibiting a high aspect ratio. Furthermore, the fact that these nanowires can naturally bend and intertwine may provide significant flexibility and a mechanical advantage for the cryogels compared to the commercial Hap [51], [80]. The Hap NW have a smoother texture compared to the powders, which appear rougher, potentially affecting their reactivity/ interaction with other substances. The powders appear as agglomerates of particles, with a dense and compact distribution forming a plate-like structure in a3) and with an irregular granular morphology, heterogeneous in size (where smaller particles form larger blocks), appear to have a wider size distribution, ranging from tens of nanometers to several micrometers as seen in literature and with significant porosity between the

grains in a4) [88]. Compositional results from ICP-OES of one sample reveal that the Ca/P ratio of these commercial Hap is 1.52 (below the expected ratio).

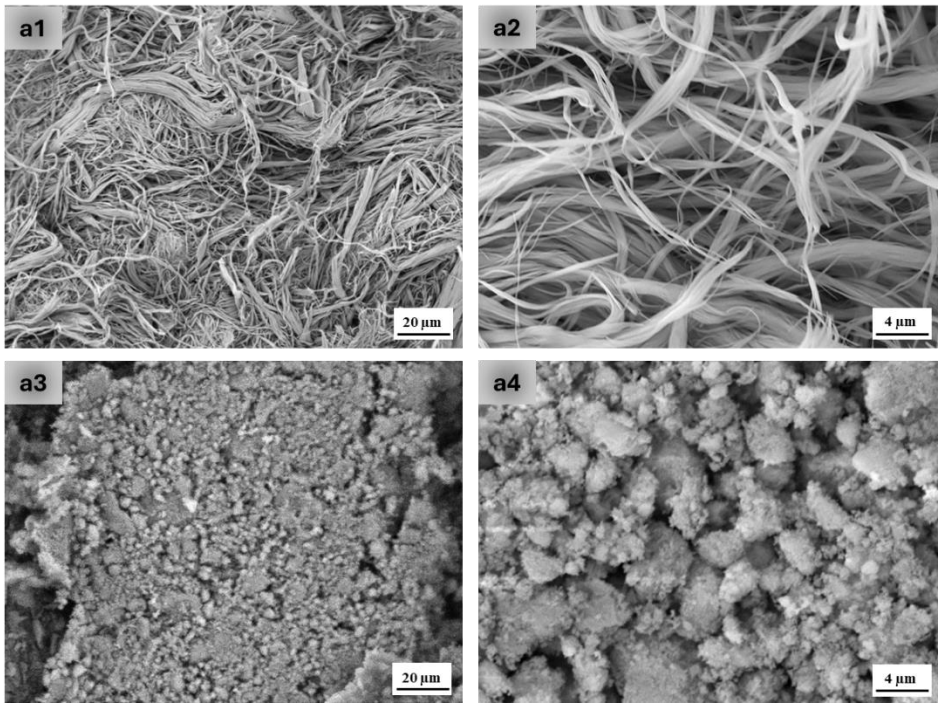

Figure 3.2 - SEM images of Hap NW synthesised at 180 °C for 18h with magnifications of a1) x1K and a2) x5K and commercial Hap with magnifications of a3) x1K and a4) x5K.

3.1.4 ATR-FTIR analysis

The spectra represented in Figure 3.3 reflects the ATR-FTIR analysis of Hap NW synthesized at 180 ºC for 18 h and of commercial Hap (a), showing phosphate (PO_4^{3-}) and hydroxyl (OH^-) bands, typical of a Hap spectrum. In the case of the Hap NW, the bands at 1017 and 1088 cm^{-1} are visible for the asymmetric stretching mode υ_3, and at 961 cm^{-1} for the symmetric stretching mode υ_1 related to the P-O bond. Additionally, the bands at 558 cm^{-1} and 601 cm^{-1} correspond to the O-P-O bending mode (υ_4 stretching mode) found in apatite. The OH^- groups are represented by bands at 628 and 3572 cm^{-1}, attributed to the bending and stretching modes, respectively [89], [90]. The small band at 880 cm^{-1} is attributed to the [P-(OH)] stretching of HPO_4^{2-} ions. It is also possible to observe a broad band between 3700 and 2500 cm^{-1}, along with peaks at 2853 and 2924 cm^{-1}, which could have appeared due to the adsorption of water and oleic acid (C-H groups – methyl and methylene) on the surface of the ultralong Hap NW, respectively [51], [90]. In the case of the commercial Hap, the bands at 561, 601, 963, 1024, and 1090 cm^{-1} are visible and representative of PO_4^{3-} groups. The OH^- groups are represented by the bands at 629 and 3568 cm^{-1}. There are no impurities, except for the small band at 878 cm^{-1}, which is associated with the presence of HPO_4^{2-} ions.

By observing the Figure 3.3.b), the presence of carbonate groups is visible and confirmed by the characteristic bands at 1414 and 1549 cm^{-1}, corresponding to A-type and B-type carbonate substitutions, respectively. In A-type carbonate, CO_3^{2-} ions replace OH^- ions in the Hap NW channels, leading to an expansion along the a-axis and a contraction along the c-axis, while in B-type carbonate, CO_3^{2-} ions replace PO_4^{3-} ions in the Hap NW structure, causing the inverse of A-type. Thus, the synthesised

Hap is a carbonated Hap of A&B type, as indicated by the peak position at 1456 cm^{-1}, resulting in a mixed substitution that constitutes bone mineral [89], [91], which is advantageous as it enhances similarity to natural bone, improves bioactivity, provides controlled solubility, optimizes structural properties, and promotes better cellular compatibility for bone regeneration..

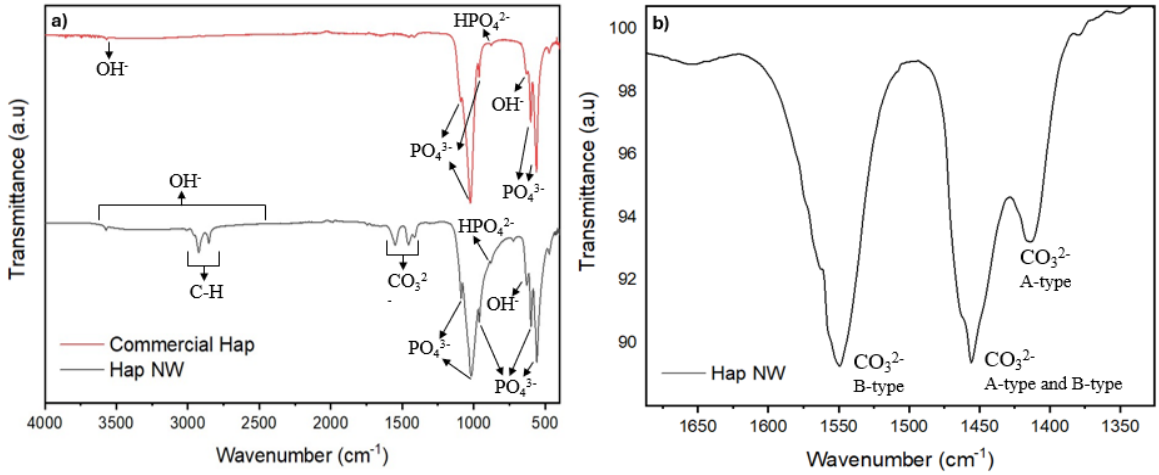

Figure 3.3 - a) ATR-FTIR spectra of Hap NW synthesised at 180 ℃ for 18 h and commercial Hap. b) ATR-FTIR spectrum of the region between 1750 cm^{-1} and 1300 cm^{-1} of Hap NW corresponding to A-type and B-type carbonate substitutions.

3.2 β-TCP nanoparticles

3.2.1 β-TCP synthesis

As previously mentioned, the β-TCP nanoparticles were successfully produced in precipitate form using the sol-gel method [67], according to the following reaction (equation 3.6), with calcium nitrate tetrahydrate ($Ca(NO_3)_2 \bullet 4H_2O$) as the calcium source and potassium dihydrogen phosphate (KH_2PO_4), as the phosphate source:

$$3Ca(NO_3)_2 \bullet 4H_2O + 2KH_2PO_4 + 6NH_4OH \rightarrow Ca_3(PO_4)_2 + 2KOH + 6NH_4NO_3 + 16H_2O \quad \textbf{(3.6)}$$

This synthesis can be explained by nucleation-aggregation-agglomeration-growth mechanism outlined in Figure 3.4. During precipitation, small nuclei form and begin to grow as solute ions, Ca^{2+} and PO_4^{3-}, deposit onto them, forming β-TCP nanocrystals. Aggregation occurs when the formed nanocrystals start to cluster due to molecular attraction between them, arising from different forces at the nanometric/colloidal scale that minimize the free surface energy. Under constant temperature and supersaturation conditions, the nanocrystal aggregates cement together, forming denser and more

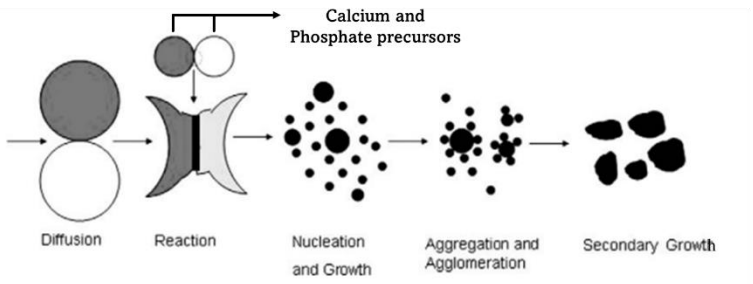

Figure 3.4 - Schematic representation of the nucleation-aggregation-agglomeration-growth mechanism in the production of β-TCP nanoparticles (adapted from Ishikawa K. *et al.* (2020)[92]**.**

organized agglomerates. The residual supersaturation acts as a cementing agent within the aggregates, keeping the particles bonded. Agglomeration and calcination temperature influence the final size of the secondary particles and their physical and chemical properties, according to Sanosh K.P *et al.* [67].

The yield of this reaction was calculated based on the limiting reagent, obtaining a value of (92.18 ± 0.03) %. Regarding the compositional analysis of the nanoparticles, it was performed using ICP-OES, revealing a Ca/P ratio of 1.87 for one sample (and represented in **Table B.2.2**, section B.2), which is above the standard corresponding to 1.5, although in **Figure 3.5**, section 3.3.2, XRD analysis showed that β-TCP was formed. The high temperatures during the calcination of the sol-gel method (800 ºC for 30 min) may favor the loss of phosphorus in the form of volatile compounds, resulting in a final material with less phosphorus in its composition and the formation of calcium oxide (CaO), which increases the Ca/P ratio.

3.2.2 XRD analysis

The diffractograms shown in Figure 3.5 present the actual diffraction peaks (a), and when converted into a percentage (b) of the β-TCP nanoparticles. This was compared with the ICDD files #09-0169 (c) and #09-0348 (d) to evaluate which phases of TCP, α-TCP or β-TCP, respectively, were formed in the sample. This procedure is essential to determine the predominant phase, check for any phase transitions that may occur during the synthesis process, and assess purity and structural changes.

The comparison of the resulting diffractogram with the ICDD cards for $Ca_3(PO_4)_2$ shows that the produced nanoparticles exhibit predominantly characteristic peaks of β-TCP with a rhombohedral structure, but not the peaks characteristic of α-TCP, with monoclinic structure.

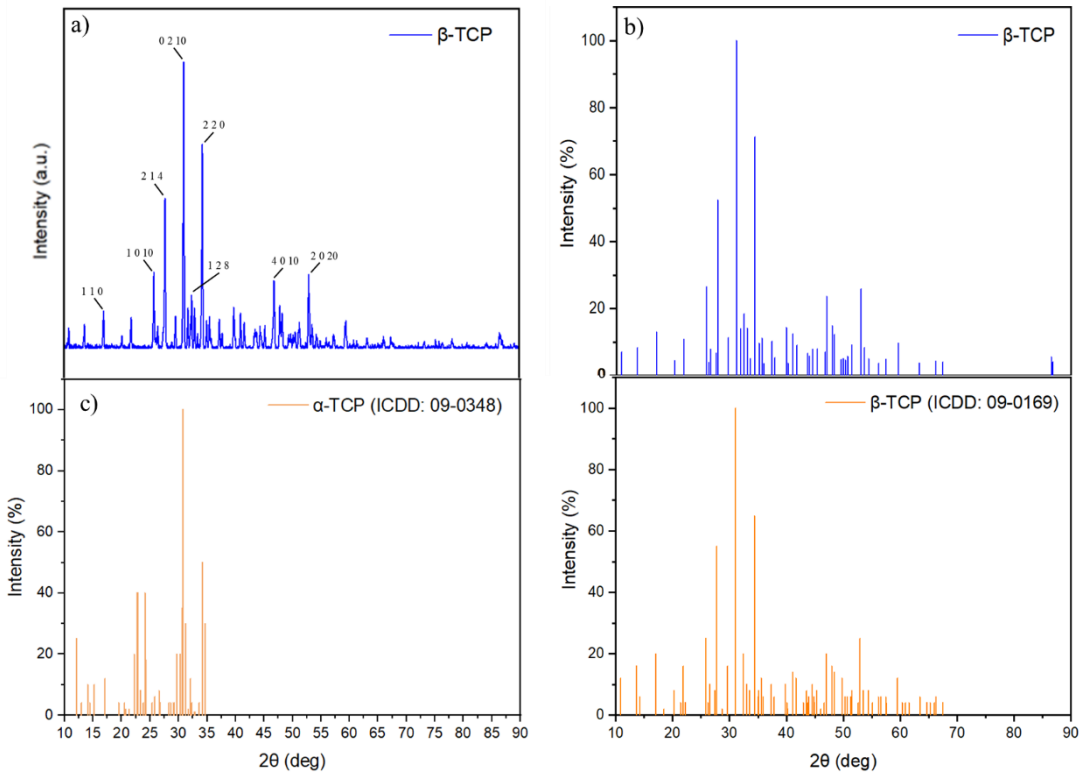

Figure 3.5 - Diffractograms of the diffraction peaks and when converted into percentage of β-TCP, a) and b), respectively; and data sheets α -TCP ICDD: 09-0348 and β-TCP ICDD: 09-0169, c) and d) respectively.

Upon comparing the data with the KH_2PO_4 and $Ca(NO_3)_2{\bullet}4H_2O$ reference files, small peaks were identified at 86.79º (5 1 4), 31.83º (2 3 0), and 49.54º (3 2 3), corresponding to the phosphate and calcium precursors, indicating that the reaction was incomplete, in spite of the high yield calculated in section 3.2.1. The comparison with the NH_3 reference file did not reveal any characteristic peaks of this reagent, indicating that good filtering and washing were carried out during the β-TCP synthesis.

The crystallite size was calculated for the XRD peak corresponding to the Miller index (0 2 10), using the Debey–Scherrer equation 3.5, presented in section 3.1.2. A wavelength of λ ($CuK\alpha$) = 1.540598 Å was used, with the shape factor κ set to 0.9. The values of 2θ and β (FWHM) are shown in Table 3.2 for the β-TCP nanoparticles:

Table 3.2 - Crystallite size for β-TCP according to the Debey–Scherrer equation

Sample	FWHM, β (rad)	Standard error (β)	Peak, 2θ (°)	Standard error (2θ)	Crystallite Size, τ (nm)	Uncertainty (nm)
β-TCP	3.3×10^{-3}	7.3×10^{-5}	31.060	0.002	43.6	1.0

The crystallite size obtained (43.6 ± 1.0) nm is below that reported in the literature (83 ± 6) nm, which is due to the alteration of the molarity of the reagents, directly influencing the nucleation and growth of the crystals. This fact is justified by Windarti T. *et al*. (2019), who state that the size of β-TCP crystallites increases with the Ca/P ratio (M) used by the precursors. This ratio is lower (0.67) than the theoretically established one (1.5), resulting in different levels of stability and aggregation before calcination, contributing to the formation of smaller or less cohesive structures. Besides that, the size is consistent with the size of calcium phosphate in human bones, which ranges between 40-60 nm [66].

3.2.3 SEM analysis

The results of SEM analysis of β-TCP synthesis are presented in Figure 3.6. It clearly demonstrates that the β-TCP nanoparticles consist of small, irregularly shaped particles covered by an amorphous accumulation of clouds revealing a rough texture in the surface [93]. They appear as spherical granules, notably in a prolate spheroidal phase structure. This morphology can be attributed to the increase in lattice parameters along the a-axis and the reduction along the c-axis [94]. The particle sizes ranged from 200 to 650 nm (using Figure 3.6.b2 and represented in **Figure B.1.2**, section B.1), showing a broader particle size distribution compared to the literature, which indicates a predominance of particles with diameters between 70 and 80 nm, reaching up to 350 nm. This may be related to the grinding process carried out with the mortar, indicating a need for optimization, or to the agglomeration of some β-TCP particles present along the images [67].

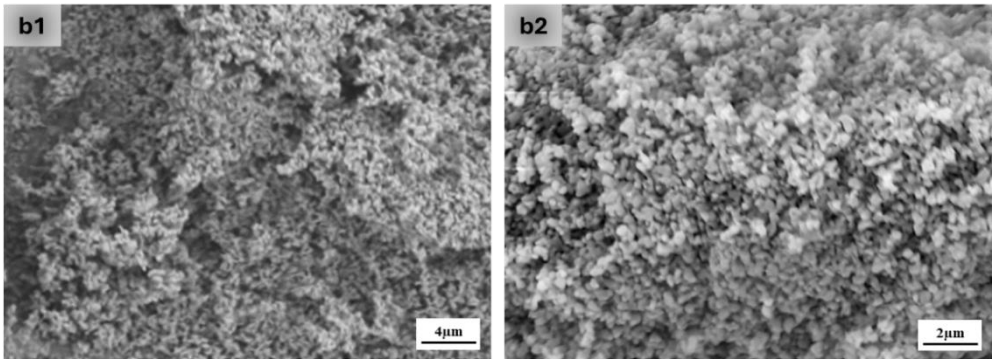

Figure 3.6 - SEM analysis of β-TCP with magnifications of b1) x5K and b2) x10K

3.2.4 ATR-FTIR analysis

The spectrum represented in Figure 3.7 reflects the ATR-FTIR analysis of β-TCP calcined at 800 ºC, showing phosphate group vibrations, characteristic of a β-TCP spectrum. Visible bands at 1022 and around 1098 cm^{-1} correspond to the triply degenerate asymmetric P-O stretching mode (υ_3), with the first being more pronounced. Additionally, the bands around 945 and 972 cm^{-1} are attributed to the non-degenerate symmetric P-O stretching (υ_1), and the bands at 602, 571, and 544 cm^{-1} correspond to the triply degenerate O-P-O bending mode (υ_4), with the first and last being more pronounced [67][95]. A small stretching and liberational band at 629 cm^{-1}, minimally significant, can also be observed, indicating OH^- groups present in the structure. Additionally, a small band at 3574 cm^{-1} was detected, corresponding to water adsorbed by the synthesised material. Moreover, the absence of any strong peak at 1400-1600 cm^{-1} and around 875 cm^{-1} suggests that neither CO_3^{2-} groups constituents of bone structures, nor the HPO_4^{2-} groups, respectively, are present in the sample [67], [96].

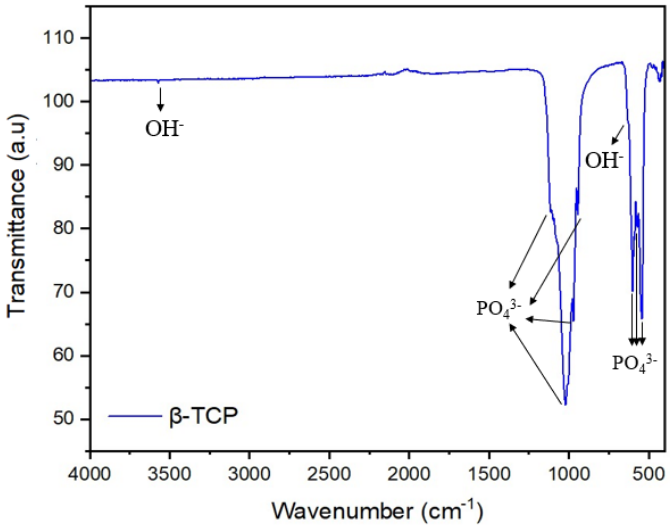

Figure 3.7 – ATR-FTIR spectrum of β-TCP calcined at 800ºC.

3.3 Cellulose nanofibers

3.3.1 SEM analysis

The SEM analysis of the cellulose used in the composition of some previously mentioned cryogels is shown in Figure 3.8, showing an elongated shape with thin uniform flexible fibers, forming a dense complex and separated from adjacent fibers [97]. The orientation of the fibers is random, which is characteristic of this type of material [98]. The surface of the observed fibers is smooth, with no significant roughness or cracks. In some areas of the images, minimal presence of fibers agglomerates and irregularities can be noted, likely due to the drying or dispersion process. This morphology of the CNF suggests that it is suitable for applications in the production of nanocomposites. The ImageJ software showed diameters ranging from 5 to 30 nm (using Figure 3.8.c1 and represented in **Figure B.1.3**, section B.1) which contradict the product specifications. This could be due to the formation of

aggregates and stacking during the dispersion or drying process carried out by the manufacturer, or due to the binding to residues present in the environment (e.g. humidity).

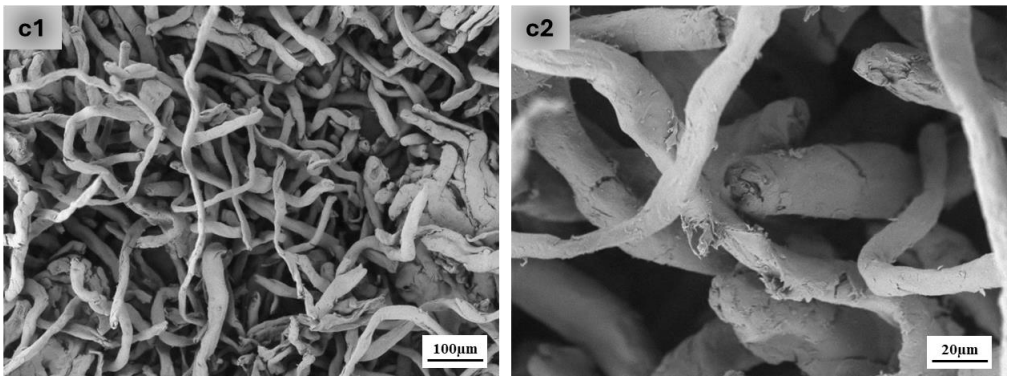

Figure 3.8 - SEM analysis of cellulose with magnifications of c1) x200 and c2) x1K.

3.3.2 ATR-FTIR analysis

The spectrum represented in Figure 3.9 corresponds to the ATR-FTIR analysis of CNF. A band can be observed between 3700 and 3000 cm^{-1}, more specifically at 3335 cm^{-1}, corresponding to OH^- groups, namely intra- and intermolecular hydrogen bonds, as well as water adsorbed by the cellulose. The asymmetric and symmetric stretching vibrations of C-H (methylene groups) are visible around 2900 cm^{-1}, which are related to the carbon chains of glucose, the monomeric unit of cellulose. The absorption band around 1590 cm^{-1} corresponds to stretching of CNF carboxylic groups [99], [100]. The bands located at 1414 and 1322 cm^{-1} represent the symmetric bending mode of CH_2 groups. The most pronounced bands were observed between 1200 and 1000 cm^{-1}, corresponding to C-O-C stretching vibrations (pyranose ring) in the intra- and intermolecular structure of cellulose, with bands at 1025 and 1052 cm^{-1} revealing glycosidic deformation (C_1-O-C_4) between glucose units. Furthermore, the small band observed around 913-915 cm^{-1} corresponds to $\beta_{1\text{-}4}$ glycosidic bonds (C-H glycosidic deformation). The small band at 659-662 cm^{-1} is related to the C–O–H bending mode [101]–[103].

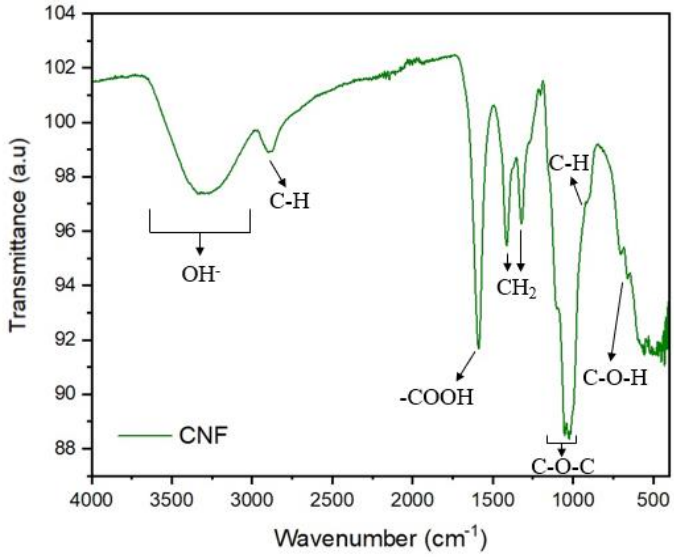

Figure 3.9 - ATR-FTIR spectrum of CNF.

3.4 Cryogels of Hap, β-TCP and CNF

3.4.1 SEM analysis

Through SEM analysis, represented in Figure 3.10 and **Figure B.3.1.1** (in section B.3.1), the microscopic homogeneity of the cryogels listed in **Table 2.1** of section 2.1.4 was examined, focusing on their surface, which is crucial for understanding characteristics such as pore distribution uniformity and external morphology, while maintaining the integrity of the porous structure. The cross-sections of the cryogels were not examined, as the pressure applied by the blade during cutting could alter the material's porosity, resulting in deformation or collapse of the structure.

Regarding the cryogels produced with Hap NW and β-TCP, despicted in Figure 3.10 from image a1) to d3), a good dispersion of the components throughout the matrix was observed, although some agglomerates of β-TCP were found (e.g. image c1)). In addition, it appears to have a heterogeneous distribution of porosity, suitable for cell migration and nutrient supply, respectively [104]. This, coupled with insufficient material concentration in certain regions, may lead to the creation of stress points, possible making the cryogels less resistant to external forces and more prone to rupture, limiting their mechanical stability. Visualizing the images c3) and d3), the structures appear to weaken with the introduction of more than 10% of β-TCP, as it is an inherently brittle material, which may limit its use in load-bearing applications [105].

The images e1) to g3) from Figure 3.10 show composite cryogels of Hap NW and CNF in different concentrations (mg/mL), showing that CNF promotes the formation of a fibrous network intertwined with Hap NW after lyophilization. This is demonstrated by comparing them with images l2) and m2), for example, which could be due to the high surface area of the CNF and the hydroxyl groups (OH^-) on the crystalline surface, forming strong hydrogen bonds between adjacent fibers, with deionized water acting as an intermediary [72]. Lyophilization may contribute to the formation of porous structures due to the removal of the solvent, without structural collapse, what could lead to an increase in rigidity with higher Hap NW content.

As for Figure 3.10 from h1) to k2), they exhibit cryogels with different concentrations of Hap NW, β-TCP, and CNF, resulting in a hybrid structure that combines stiffness, biodegradability, and flexibility. The reduction in CNF concentration leads to regions where the Hap NW are not fully enveloped by the fibrous network, which may result in a less cohesive and less uniform structure in some areas. The dispersion of β-TCP nanoparticles in these aerogels was successful, although there were still some particles that did not separate due to insufficient grinding, resulting in heterogeneous size particles. Figure 3.10 from l1) to m3) served as a comparative standard.

From the samples listed in **Table 2.1** of section 2.1.4, some were selected based on prior cryogel analysis that exhibited a better structure, being quantified and mapped by EDS (**Figure B.3.2.1** to **Figure B.3.2.5** shown in section B.3.2). Taking this selection into account, a new batch was tested in which the Hap NW were replaced by commercial Hap for comparation, named: Hp50C50, Hp75B10C15, Hp80B5C15, Hp85C15 and the reference sample, Hp100, shown in **Figure B.3.1.1** from a1) to e3), section B.3.1. SEM analysis revealed that the Hap particles and those containing β-TCP were successfully incorporated into the fibrous network created in the process of forming the cryogels containing CNF. Despite the good incorporation, the final structure of the cryogels appears to have a matrix with

less cohesion and more fragility, due to the absence of nanowires, which can be seen with the naked eye.

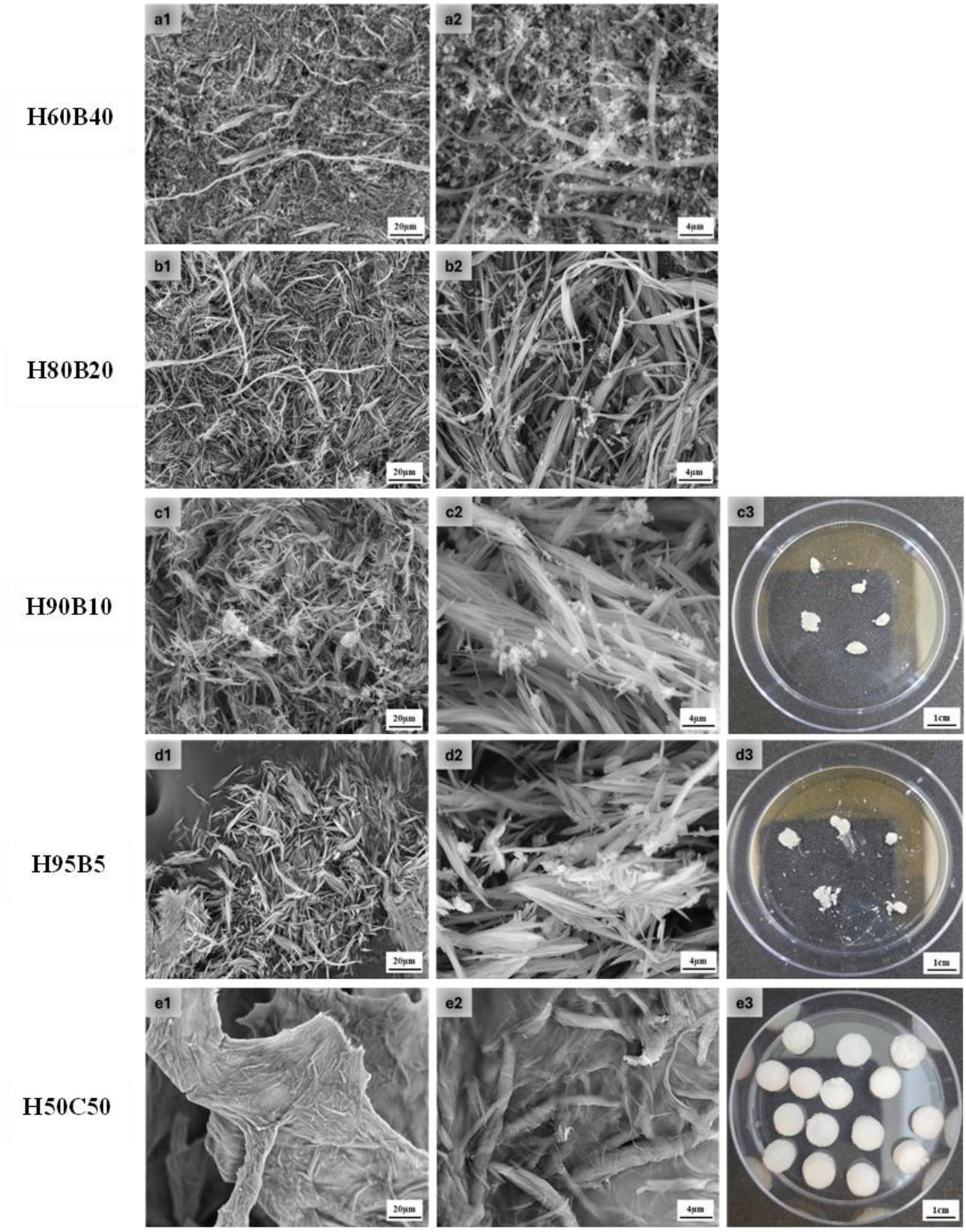

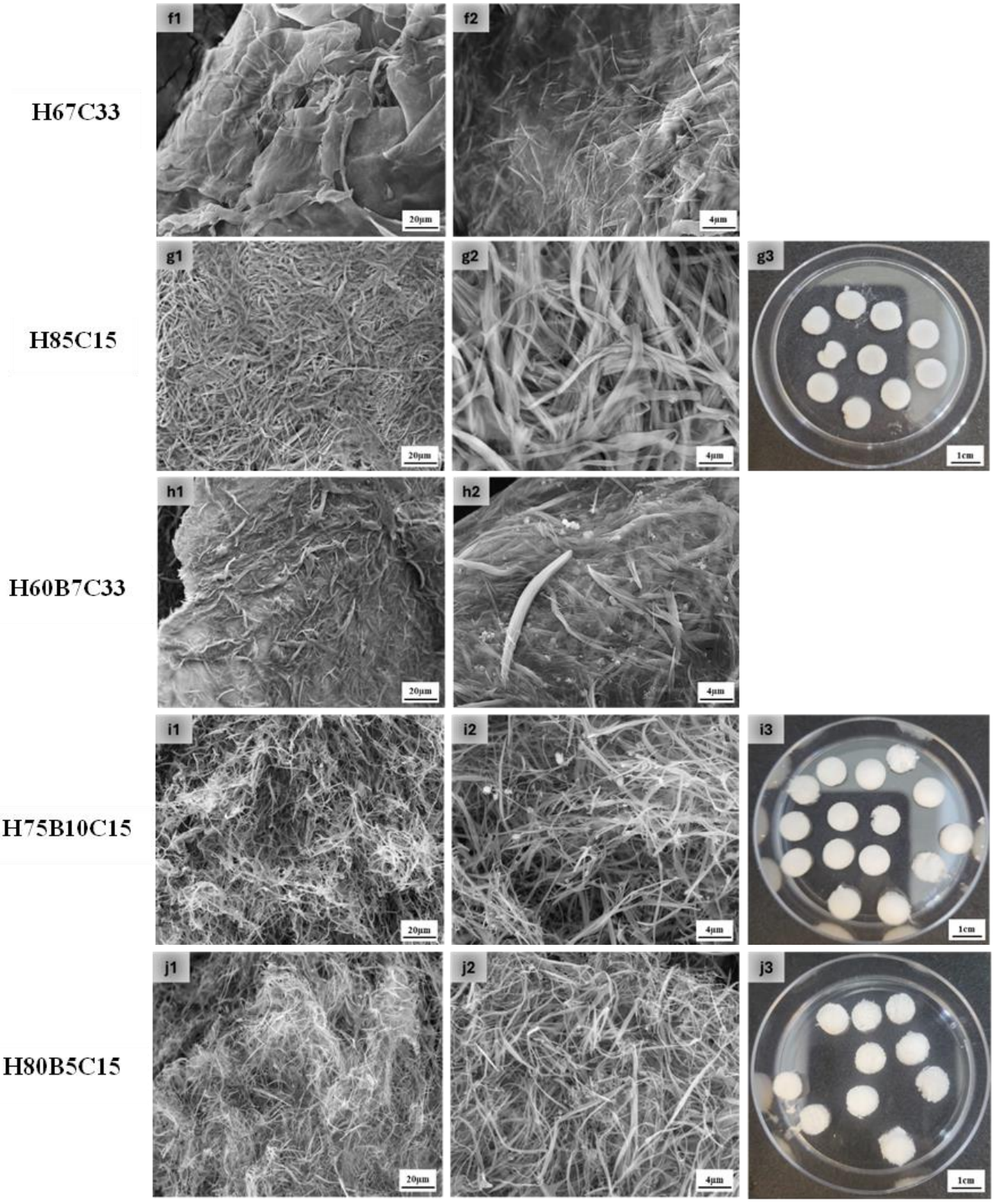
H67C33
f1
20μm
f2
4μm
H85C15
g1
20μm
g2
4μm
g3
1cm
H60B7C33
h1
20μm
h2
4μm
H75B10C15
i1
20μm
i2
4μm
i3
1cm
H80B5C15
j1
20μm
j2
4μm
j3
1cm

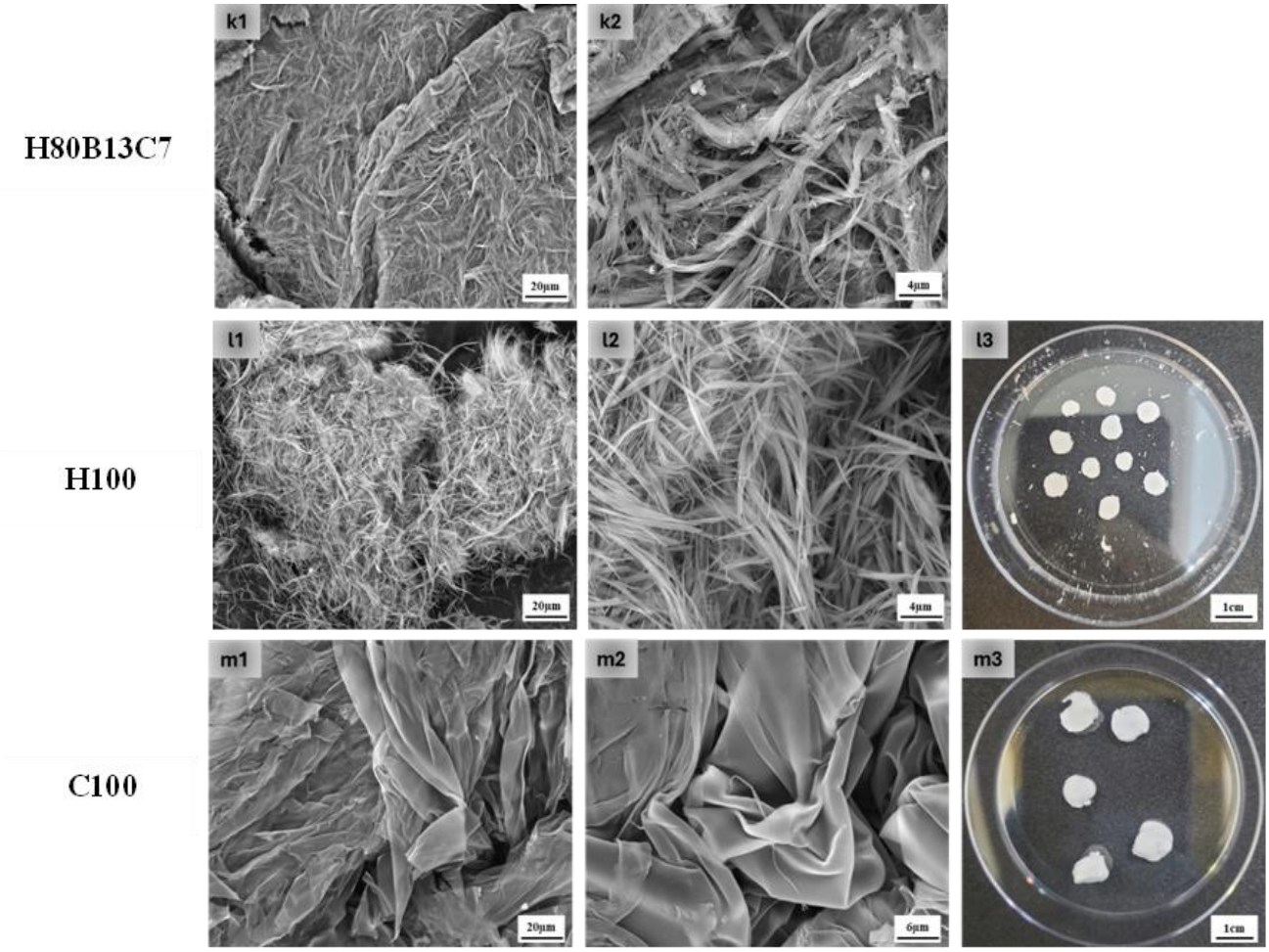

Figure 3.10 - SEM analyses of cryogels with Hap NW. H60B40: a1) x1K and a2) x5K; H80B20: b1) x1K and b2) x5K; H90B10: c1) x1K, c2) x5K and c3) naked eye morphology; H95B5: d1) x1K, d2) x5K and d3) naked eye morphology; H50C50: e1) x1K, e2) x5K and e3) naked eye morphology; H67C33: f1) x1K and f2) x5K; H85C15: g1) x1K, g2) x5K and g3) naked eye morphology; H60B7C33: h1) x1K and h2) x5K; H75B10C15: i1) x1K, i2) x5K and i3) naked eye morphology; H80B5C15: j1) x1K, j2) x5K and j3) naked eye morphology; H80B13C7: k1) x1K and k2) x5K; ; H100: l1) x1K, l2) x5K and l3) naked eye morphology; and C100: m1) x1K, m2) x3K and m3) morphology. H – Hap NW, B - β-TCP and C - CNF.

3.4.2 ATR-FTIR analysis

The results obtained by ATR-FTIR from the various samples mentioned in **Table 2.1** of section 2.1.4 are represented in Figure 3.11, where the characteristic bands of each component in the different cryogels can be observed.

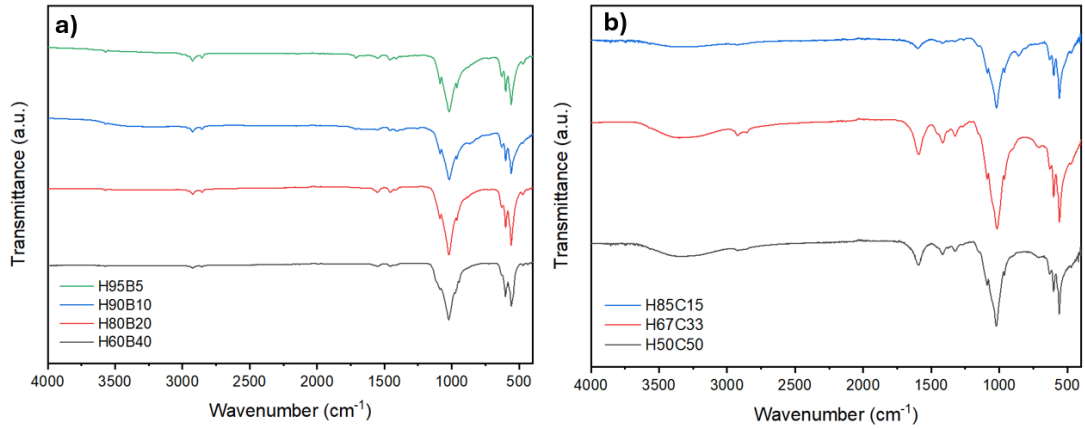

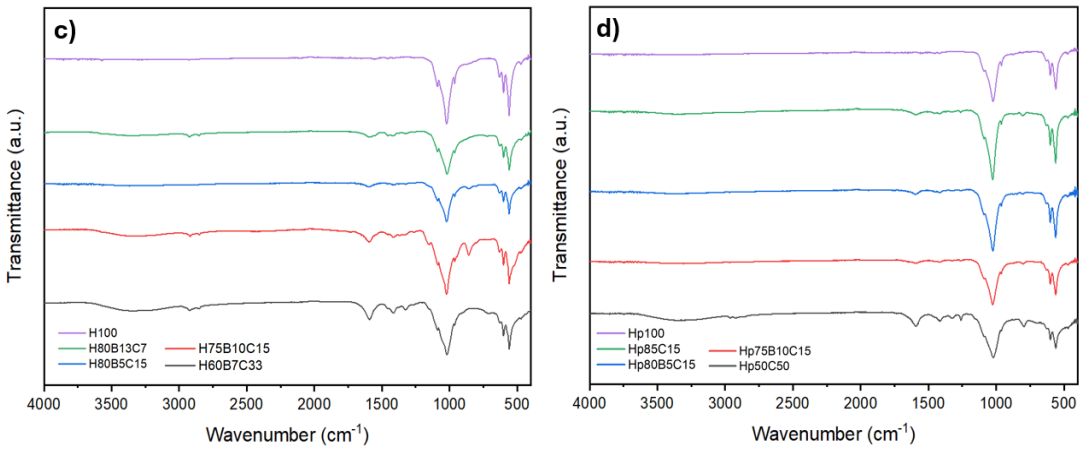

Figure 3.11 - a) ATR-FTIR spectra of cryogels H60B40, H80B20, H90B10, H95B5; b) ATR-FTIR spectra of cryogels H50C50, H67C33; c) ATR-FTIR spectra of cryogels H60B7C33, H75B10C15, H80B5C15, H80B13C7, H100; d) ATR-FTIR spectra of cryogels: Hp50C50, Hp75B10C15, Hp80B5C15, Hp85C15, Hp100 .

Starting with graph a), bands related to PO_4^{3-} can be detected around 1020 and 560 cm^{-1}, as well as the -OH band around 629 cm^{-1}, indicating the coexistence of both components, Hap NW and β-TCP, in the cryogels. The increase of β-TCP shows a decrease in the band around 2900 cm^{-1} and between 1400 and 1500 cm^{-1}, corresponding to the C-H and CO_3^{2-} groups, which is related to impurities found in the synthesized Hap of this sample.

In graph b), it is possible to detect not only the bands related to PO_4^{3-} around 1020 and 560 cm^{-1}, corresponding to Hap in this case, in the cryogels H85C15, H67C33, and H50C50, but also the bands at 1590 cm^{-1} and located at 1414 and 1322 cm^{-1}, related to CNF carboxylic groups and CH_2 groups, respectively, corresponding to CNF. Furthermore, the increase in CNF shows a broadening of the band around 3335 (-OH groups) and 1000 cm^{-1} (C-O-C groups) and the appearance of a band around 2900 cm^{-1} (C-H groups).

The ATR-FTIR graphs c) and d) show the cryogels produced that encompass the three components discussed, differing in the type of Hap, nanowires and commercial, respectively. In these, the same behavior observed in graphs a) and b) is visible, revealing a good integration of the three materials in the cryogels, with interactions between functional groups, but without significant changes in the molecular structure of the components.

3.4.3 Cytotoxicity tests

The *in vitro* colorimetric assays using resazurin as an indicator enabled the evaluation of the cytotoxic potential across various dilutions, including those of Hap NW, β-TCP nanoparticles, CNF nanofibers, as well as the selected cryogels: H50C50, H75B10C15, H80B5C15, and H85C15.

Figure 3.12 and **Table B.4.1**, in section B.4 present the relative cell population and associated relative uncertainty in percentage for each of the particles mentioned and tested across various dilutions.

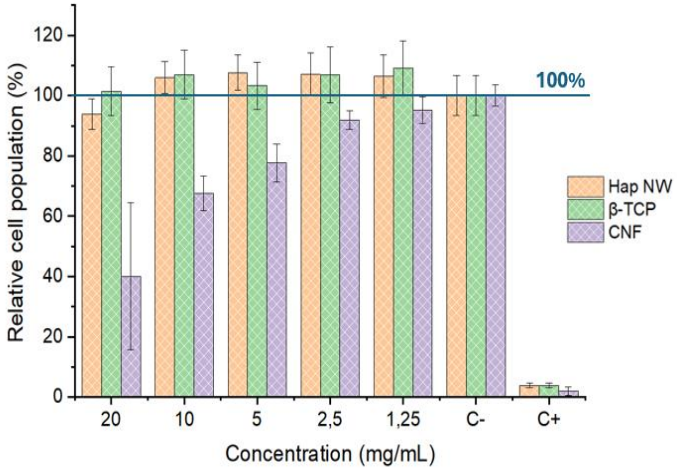

Figure 3.12 - Histogram data from the cytotoxicity tests of Hap NW, β-TCP, CNF and negative (C-) and positive (C+) control groups for

It is possible to observe that all particles demonstrated high cell viability, with a relative population above 100% for each dilution shown, except for cellulose in all dilutions and Hap NW at 20 mg/mL, with the last above 90%. This demonstrates not only efficient cell survival but also good cell proliferation for Hap and β-TCP, showing that they are non-cytotoxic at all concentrations when compared with **Table A.2.2.1**, in section A.2.2.

Regarding CNF, we observe an increase in cell viability as the concentration used in the medium decreases. Several cytotoxicity studies with CNF's conducted at relatively high concentrations by Gao *et al.* (2018) [106] or Kumari *et al.* (2019) [107] indicated no cytotoxicity up to 1 mg/mL In addition, Tibolla *et al.* (2019) [108], while extracting CNF from banana peel through enzymatic hydrolysis and analyzing it, found that up to 2 mg/mL, cell viability was not significantly affected. However, above 5 µg/mL, there was a considerable reduction in comparison to the control group. This can be observed in the graphs obtained, allowing us to conclude that when used in high concentrations, specifically above 5 mg/mL, CNF exhibits cytotoxic characteristics. It is not possible to determine a clear reason for this cytotoxicity given the lack of information, but it may be related to CNF's ability to absorb nutritional components from the culture medium (possible detected and followed by ICP-OES along the process), which could lead to cell death by depletion of essential nutrients for their survival or due to the presence of carboxylic acid in the polymeric fiber chains. It is, therefore, recommended to establish reasonable exposure concentrations and, if necessary, add supplementary components to the culture medium. The presence of changes in CNF aggregation/clustering and dispersion states due to the components of the culture medium also needs to be considered [109].

In the case of the synthesized cryogels, Figure 3.13 and **Table B.4.2**, in section B.4 present the relative cell population and the associated relative uncertainty in percentage for each cryogel mentioned and tested for the same dilution factors.

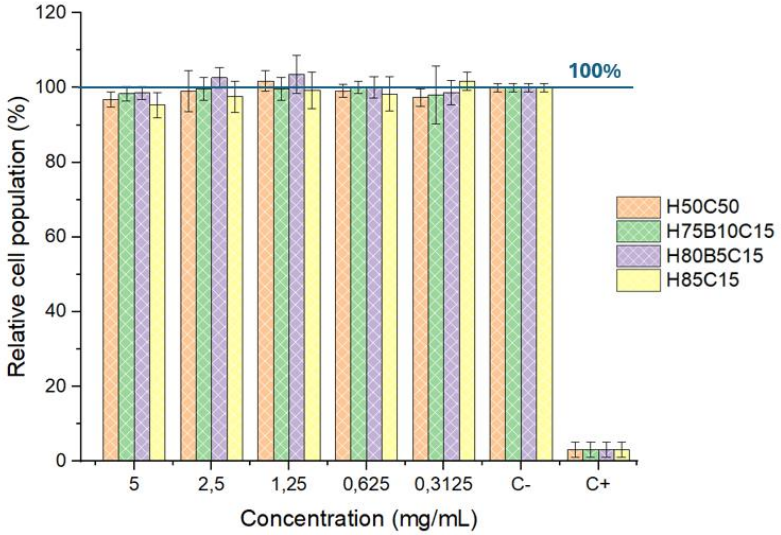

Figure 3.13 - Histogram data from the cytotoxicity tests of cryogels: H50C50, H75B10C15, H80B5C15, H85C15 and negative (C-) and positive (C+) control groups for each one.

Considering the relative uncertainty, all samples show viability above 90%, thus demonstrating that they are non-cytotoxic at all concentrations, when compared to **Table A.2.2.1**, in section A.2.2. The result is predictable since Hap and β-TCP were shown to be non-cytotoxic and due to the low amounts of CNF administered in each sample.

3.4.4 Bioactivity assays in SBF solution

For the bioactivity assay performed on the cryogels H100, H50C50, H85C15, H75B10C15, and H80B5C15, each was immersed in an SBF solution maintained at 37ºC, simulating body temperature, for different periods (1, 3, 7, and 14 days). Along with these, a control group consisting only of SBF was prepared separately. Given the variations in the surface area of the cryogel, ranging from 265.51 to 282.74 mm², the excess value was considered, and V_s was set at 30 mL, with the minimum value being 28.274 mL according to equation 2.1 in section 2.2.4. Although they maintained their shape due to the amphiphilic component of cellulose, the cryogels containing CNF were the only ones that rose to the surface due to their low density, while H100 remained at the bottom of the Falcon tube. This protocol aims to evaluate the possible formation of a Hap layer on the surface of a given biomaterial after immersion in SBF. Due to the similarity of Hap with the mineral phase of bone tissue, it is believed that the ability to develop a superficial Hap film is crucial for the biomaterial's bonding to bone. According to Kokubo *et al.* [85], by immersing the material in SBF, it is possible to study the precipitation of Hap and the subsequent bioactivity of the material when implanted *in vivo* [110].

When that immersion occurs, two phenomena typically happen: the dissolution of the material and the formation of a calcium and phosphate (Ca/P) layer on its surface. If dissolution predominates, the ions concentration in the solution increases. On the other hand, if there is a decrease in the ion concentration (Ca^{2+} and P^{3-}), it means that these ions are removed from the solution and used in the formation of a new Ca/P layer [111].

Considering the concentrations of Ca^{2+} and P^{3-} in the SBF, 6.9 and 30.3 mg/L, respectively, different variations in the release and retention of these ions into the medium was observed for all cryogels at different periods in Figure 3.14. However, these variations are not significant, at least in the first 14 days evaluated, as confirmed by the analysis of SEM images and EDS mapping (all Figures in section B.5.1 and B.5.2, respectively), due to the absence of deposition of these ions on the cryogels, which may indicate the lack of bioactivity.

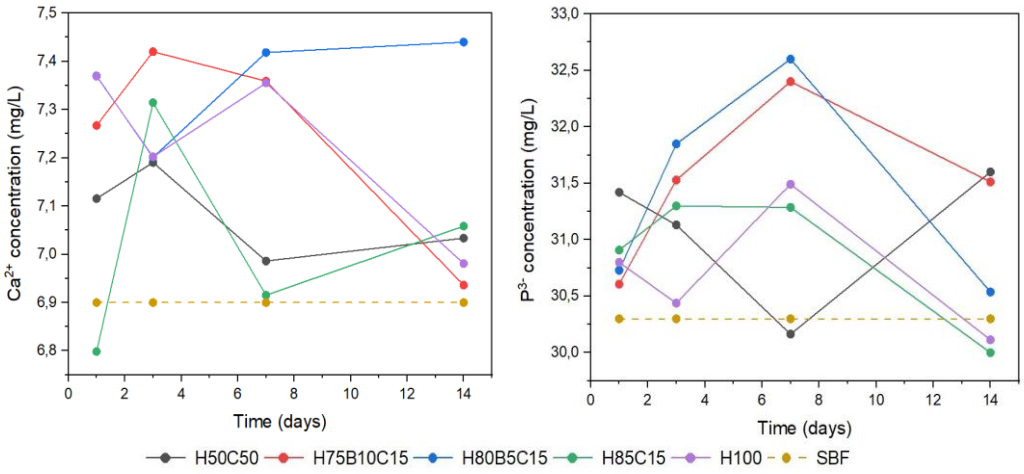

Figure 3.14 - Variation of Ca^{2+} concentration (a) and P^{3-} concentration (b) in SBF solution for cryogels H50C50, H75B10C15, H80B5C15, H85C15 and H100 after 1, 3, 7 and 14 days.

This can also be verified in Figure 3.15 where no significant variation of Ca/P ratios is observed through the SBF immersion time (1st , 3rd, 7th and 14th day) as well as between before and after immersion, calculated based on quantification EDS results present in **Figure B.3.2.1** to **Figure B.3.2.5**, section B.3.2 (referent to before immersion) and present in **Figure B.5.2.1** to **Figure B.5.2.20**, section B.5.2 (referent to after immersion).

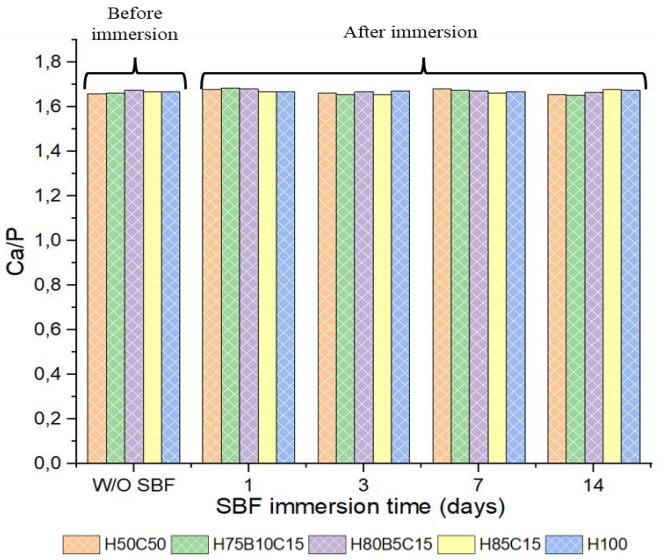

Figure 3.15 - Ca/P ratios of cryogels, quantified by EDS analysis, before (dry cryogels) and after SBF immersion. W/O SBF – without SBF

Nevertheless, from this assay, some conclusions can be drawn, such as the presence of higher concentrations of Ca^{2+} and P^{3-} in the SBF between the 3rd and 7th days from the cryogels H75B10C15 and H80B5C15. This presence is consistent with the expected behavior of the β-TCP present in the samples, particularly regarding its low stability and excellent biodegradability. Thus, the samples containing β-TCP may be contributing to the continuous and gradual release of the ions, promoting a more efficient and controlled dissolution essential for facilitating bone growth, compared to the Hap NW/CNF composites or those containing only Hap NW. After this period, only H75B10C15 tends to start retaining both ions, possibly indicating an attempt to form apatite, thereby exhibiting dual behavior.

Considering the quantification and mapping EDS analysis represented in Figures in section B.5.2, it is evident that there are ions Ca^{2+} and P^{3-} originating solely from the structure of Hap NW and/or β-TCP, as well as the incorporation of sodium and chlorine. The presence of crystals typical of the cubic lattice of sodium chloride, derived from the SBF and integrated in CNF structure, occurs in all cryogels that contain CNF, but with more intensely in the H50C50 cryogel (**Figure B.5.2.1**, **Figure B.5.2.6**, **Figure B.5.2.11** and **Figure B.5.2.16** comparing with **Figure B.3.2.1 - Quantification and mapping EDS analysis of the H50C50 cryogel (control sample not immersed in SBF)Figure B.3.2.1**, section B.3.2), where the amount of CNF is significant (50% by weight), increasing from the 1st to the 14th day. The high superficial area of CNF and the fact that these Na^{+} and Cl^{-} ions can interact with the functional groups on the surface of the CNF, namely the -OH and -COOH groups, until saturation is reached, making it difficult to observe other structures in some areas of the SEM images. Additionally, the rough morphology of the samples may also hinder the observation and distinction of deposited apatites in the case of relatively small crystal formation, which is further limited by the maximum sharp magnification of the SEM [112].

3.4.5 Mechanical tests

The graphs shown in Figure 3.16 represent the results of the uniaxial compression tests of the cryogels: C100, H50C50, H85C15, H80B5C15, and H75B10C15, highlighting the variations in mechanical properties, such as the modulus of elasticity as a function of the composition and the proportion of each component.

By observing the graphs, it is possible to verify that the linear phase and the plateau overlap, which can be attributed to the low density and high porosity of these foams. Furthermore, the tests reveal the viscoelastic nature of the material, characterized by the quick response to stress application and more prolonged deformation in the initial phase, suggesting that part of the applied mechanical energy is absorbed by the material in the form of heat or internal friction [113], [114].

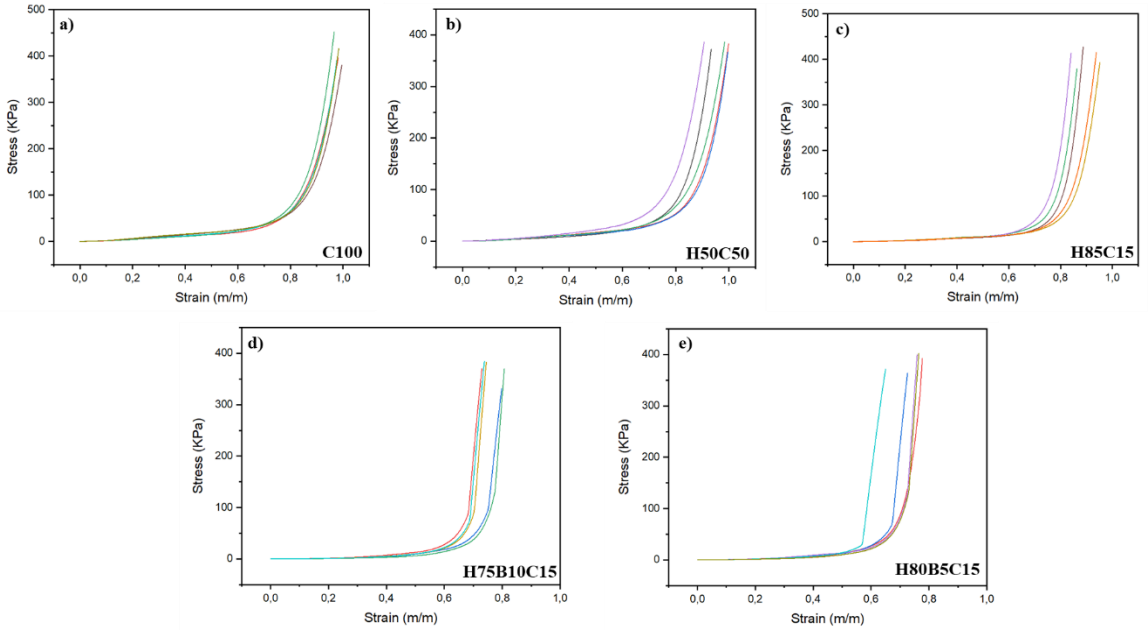

Figure 3.16 - Stress-strain curve from cryogels obtained in uniaxial compression test. a) C100; b) H50C50; c) H85C15; d) H75B10C15; e) H80B5C15.

The **Table B.6.1**, section B.6 and Figure 3.17 represent the Young's modulus for the various replicas calculated based in equation 2.2 from section 2.2.5, as well as the mean and corresponding standard deviations for each cryogel. These values reveal the existence of three distinct behaviors, according to the amount of each component used in the cryogel formulation. A decrease in Young's modulus is observed with an increase in the amount of β-TCP, which can be attributed to the more brittle and less rigid nature of this component and its nanoparticles morphology. The other two behaviors are associated with two groups of cryogels: one where Hap predominates (H75B10C15, H80B5C15 and H85C15) and another where CNF dominates (C100 and H50C50). Together, they allow us to verify that increasing the amount of CNF and Hap leads to an increase in Young's modulus, as they impart greater stiffness to the material due to their structural properties and higher mechanical strength.

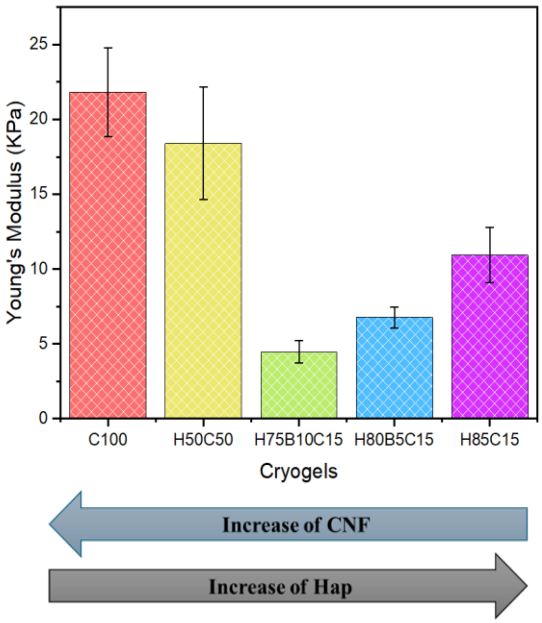

Figure 3.17 - Histogram representative of the Young's modulus means of each cryogel with the associated uncertainty.

The behavior of CNF is opposite to that described in Guo W. *et al.* (2018) [115], where Hap NW/CNF composites are evaluated. However, the presence of crosslinkers such as polyethyleneimine

and 3-glycidoxypropyltrimethoxysilane used in the formulation of these cryogels may justify this difference in behavior, as these crosslinkers directly influence the chemical interactions (covalent bonds) and matrix structure. As a result, this interaction leads to a distinct linear behavior in our cryogels, where the absence of such crosslinkers may have led to less robust mechanical behavior.

It is important to note that few studies have been carried out on low-density foams with the components used in this dissertation, making it difficult to compare the results obtained. Additionally, the fact that compression tests could not be performed with the cryogel of Hap alone due to its high fragility imposed a limitation on the study. Another important aspect to consider is that the tests were limited to only five samples, which, although providing important preliminary data, may not be sufficient to ensure high statistical robustness.

Although several studies have been conducted with different scaffolds for use in bone regeneration, the ideal Young's modulus for such applications is still uncertain, with only the suggestion that it should be less than 1 GPa [116].The values obtained from the tested cryogels (< 100 KPa) are far from this value, indicating that, while promising in terms of biocompatibility, they still need to be adjusted to achieve the necessary stiffness without compromising controlled degradation, which is essential for effective bone regeneration.

3.4.6 DSC/TG analysis

Through the DSC-TG assays, the curves represented in the graphs of Figure 3.18 were obtained for the different cryogels, providing information about thermal stability of the materials and possible presence of phase transitions.

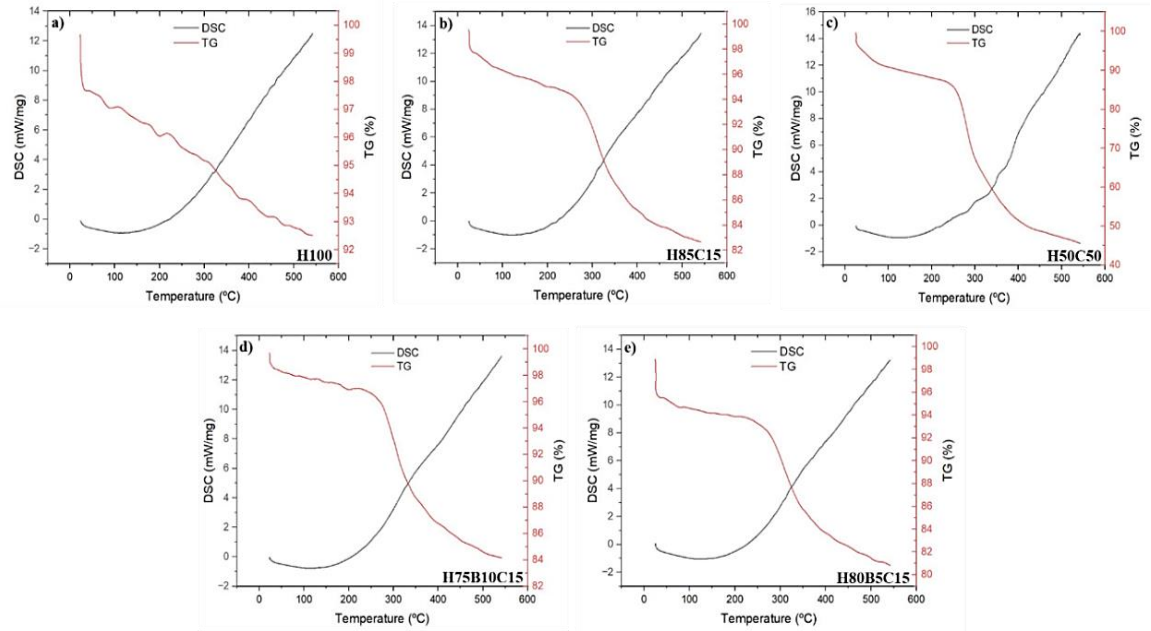

Figure 3.18 - Representative curves of DSC (black curve) and TG (red curve) assays according to temperature for each cryogel.

The TG curve of H100 shows little mass loss (around 7-8%) up to 600 °C, indicating high thermal stability. However, the cryogels with CNF show more significant mass loss, particularly in samples with larger amounts of CNF, such as H50C50, which loses almost 60% of its mass, demonstrating that CNF

has low thermal stability, degrading in a temperature range 200-380 °C has it was expected from a polymeric material [117][118]. Comparing the cryogels: H75B10C15 and H80B5C15, it can be concluded that a higher amount of β-TCP leads to more moderate mass loss, with greater thermal stabilization.

Observing the DSC curves, H100 exhibits a smooth endothermic peak, suggesting that the lyophilized Hap does not undergo significant phase changes until high temperatures (>1000ºC). When adding CNF in large amounts (H50C50), endothermic peaks are observed between 250 and 400 °C, which may be related to the degradation of CNF. Representative peaks for phase transition cannot be observed in the samples with β-TCP, as it only transforms into α-TCP at temperatures above 1125 °C.

In general, these analyses suggest that the combination of Hap with β-TCP may be more effective for thermal resistance, while CNF reduces this stability at high temperatures, not occurring in biological applications.

3.4.7 BET analysis

The graphs in Figure 3.19 represent the isothermal adsorption and desorption curves of each cryogel, indicating that they follow a similar pattern of type III, namely a), b), and e), according to the IUPAC (International Union of Pure and Applied Chemistry). This non-linear pattern is characteristic of non-porous or macroporous adsorbents, where the interactions between the adsorbent and the adsorbate are weak, resulting in minimal initial adsorption without the formation of a clear monolayer. As the pressure increases, intermolecular adsorption interactions become predominant, favoring adsorption in successive layers. The amount adsorbed remains finite at saturation pressure (i.e., at $p/p_o = 1$), even though multilayer adsorption continues up to the limit of the adsorbent surface capacity.

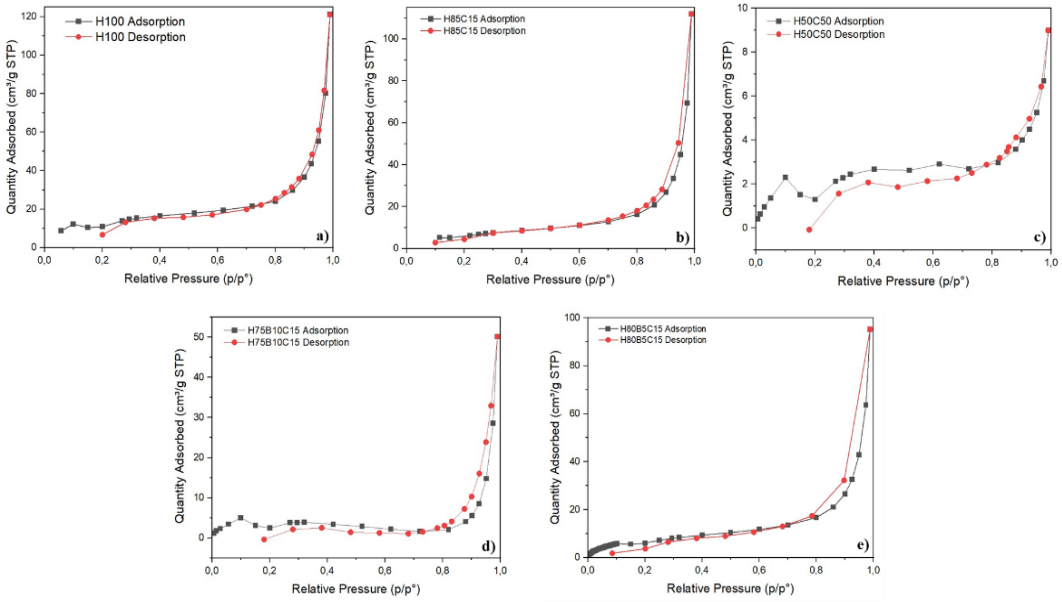

Figure 3.19 - Isothermal adsorption and desorption curves for the different cryogels obtained using the BET method: a) H100; b) H85C15; c) H50C50; d) H75B10C15; e) H80B5C15.

This process is visibly reversible without significant hysteresis when the pressure decreases, due to the weak interactions between the adsorbent and the adsorbate. In this case, and considering **Figure**

B.7.1, section B.7, resulting from observation using a binocular stereo microscope and **Figure 3.10**, section 3.4.1 from the SEM of the cryogels (H50C50: image e1 and e2; H75B10C15: image i1 and i2; H80B5C15: image j1 and j2; H85C15: image g1 and g2; H100: image l1 and l2), we can verify that they are macroporous, with pores > 50 nm [119]. However, the quantity value of porosity for each cryogel cannot be calculated by BJH (Barrett-Joyner-Halenda) method because it is out of range (2-50 nm) and the cryogels have low density for the equipment, having the necessity to adopt another technique.

The isothermal adsorption and desorption curves presented in graphs c) and d) of Figure 3.19 show an irregular and inconclusive behavior, not following typical adsorption isotherm profiles. This suggests complexity in the interaction mechanism between the cryogel and the adsorbate, as well as in the superficial area calculation due to the difficulty in identifying the initial linear section or its absence.

The surface area of the cryogels H100, H85C15, and H80B5C15 were calculated using the BET equation 3.7, which determines multilayer adsorption:

$$\frac{p/p_0}{V_{ads}(1-p/p_0)} = \frac{1}{V_m C} + \frac{C-1}{V_m C}\frac{p}{p_0} \qquad \textbf{(3.7)}$$

where p is the partial pressure of the adsorbate, p_0 is the saturation pressure of the adsorbate (nitrogen), V_{ads} is the volume of gas adsorbed at the pressure of p/p_0, V_m is the monolayer capacity, and C is the BET constant (exponentially related to the energy of monolayer adsorption).

In the p/p_0 range between 0.05 and 0.3, the values of V_m and the constant C are obtained from the following linear equations for each cryogel, represented in Figure 3.20 and Table 3.3.

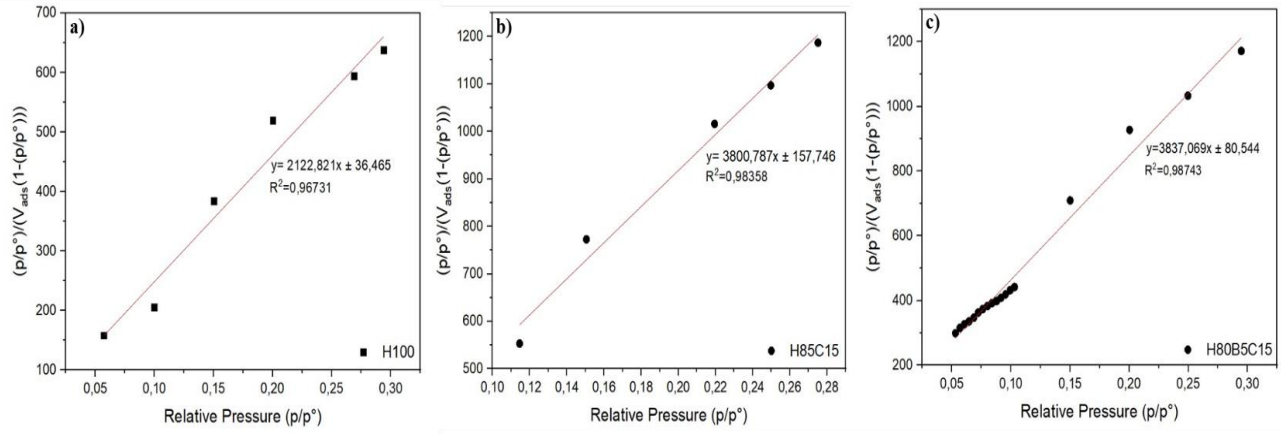

Figure 3.20 - Linear regression obtained in the p/p_0 range between 0.05 and 0.3 using the BET equation 3.7 for the cryogels: a) H100; b) H85C15; c) H80B5C15.

Considering the C values obtained for the cryogels H85C15 and H80B5C15 in Table 3.3, which are below 50, it is observed that the start of the almost linear middle section cannot be identified as a single point on the isotherm. Therefore, there is an overlap of monolayer and multilayer adsorption, making the precise interpretation of V_m questionable [119].

Finally, the surface area, A, of the cryogels was calculated using the following equation 3.8, with the results presented in Table 3.3.

$$A = V_m \times N_A \times a_m \qquad \textbf{(3.8)}$$

where N_A is Avogadro's number (6.022×10^{23} molecules/mol), a_m is the area occupied by an adsorbed molecule (for example, for nitrogen at 77 K, a_m=16.2 $A^{\circ 2}$).

Table 3.3 - Values of V_m, C, and the surface area of the cryogels.

Cryogel	V_m (cm^3/ g STP)	C	Area (m^2/g)
H100	4.6×10^{-4}	59.2	45.2 ± 4.9
H85C15	2.5×10^{-4}	25.1	24.6 ± 2.1
H80B5C15	2.6×10^{-4}	48.6	24.9 ± 0.8

The addition of CNF to the cryogels significantly reduces the specific surface area and consequently the adsorption capacity of the material compared to pure freeze-dried Hap, indicating that the cellulose nanofibers fill or block the pores, resulting in a denser and less porous structure.

4

CONCLUSION

The main objective of this dissertation was to produce composite cryogels of Hap NW incorporating β-TCP nanoparticles and CNF for application in bone tissue regeneration.

Each of the cryogel components were initially characterized. Starting with the Hap NW produced by the solvothermal method, it was possible to observe through SEM that the ultralong nanofibers appeared to exhibit greater flexibility compared to commercial Hap. Furthermore, its hexagonal phase was detected by XRD, revealing that an incomplete reaction had occurred, with some reagents remaining after washing, such as the presence of small peaks related to $CaCl_2$ and $NaH_2PO_4 \cdot 2H_2O$. ATR-FTIR analysis concluded that it exhibited vibration bands of the ions PO_4^{3-} and OH^- characteristic of the Hap spectrum, as well as carbonate groups similar to those in bone mineral, justifying the possible increase in the Ca/P ratio obtained by ICP-OES. Regarding β-TCP, synthesized by the sol-gel method, spherical and irregular nanoparticles were observed through SEM, and a rhombohedral structure was identified through XRD, allowing for the distinction of the β phase over the α phase. Small peaks representing the reagents KH_2PO_4 and $Ca(NO_3)_2 \cdot 4H_2O$ were also visible. The ATR-FTIR analysis allowed for the observation of the characteristic vibrations of the PO_4^{3-} group in the β-TCP spectrum. A Ca/P ratio higher than expected was detected, possibly due to the loss of phosphate groups during calcination at 800 ºC. As the CNF used was commercial, SEM and ATR-FTIR were performed to verify the presence of long, flexible fibers and their characteristic functional groups, respectively. Thus, despite the minor impurities and deviations observed, all components demonstrated promising properties that do not compromise their use in composites aimed at bone regeneration.

Subsequently, different composites were developed through dispersion and subsequent freezing, followed by freeze-drying, consisting of one or more of these three elements in different concentrations (mg/mL). To select those with the best characteristics, their morphology and stability was observed both by SEM and naked eye, respectively, as well as their composition and molecular structure by ATR-FTIR. The cryogels with only Hap NW and β-TCP were excluded due to their lack of firmness and fragility, requiring the addition of a third component, such as CNF as a structural element. Therefore, only H50C50, H75B10C15, H80B5C15, H85C15, and H100 were selected, as they not only exhibited the representative functional groups of each element, indicating chemical conformity without significant changes in the molecular structure of the components, but also appeared to have strong cohesion. Thus, these were selected for future comparison effects of each characterization method.

Cytotoxicity tests were conducted on both the components and the cryogels themselves, at different concentrations, 20 mg/mL and 5 mg/mL, respectively. It was found that all were non-cytotoxic, except for cellulose at high concentrations (≥5 mg/mL), likely due to the possible absorption of nutritional components from the culture medium by cellulose, essential for cell survival, or changes in the aggregation and dispersion of CNF, indicating that values below this can be tested *in vivo*. This highlights the need to establish reasonable exposure levels of CNF and to supplement components in the culture medium when using concentrations above the mentioned value. The cryogels showed no signs of cytotoxicity since the content of CNF was low enough.

Based on the bioactivity tests, ICP-OES showed no significant variations in the concentrations of Ca^{2+} and P^{3-} in the SBF regarding their release and retention by the cryogels. SEM images and EDS mapping corroborate this fact, showing the absence of substantial deposition of these ions in the cryogels, indicating a possible lack of bioactivity. The presence of ions such as Na^{+} and Cl^{-} incorporated on the surface of the CNF, along with the rough morphology of the samples and the clear and limited maximum magnification of the SEM, contribute to the difficulty in observing deposited apatites.

Through the results obtained from mechanical tests, it was determined that the Young's modulus was below 100 KPa for all cryogels, demonstrating three types of behavior: the increase in β-TCP reduced the Young's modulus, while the increase in Hap NW and CNF increased it, contrary to studies that present a linear behavior with the increase of Hap NW. These values are significantly low compared to the literature, indicating the need to add a crosslinking agent or replace one of the components of the cryogel.

The DSC-TG analysis shows that the combination of Hap and β-TCP is more efficient in increasing the thermal resistance of the cryogels, as it leads to a lower and more moderate mass loss, while CNF compromises stability around 200-350 ºC. However, a broader temperature range in the DSC-TG analysis will allow the verification of certain phase transitions of the synthesized β-TCP and an assessment of the degradation behavior of Hap, providing a more comprehensive view of the thermal stability of the cryogels at high temperatures.

The BET results obtained from the isothermal adsorption and desorption curves indicate that most cryogels follow the type III pattern according to IUPAC, characteristic of macroporous materials, specifically greater than 50 nm, with weak interactions between the adsorbent and adsorbate. However, the isothermal curves of the H50C50 and H75B10C15 cryogels exhibited irregular behaviors, with more complex interaction mechanisms in the monolayer adsorption capacity. Furthermore, due to the method used exceeding the appropriate analysis range for these cryogels, it became impossible to accurately calculate the porosity and specific surface area of some, due to the low sample amount and the difficulty in identifying the initial linear section or its absence, respectively. It is necessary to adopt another technique. Mercury intrusion porosimetry is a technique that applies high pressures to force the entry of mercury into the pores of the material. However, this process can cause structural collapse or permanent deformation in low-density cryogels, which have a delicate and porous three-dimensional matrix, making it unsuitable for such materials. An alternative would be Computed Axial Tomography (CAT), which provides detailed three-dimensional images of the internal microstructure of the cryogels, as well as a more precise and quantitative analysis of porosity and pore distribution, offering a better understanding of the structural properties of the material.

In summary, the composite cryogels of Hap NW, along with β-TCP nanoparticles and CNF, exhibit favorable characteristics for bone regeneration, such as flexibility, non-cytotoxicity, and macroporosity, the latter being essential for nutrient circulation and cell growth. However, in addition to the aspects that require improvement mentioned earlier, it is crucial to conduct further tests, such as assessing cell adhesion and proliferation, to verify biological compatibility and the ability to support the formation of new tissues, as well as *in vivo* testing.

BIBLIOGRAPHY

[1] X. Feng, "Chemical and Biochemical Basis of Cell-Bone Matrix Interaction in Health and Disease," *Curr. Chem. Biol.*, vol. 3, no. 2, pp. 189–196, 2009, doi: 10.2174/187231309788166398.

[2] A. G. Abdelaziz *et al.*, "A Review of 3D Polymeric Scaffolds for Bone Tissue Engineering : Principles , Fabrication Techniques , Immunomodulatory Roles , and Challenges," *Bioengineering*, vol. 10, p. 204, 2023, doi: 10.3390/bioengineering10020204.

[3] N. Reznikov, M. Bilton, L. Lari, M. M. Stevens, and R. Kröger, "Fractal-like hierarchical organization of bone begins at the nanoscale," *Science (80-.).*, vol. 360, no. 6388, 2018, doi: 10.1126/science.aao2189.

[4] P. Fratzl and R. Weinkamer, "Nature's hierarchical materials," *Prog. Mater. Sci.*, vol. 52, no. 8, pp. 1263–1334, 2007, doi: 10.1016/j.pmatsci.2007.06.001.

[5] S. Weiner and H. D. Wagner, "The material bone: Structure-mechanical function relations," *Annu. Rev. Mater. Sci.*, vol. 28, no. 1, pp. 271–298, 1998, doi: 10.1146/annurev.matsci.28.1.271.

[6] C. Gao, S. Peng, P. Feng, and C. Shuai, "Bone biomaterials and interactions with stem cells," *Bone Res.*, vol. 5, pp. 1–33, 2017, doi: 10.1038/boneres.2017.59.

[7] I. Lázár, L. Čelko, and M. Menelaou, "Aerogel-Based Materials in Bone and Cartilage Tissue Engineering—A Review with Future Implications," *Gels*, vol. 9, no. 9, 2023, doi: 10.3390/gels9090746.

[8] M. Ansari, "Bone tissue regeneration: biology, strategies and interface studies," *Prog. Biomater.*, vol. 8, no. 4, pp. 223–237, 2019, doi: 10.1007/s40204-019-00125-z.

[9] J. S. Kenkre and J. H. D. Bassett, "The bone remodelling cycle," *Ann. Clin. Biochem.*, vol. 55, no. 3, pp. 308–327, 2018, doi: 10.1177/0004563218759371.

[10] V. C. Carriero, L. Di Muzio, S. Petralito, M. A. Casadei, and P. Paolicelli, "Cryogel Scaffolds for Tissue-Engineering: Advances and Challenges for Effective Bone and Cartilage Regeneration," *Gels*, vol. 9, no. 12, 2023, doi: 10.3390/gels9120979.

[11] G. Horvat, M. Pantić, Ž. Knez, and Z. Novak, "A Brief Evaluation of Pore Structure Determination for Bioaerogels," *Gels*, vol. 8, no. 7, pp. 1–18, 2022, doi: 10.3390/gels8070438.

[12] V. M. Gun'ko, I. N. Savina, and S. V. Mikhalovsky, "Cryogels: Morphological, structural and adsorption characterisation," *Adv. Colloid Interface Sci.*, vol. 187–188, pp. 1–46, 2013, doi: 10.1016/j.cis.2012.11.001.

[13] E. BAYIR, "Comparative Evaluation of Alginate-Gelatin Hydrogel, Cryogel, and Aerogel

Beads as a Tissue Scaffold," *Sak. Univ. J. Sci.*, vol. 27, no. 2, pp. 335–348, 2023, doi: 10.16984/saufenbilder.1098637.

[14] M. P. Nikolova and M. S. Chavali, "Recent advances in biomaterials for 3D scaffolds: A review," *Bioact. Mater.*, vol. 4, pp. 271–292, 2019, doi: 10.1016/j.bioactmat.2019.10.005.

[15] N. Abbasi, S. Hamlet, R. M. Love, and N. T. Nguyen, "Porous scaffolds for bone regeneration," *J. Sci. Adv. Mater. Devices*, vol. 5, no. 1, pp. 1–9, 2020, doi: 10.1016/j.jsamd.2020.01.007.

[16] S. Lozinsky, VI, Vainerman, ES & Rogozhin, "Study of cryostructurization of polymer systems .," *Colloid Polym. Sci.*, vol. 260, pp. 776–780, 1982, doi: https://doi.org/10.1007/BF01452068.

[17] V. I. Lozinsky *et al.*, "Use of PVA-cryogel entrappedCitrobacter intermedius cells for continuous production of 3-fluoro-L-tyrosine.," *Biotechnol. Lett.*, vol. 11, pp. 43–48, 1989, doi: https://doi.org/10.1007/BF01026784.

[18] A. Sharma, S. Bhat, T. Vishnoi, V. Nayak, and A. Kumar, "Three-dimensional supermacroporous carrageenan-gelatin cryogel matrix for tissue engineering applications," *Biomed Res. Int.*, vol. 2013, 2013, doi: 10.1155/2013/478279.

[19] D. B. Raina and A. Kumar, *Cryogels and Related Research: A glance over the past few decades. Supermacroporous Cryogels: Biomedical and Biotechnological Applications*. CRC Press, 2016.

[20] S. Odabas, "Collagen – carboxymethyl cellulose – tricalcium phosphate multi-lamellar cryogels for tissue engineering applications : Production and characterization," *J. Bioact. Compat. Polym.*, vol. 31(4), pp. 411–422, 2016, doi: 10.1177/0883911515627472.

[21] L. Gu, J. Zhang, L. Li, Z. Du, Q. Cai*, and X. Yang, "Hydroxyapatite nanowire composited gelatin cryogel with improved mechanical properties and cell migration for bone regeneration.," *Biomed. Mater.*, vol. 14(4), 2019, doi: 10.1088/1748-605X/ab1583.

[22] F. V. Ferreira *et al.*, "Nanocellulose/bioactive glass cryogels as scaffolds for bone regeneration," *R. Soc. Chem.*, vol. 11, pp. 19842–19849, 2019, doi: 10.1039/c9nr05383b.

[23] B. Wang *et al.*, "Fabrication and properties of PLA / β -TCP scaffolds using liquid crystal display (LCD) photocuring 3D printing for bone tissue engineering," *Front. Bioeng. Biotechnol.*, vol. 12, no. 1273541, pp. 1–13, 2024, doi: 10.3389/fbioe.2024.1273541.

[24] D. Zhanbassynova, A.; Mukasheva, F.; Abilev, M.; Berillo, D.; Trifonov, A.; Akilbekova, "Impact of Hydroxyapatite on Gelatin/Oxidized Alginate 3D-Printed Cryogel Scaffolds," *Gels*, vol. 10(6), p. 406, 2024, doi: 10.3390/gels10060406.

[25] Razavi M. el al., "Three-dimensional cryogels for biomedical applications," *J Biomed Mater Res A.*, vol. 107(12), pp. 2736–2755, 2019, doi: 10.1002/jbm.a.36777.

[26] H. Omidian, S. Dey Chowdhury, and N. Babanejad, "Cryogels: Advancing Biomaterials for Transformative Biomedical Applications," *Pharmaceutics*, vol. 15, no. 7, 2023, doi: 10.3390/pharmaceutics15071836.

[27] D. B. Raina, H. Isaksson, A. K. Teotia, L. Lidgren, M. Tägil, and A. Kumar, "Biocomposite macroporous cryogels as potential carrier scaffolds for bone active agents augmenting bone regeneration," *J. Control. Release*, vol. 235, pp. 365–378, 2016, doi: 10.1016/j.jconrel.2016.05.061.

[28] K. R. Hixon, T. Lu, and S. A. Sell, "A comprehensive review of cryogels and their roles in tissue engineering applications," *Acta Biomater.*, vol. 62, pp. 29–41, 2017, doi: 10.1016/j.actbio.2017.08.033.

[29] R. Mishra, S. K. Goel, K. C. Gupta, and A. Kumar, "Biocomposite cryogels as tissue-engineered biomaterials for regeneration of critical-sized cranial bone defects," *Tissue Eng. - Part A*, vol. 20, no. 3–4, pp. 751–762, 2014, doi: 10.1089/ten.tea.2013.0072.

[30] K. R. Hixon, C. T. Eberlin, P. U. Kadakia, S. H. McBride-Gagyi, E. Jain, and S. A. Sell, "A comparison of cryogel scaffolds to identify an appropriate structure for promoting bone regeneration," *Biomed. Phys. Eng. Express*, vol. 2, no. 3, 2016, doi: 10.1088/2057-1976/2/3/035014.

[31] M. Sawada, K. Sridhar, Y. Kanda, and S. Yamanaka, "Pure hydroxyapatite synthesis originating from amorphous calcium carbonate," *Sci. Rep.*, vol. 11, no. 1, pp. 1–9, 2021, doi: 10.1038/s41598-021-91064-y.

[32] M. U. Munir, S. Salman, A. Ihsan, and T. Elsaman, "Synthesis, Characterization, Functionalization and Bio-Applications of Hydroxyapatite Nanomaterials: An Overview," *Int. J. Nanomedicine*, vol. 17, pp. 1903–1925, 2022, doi: 10.2147/IJN.S360670.

[33] A. Abburi and V. R. Abburi, "Controlled synthesis of hydroxyapatite nanoparticles," *Proc. 14th Annu. IEEE Int. Conf. Nano/Micro Eng. Mol. Syst. NEMS 2019*, pp. 300–303, 2019, doi: 10.1109/NEMS.2019.8915677.

[34] A. Serban *et al.*, "Interplay of the hydroxyapatite structure and morphology with the thermodynamic parameters at hydroxyapatite/protein interface," *Ceram. Int.*, vol. 49, no. 22, pp. 34734–34741, 2023, doi: 10.1016/j.ceramint.2023.08.140.

[35] A. Shah, S. Patel, J. Pathak, N. Swain, and S. Shah, "An insight into diagnostically challenging salivary gland malignancy with case report: Polymorphous low grade adenocarcinoma," *J. Dent. Res. Sci. Dev.*, vol. 1, pp. 20–23, 2014, doi: 10.4103/2348-3407.126135.

[36] Y. Zhang, Y. J. Zhu, and H. P. Yu, "Microwave-Assisted Hydrothermal Rapid Synthesis of Ultralong Hydroxyapatite Nanowires Using Adenosine 5′-Triphosphate," *Molecules*, vol. 27, no. 15, 2022, doi: 10.3390/molecules27155020.

[37] Z. Abbas, M. Dapporto, A. Tampieri, and S. Sprio, "Toughening of bioceramic composites for bone regeneration," *J. Compos. Sci.*, vol. 5, no. 10, 2021, doi: 10.3390/jcs5100259.

[38] R. Ahmed, S. El-Nahas, and A. Mohamed, "Structural and Morphological Features of Hydroxyapatite Nanoparticles from Different Calcium Resources," *Aswan Univ. J. Environ. Stud.*, vol. 3, no. 3, pp. 313–323, 2022, doi: 10.21608/aujes.2022.142530.1070.

[39] G. Wei and P. X. Ma, "Structure and properties of nano-hydroxyapatite/polymer composite scaffolds for bone tissue engineering," *Biomaterials*, vol. 25, no. 19, pp. 4749–4757, 2004, doi: 10.1016/j.biomaterials.2003.12.005.

[40] S. J. Kalita, A. Bhardwaj, and H. A. Bhatt, "Nanocrystalline calcium phosphate ceramics in biomedical engineering," *Mater. Sci. Eng. C*, vol. 27, no. 3, pp. 441–449, 2007, doi: 10.1016/j.msec.2006.05.018.

[41] N. Y. Mostafa and P. W. Brown, "Computer simulation of stoichiometric hydroxyapatite: Structure and substitutions," *J. Phys. Chem. Solids*, vol. 68, no. 3, pp. 431–437, 2007, doi: 10.1016/j.jpcs.2006.12.011.

[42] S. Teixeira *et al.*, "Physical characterization of hydroxyapatite porous scaffolds for tissue engineering," *Mater. Sci. Eng. C*, vol. 29, no. 5, pp. 1510–1514, 2009, doi: 10.1016/j.msec.2008.09.052.

[43] L. Guo, M. Huang, and X. Zhang, "Effects of sintering temperature on structure of hydroxyapatite studied with Rietveld method," *J. Mater. Sci. Mater. Med.*, vol. 14, pp.

817–822, 2003, doi: 10.1023/a:1025048724330.
[44] E. Fiume, G. Magnaterra, A. Rahdar, E. Verné, and F. Baino, "Hydroxyapatite for biomedical applications: A short overview," *Ceramics*, vol. 4, no. 4, pp. 542–563, 2021, doi: 10.3390/ceramics4040039.
[45] D. S. Gomes, A. M. C. Santos, G. A. Neves, and R. R. Menezes, "A brief review on hydroxyapatite production and use in biomedicine," *Ceramica*, vol. 65, no. 374, pp. 282–302, 2019, doi: 10.1590/0366-69132019653742706.
[46] A. R. Noviyanti *et al.*, "Synthesis of hydroxyapatite nanowires (HAp NWs) from eggshell by solvothermal method using oleic acid as soft-template," *Emergent Mater.*, vol. 7, no. 4, pp. 1647–1655, 2024, doi: 10.1007/s42247-024-00716-y.
[47] A. Herrera *et al.*, "Cementless hydroxyapatite coated hip prostheses," *Biomed Res. Int.*, vol. 2025, 2015, doi: 10.1155/2015/386461.
[48] X. Wang, S. Huang, and Q. Peng, "Metal Ion-Doped Hydroxyapatite-Based Materials for Bone Defect Restoration," *Bioengineering*, vol. 10, no. 12, 2023, doi: 10.3390/bioengineering10121367.
[49] X. Mo, D. Zhang, K. Liu, X. Zhao, X. Li, and W. Wang, "Nano-Hydroxyapatite Composite Scaffolds Loaded with Bioactive Factors and Drugs for Bone Tissue Engineering," *Int. J. Mol. Sci.*, vol. 24, no. 2, 2023, doi: 10.3390/ijms24021291.
[50] R. S. Syafira, M. J. Devi, S. Gaffar, and Y. W. Hartati, "Immobilization of Biomolecules on Hydroxyapatite and Its Composites in Biosensor Application: A Review," *Biointerface Res. Appl. Chem.*, vol. 13, no. 5, pp. 1–17, 2023, doi: 10.33263/BRIAC135.499.
[51] Y. G. Zhang, Y. J. Zhu, F. Chen, and J. Wu, "Ultralong hydroxyapatite nanowires synthesized by solvothermal treatment using a series of phosphate sodium salts," *Mater. Lett.*, vol. 144, pp. 135–137, 2015, doi: 10.1016/j.matlet.2015.01.031.
[52] P. J. Thomas Reardon, A. D. Handoko, L. Li, J. Huang, and J. Tang, "Dimensionally and compositionally controlled growth of calcium phosphate nanowires for bone tissue regeneration," *J. Mater. Chem. B*, vol. 1, no. 44, pp. 6170–6176, 2013, doi: 10.1039/c3tb21073a.
[53] M. Cao, Y. Wang, C. Guo, Y. Qi, and C. Hu, "Preparation of ultrahigh-aspect-ratio hydroxyapatite nanofibers in reverse micelles under hydrothermal conditions," *Langmuir*, vol. 20, no. 11, pp. 4784–4786, 2004, doi: 10.1021/la0498197.
[54] C. S. Choy *et al.*, "Surface Modified β-Tricalcium phosphate enhanced stem cell osteogenic differentiation in vitro and bone regeneration in vivo," *Sci. Rep.*, vol. 11, no. 1, pp. 1–14, 2021, doi: 10.1038/s41598-021-88402-5.
[55] S. L. O. Costa, P. F. Silva, G. K. G. Carvalho, Y. B. A. Almeida, J. R. S. Farias, and A. S. N. Braga, "A Brief review of Beta Tricalcium Phosphate (β-TCP) Doped with Metal Ions," *Am. J. Eng. Res.*, vol. 10, no. 8, pp. 333–344, 2021.
[56] K. Matsunaga, T. Kubota, K. Toyoura, and A. Nakamura, "First-principles calculations of divalent substitution of Ca 2+ in tricalcium phosphates," *Elsevier*, vol. 23, pp. 329–337, 2015, doi: 10.1016/j.actbio.2015.05.014.
[57] X. Yin and M. J. Stott, "a- and b-tricalcium phosphate: A density functional study," *Phys. Rev.*, vol. 68(20), pp. 2052051–2052058, 2003, doi: 10.1103/PhysRevB.68.205205.
[58] M. D. Vlad, S. Gómez, M. Barracó, J. López, and E. Fernández, "Effect of the calcium to phosphorus ratio on the setting properties of calcium phosphate bone cements," *J. Mater. Sci. Mater. Med.*, vol. 23, no. 9, pp. 2081–2090, 2012, doi: 10.1007/s10856-012-

4686-3.
[59] G. A. Sblendorio, B. Le Gars Santoni, D. T. L. Alexander, P. Bowen, M. Bohner, and N. Döbelin, "Towards an improved understanding of the β-TCP crystal structure by means of 'checkerboard' atomistic simulations," *J. Eur. Ceram. Soc.*, vol. 43, no. 8, pp. 3746–3754, 2023, doi: 10.1016/j.jeurceramsoc.2023.02.036.
[60] D. Moreno, F. Vargas, J. Ruiz, and M. E. López, "Solid-state synthesis of alpha tricalcium phosphate for cements used in biomedical applications," *Bol. la Soc. Esp. Ceram. y Vidr.*, vol. 59, no. 5, pp. 193–200, 2020, doi: 10.1016/j.bsecv.2019.11.004.
[61] J. Jeong, J. H. Kim, J. H. Shim, N. S. Hwang, and C. Y. Heo, "Bioactive calcium phosphate materials and applications in bone regeneration," *Biomater. Res*, vol. 23:4, pp. 1–11, 2019, doi: 10.1186/s40824-018-0149-3.
[62] M. Bohner, B. Le, G. Santoni, and N. Döbelin, "β -Tricalcium Phosphate for Bone Substitution : Synthesis and Properties," *Acta Biomater.*, vol. 113, pp. 23–41, 2020, doi: 10.1016/j.actbio.2020.06.022.
[63] L. Liu, Y. Wu, C. Xu, S. Yu, X. Wu, and H. Dai, "Synthesis, characterization of nano- β -tricalcium phosphate and the inhibition on hepatocellular carcinoma cells," *J. Nanomater.*, vol. 2018, 2018, doi: 10.1155/2018/7083416.
[64] M. C. Farias, Rocha, G, "Beta tricalcium phosphate (β -TCP): A scientific and technological mapping," *Am. J. Eng. Res.*, vol. 11, pp. 125–138, 2022.
[65] B. Mirhadi, B. Mehdikhani, and N. Askari, "Synthesis of nano-sized β-tricalcium phosphate via wet precipitation," *Process. Appl. Ceram.*, vol. 5, no. 4, pp. 193–198, 2011, doi: 10.2298/pac1104193m.
[66] T. Windarti, A. Darmawan, and A. Marliana, "Synthesis of β-TCP by sol-gel method: Variation of Ca/P molar ratio," *IOP Conf. Ser. Mater. Sci. Eng.*, vol. 509, no. 1, 2019, doi: 10.1088/1757-899X/509/1/012147.
[67] K. P. Sanosh, M. C. Chu, A. Balakrishnan, T. N. Kim, and S. J. Cho, "Sol-gel synthesis of pure nano sized β-tricalcium phosphate crystalline powders," *Curr. Appl. Phys.*, vol. 10, no. 1, pp. 68–71, 2010, doi: 10.1016/j.cap.2009.04.014.
[68] R. Ghosh and R. Sarkar, "Synthesis and characterization of sintered beta-tricalcium phosphate: A comparative study on the effect of preparation route," *Mater. Sci. Eng. C*, vol. 67, pp. 345–352, 2016, doi: 10.1016/j.msec.2016.05.029.
[69] A. C. Marques, "Sol - Gel Process : An Overview," *Dep. Mater. Sci. Eng. Lehigh Univ.*, vol. 302, no. 317, pp. 2–15, 2007.
[70] Y. Zhang *et al.*, "Application of Nanocellulose-Based Aerogels in Bone Tissue Engineering: Current Trends and Outlooks," *Polymers.*, vol. 15, no. 10, pp. 1–26, 2023, doi: 10.3390/polym15102323.
[71] H. Kargarzadeh *et al.*, "Recent developments in nanocellulose-based biodegradable polymers, thermoplastic polymers, and porous nanocomposites," *Prog. Polym. Sci.*, vol. 87, pp. 197–227, 2018, doi: 10.1016/j.progpolymsci.2018.07.008.
[72] V. Calvo, C. Martínez-Barón, L. Fuentes, W. K. Maser, A. M. Benito, and J. M. González-Domínguez, "Nanocellulose: The Ultimate Green Aqueous Dispersant for Nanomaterials," *Polymers*, vol. 16, no. 12, 2024, doi: 10.3390/polym16121664.
[73] F. Barja, "Bacterial nanocellulose production and biomedical applications," *J. Biomed. Res.*, vol. 35, no. 4, pp. 310–317, 2021, doi: 10.7555/JBR.35.20210036.
[74] M. Janmohammadi *et al.*, "Cellulose-based composite scaffolds for bone tissue

engineering and localized drug delivery," *Bioact. Mater.*, vol. 20, pp. 137–163, 2023, doi: 10.1016/j.bioactmat.2022.05.018.

[75] M. Jorfi and E. J. Foster, "Recent advances in nanocellulose for biomedical applications," *J. Appl. Polym. Sci.*, vol. 132, no. 14, pp. 1–19, 2015, doi: 10.1002/app.41719.

[76] R. R *et al.*, "Bacterial nanocellulose: engineering, production, and applications," *Bioengineered*, vol. 12, no. 2, pp. 11463–11483, 2021, doi: 10.1080/21655979.2021.2009753.

[77] R. F. Santos *et al.*, "Nanofibrillated cellulose and its applications in cement-based composites: A review," *Constr. Build. Mater.*, vol. 288, p. 123122, 2021, doi: 10.1016/j.conbuildmat.2021.123122.

[78] Q. Song, W. T. Winter, B. M. Bujanovic, and T. E. Amidon, "Nanofibrillated cellulose (NFC): A high-value co-product that improves the economics of cellulosic ethanol production," *Energies*, vol. 7, no. 2, pp. 607–618, 2014, doi: 10.3390/en7020607.

[79] A. H. Tayeb, E. Amini, S. Ghasemi, and M. Tajvidi, "Cellulose nanomaterials-binding properties and applications: A review," *Molecules*, vol. 23, no. 10, pp. 1–24, 2018, doi: 10.3390/molecules23102684.

[80] Z. Xiong, Z. Yang, Y. Zhu, F. Chen, Y. Zhang, and R. Yang, "Ultralong Hydroxyapatite Nanowires-Based Paper Co-Loaded with Silver Nanoparticles and Antibiotic for Long-Term Antibacterial Benefit," *ACS Appl. Mater. Interfaces*, vol. 9(27), pp. 22212–22222, 2017, doi: 10.1021/acsami.7b05208.

[81] Z. Xiong, Y. Zhu, Z. Wang, Y. Chen, and H. Yu, "Tree-Inspired Ultralong Hydroxyapatite Nanowires-Based Multifunctional Aerogel with Vertically Aligned Channels for Continuous Flow Catalysis , Water Disinfection , and Solar Energy-Driven Water Purification," *Adv. Funct. Mater*, vol. 2106978, pp. 1–14, 2022, doi: 10.1002/adfm.202106978.

[82] C. A. Schneider, W. S. Rasband, and K. W. Eliceiri, "HISTORICAL commentary NIH Image to ImageJ : 25 years of image analysis," *Nat. Methods*, vol. 9, no. 7, pp. 671–675, 2012, doi: 10.1038/nmeth.2089.

[83] "INTERNATIONAL STANDARD ISO 10993 - 'Biological evaluation of medical devices, Part 5: Tests for in vitro cytotoxicity,'" 2009.

[84] "INTERNATIONAL STANDARD ISO / FDIS 23317 - Implants for surgery — In vitro evaluation for apatite-forming ability of implant materials, Part 6: Simulated body fluid.," 2007.

[85] T. K. Ã and H. Takadama, "How useful is SBF in predicting in vivo bone bioactivity ?," *Elsevier, Biomater.*, vol. 27, pp. 2907–2915, 2006, doi: 10.1016/j.biomaterials.2006.01.017.

[86] Y. Jiang, Y. Zhu, F. Chen, and J. Wu, "Solvothermal synthesis of submillimeter ultralong hydroxyapatite nanowires using a calcium oleate precursor in a series of monohydroxy alcohols," *Ceram. Int.*, vol. 41, no. 4, pp. 6098–6102, 2015, doi: 10.1016/j.ceramint.2014.12.122.

[87] J. R. Viana *et al.*, "Análise comparativa da síntese de hidroxiapatita via estado sólido Comparative analysis of solid state hydroxyapatite synthesis," *Rev. Mater.*, vol. 25, no. 1517–7076, 2020, doi: 10.1590/S1517-707620200001.0914.

[88] V. B. Miˇ, N. Bibi, and J. Stojanovi, "Electrochemical synthesis and characterization of hydroxyapatite powders," *Elsevier*, vol. 111, pp. 137–142, 2008, doi: 10.1016/j.matchemphys.2008.03.045.

[89] H. Zhao *et al.*, "Biomaterials The structural and biological properties of hydroxyapatite-modi fi ed titanate nanowire scaffolds," *Biomaterials*, vol. 32, no. 25, pp. 5837–5846, 2011, doi: 10.1016/j.biomaterials.2011.04.083.

[90] M. Markovic, B. O. Fowler, and M. S. Tung, "Preparation and Comprehensive Characterization of a Calcium Hydroxyapatite Reference Material," *J. Res. Natl. Inst. Stand. Technol.*, vol. 109, no. 6, pp. 553–568, 2004, doi: 10.6028/jres.109.042.

[91] N. Bano, S. S. Jikan, H. Basri, and S. Adzila, "XRD and FTIR study of A & B type carbonated hydroxyapatite extracted from bovine bone XRD and FTIR Study of A & B Type Carbonated Hydroxyapatite Extracted from Bovine Bone," *AIP Conf. Proc.*, vol. 020100, no. 2068, 2019, doi: 10.1063/1.5089399.

[92] K. Ishikawa, E. Garskaite, and A. Kareiva, "Sol–gel synthesis of calcium phosphate-based biomaterials—A review of environmentally benign, simple, and effective synthesis routes," *J. Sol-Gel Sci. Technol.*, vol. 94, no. 3, pp. 551–572, 2020, doi: 10.1007/s10971-020-05245-8.

[93] I. Grigoraviciute-puroniene, K. Tsuru, E. Garskaite, Z. Stankeviciute, A. Beganskiene, and K. Ishikawa, "A novel wet polymeric precipitation synthesis method for monophasic b -TCP," *Elsevier*, vol. 28, no. 9, pp. 2325–2331, 2017, doi: 10.1016/j.apt.2017.06.014.

[94] M. Aizawa, H. Ueno, K. Itatani, and I. Okada, "Syntheses of calcium-deficient apatite fibres by a homogeneous precipitation method and their characterizations," *Elsevier*, vol. 26, no. 4–5, pp. 501–507, 2006, doi: 10.1016/j.jeurceramsoc.2005.07.007.

[95] S. Hossain, A. A. Shaikh, N. Uddin, M. S. Bashar, and S. Ahmed, "β-tricalcium phosphate synthesized in organic medium for controlled release drug delivery application in bio-scaffolds," *R. Soc. Chem.*, vol. 4, no. 13, pp. 26435–26444, 2023, doi: 10.1039/d3ra04904c.

[96] D. Xidaki, P. Agrafioti, D. Diomatari, and A. Kaminari, "Synthesis of Hydroxyapatite, β-Tricalcium Phosphate and Biphasic Calcium Phosphate Particles to Act as Local Delivery Carriers of Curcumin: Loading, Release and In Vitro Studies," *Materials*, vol. 11, no. 4, p. 595, 2018, doi: 10.3390/ma11040595.

[97] A. Erdman, P. Kulpinski, and K. Olejnik, "Application of nanocomposite cellulose fibers with luminescent properties to paper functionalization," *Cellulose*, vol. 23, no. 3, pp. 2087–2097, 2016, doi: 10.1007/s10570-016-0943-9.

[98] T. Sultana, S. Sultana, H. P. Nur, and W. Khan, "Studies on Mechanical , Thermal and Morphological Properties of Betel Nut Husk Nano Cellulose Reinforced Biodegradable Polymer Composites," *J. Compos. Sci.*, vol. 4, no. 3, p. 83, 2020, doi: 10.3390/jcs4030083.

[99] S. Fujisawa, Y. Okita, H. Fukuzumi, T. Saito, and A. Isogai, "Preparation and characterization of TEMPO-oxidized cellulose nanofibril films with free carboxyl groups," *Carbohydr. Polym.*, vol. 84, no. 1, pp. 579–583, 2011, doi: 10.1016/j.carbpol.2010.12.029.

[100] A. Bayu, D. Nandiyanto, R. Oktiani, and R. Ragadhita, "How to Read and Interpret FTIR Spectroscope of Organic Material," *Indones. J. Sci. Technol.*, vol. 4, no. 1, pp. 97–118, 2019, doi: http://dx.doi.org/10.17509/ijost.v4i1.15806.

[101] B. Poyraz, A. Tozluoğlu, Z. Candan, A. Demir, and M. Yavuz, "Influence of PVA and silica on chemical , thermo-mechanical and electrical properties of Celluclast-treated nanofibrillated cellulose composites," *Int. J. Biol. Macromol.*, vol. 104, no. 7, pp. 384–392, 2017, doi: 10.1016/j.ijbiomac.2017.06.018.

[102] M. A. Jamilludin, I. K. H. Dinatha, A. I. Supii, J. Partini, D. L. Kusindarta, and Y. Yusuf, "Functionalized cellulose nanofibrils in carbonate- substituted hydroxyapatite nanorod-

based scaffold from long-spined sea urchin (Diadema setosum) shells reinforced with polyvinyl alcohol for alveolar bone tissue engineering Muhammad," *R. Soc. Chem.*, vol. 13, no. 46, pp. 32444–32456, 2023, doi: 10.1039/d3ra06165e.

[103] B. Abderrahim, E. Abderrahman, A. Mohamed, T. Fatima, and T. Abdesselam, "Kinetic Thermal Degradation of Cellulose , Polybutylene Succinate and a Green Composite : Comparative Study," *World J. Environ. Eng.*, vol. 3, no. 4, pp. 95–110, 2015, doi: 10.12691/wjee-3-4-1.

[104] O. Okay, "Cryogelation reactions and cryogels : principles and challenges," *Turkish J. Chem. Vol.*, vol. 47, no. 5, pp. 910–926, 2023, doi: 10.55730/1300-0527.3586.

[105] F. Umrath *et al.*, "Mechanical and Functional Improvement of β -TCP Scaffolds for Use in Bone Tissue Engineering," *J. Funct. Bioamaterials*, vol. 14, p. 427, 2023, doi: https://doi.org/10.3390/jfb14080427.

[106] H. Gao *et al.*, "Fabrication of cellulose nanofibers from waste brown algae and their potential application as milk thickeners," *Elsevier*, vol. 79, pp. 473–481, 2018, doi: 10.1016/j.foodhyd.2018.01.023.

[107] P. Kumari, G. Pathak, R. Gupta, D. Sharma, and A. Meena, "Cellulose nanofibers from lignocellulosic biomass of lemongrass using enzymatic hydrolysis : characterization and cytotoxicity," *J. Pharm. Sci.*, vol. 27, no. 2, pp. 683–693, 2019, doi: https://doi.org/10.1007/s40199-019-00303-1.

[108] H. Tibolla *et al.*, "Banana starch nanocomposite with cellulose nano fi bers isolated from banana peel by enzymatic treatment : In vitro cytotoxicity assessment," *Carbohydr. Polym.*, vol. 207, pp. 169–179, 2019, doi: 10.1016/j.carbpol.2018.11.079.

[109] A. Moriyama, "Potential issues specific to cytotoxicity tests of cellulose nanofibrils," *J. Appl. Toxicol.*, vol. 43, pp. 195–207, 2023, doi: 10.1002/jat.4390.

[110] D. Bellucci, R. Salvatori, A. Anesi, L. Chiarini, and V. Cannillo, "Materials Science & Engineering C SBF assays , direct and indirect cell culture tests to evaluate the biological performance of bioglasses and bioglass-based composites : Three paradigmatic cases," *Mater. Sci. Eng. C*, vol. 96, no. October 2018, pp. 757–764, 2019, doi: 10.1016/j.msec.2018.12.006.

[111] J. Kulhánková, D. Rohanová, D. Horkavcová, P. Bezdička, and A. R. Boccaccini, "The role of (HCO3)− ions in SBF on the interaction with bioactive glass-ceramic scaffold," *Mater. Today Chem.*, vol. 28, p. 101367, 2023, doi: 10.1016/j.mtchem.2022.101367.

[112] C. Tavares, T. Vieira, J. C. Silva, J. P. M. R. Borges, and M. C. Lança, "Bioactive Hydroxyapatite Aerogels with Piezoelectric Particles," *Biomimetics*, vol. 9, no. 3, pp. 1–17, 2024, doi: 10.3390/biomimetics9030143.

[113] H. Sehaqui, M. Salajková, Q. Zhou, and L. A. Berglund, "Mechanical performance tailoring of tough ultra-high porosity foams prepared from cellulose i nanofiber suspensions," *Soft Matter*, vol. 6, no. 8, pp. 1824–1832, 2010, doi: 10.1039/b927505c.

[114] T. Zhou, X. Cheng, Y. Pan, C. Li, and L. Gong, "Mechanical performance and thermal stability of polyvinyl alcohol–cellulose aerogels by freeze drying," *Cellulose*, vol. 26, no. 3, pp. 1747–1755, 2019, doi: 10.1007/s10570-018-2179-3.

[115] W. Guo, X. Wang, P. Zhang, J. Liu, L. Song, and Y. Hu, "Nano-fibrillated cellulose-hydroxyapatite based composite foams with excellent fire resistance," *Carbohydr. Polym.*, vol. 195, pp. 71–78, 2018, doi: 10.1016/j.carbpol.2018.04.063.

[116] C. Perier-Metz, G. N. Duda, and S. Checa, "Initial mechanical conditions within an

optimized bone scaffold do not ensure bone regeneration – an in silico analysis," *Biomech. Model. Mechanobiol.*, vol. 20, no. 5, pp. 1723–1731, 2021, doi: 10.1007/s10237-021-01472-2.

[117] Y. Lu, P. Tao, N. Zhang, and S. Nie, "Preparation and thermal stability evaluation of cellulose nanofibrils from bagasse pulp with differing hemicelluloses contents," *Carbohydr. Polym.*, vol. 245, p. 116463, 2020, doi: 10.1016/j.carbpol.2020.116463.

[118] R. Ceaser and A. F. A. Chimphango, "International Journal of Biological Macromolecules Comparative analysis of physical and functional properties of cellulose nano fi bers isolated from alkaline pre-treated wheat straw in optimized hydrochloric acid and enzymatic processes," *Int. J. Biol. Macromol.*, vol. 171, pp. 331–342, 2021, doi: 10.1016/j.ijbiomac.2021.01.018.

[119] M. Thommes *et al.*, "Physisorption of gases, with special reference to the evaluation of surface area and pore size distribution (IUPAC Technical Report)," *Pure Appl. Chem.*, vol. 87, no. 9–10, pp. 1051–1069, 2015, doi: 10.1515/pac-2014-1117.

A

APPENDIX – MATERIALS AND METHODS

A.1 Reagents and Equipments

Table A.1.1 - Specifications of the reagents used.

Reagent	Chemical formula	Entity	Purity
Oleic acid	$C_{18}H_{34}O_2$	Alfa Aesar, USA	99%
Methanol	CH_3OH	Valente e Ribeiro lda, Portugal	-
Sodium hydroxide	NaOH	Fisher Chemical, USA	≥98%
Calcium chloride	$CaCl_2$	Alfa Aesar, USA	≥93%
Sodium dihydrogen phosphate	$NaH_2PO_4•2H_2O$	VWR BDH-Chemicals, USA	100.2%
Calcium nitrate tetra-hydrate	$Ca(NO_3)_2•4H_2O$	Sigma-Aldrich, USA	99%
Potassium dihydrogen phosphate	KH_2PO_4	Panreac, Spain	99%
Ammonia	NH_3	VWR BDH-Chemicals, USA	25%
Cellulose nanofibers	$(C_6H_{10}O_5)_n$	PowerNano, Germany	-
Hydroxyapatite powder	$Ca_{10}(PO_4)_6(OH)_2$	Sigma-Aldrich, USA	≥ 90%;
SaOS-2 cell-line	-	ATCC, USA	-
Phosphate Buffered Saline	-	Thermo Fisher, USA	-
Resazurin	$C_{12}H_6NNaO_4$	Thermo Fisher, USA	-
Hydrochloric acid	HCl	Honeywell/Fluka, USA	≥ 37%

Table A.1.2 - Specifications of the equipments used.

Equipments	Entity
Autoclave 125 mL	Model Parr TM4748 Vessel, USA
Dry oven	Memmert, Germany
Refrigerated centrifuge	Thermo Fisher Scientific Multifuge X1R, USA
Electric furnace	Nabertherm, Germany
Ultrasonic processor	Hielscher UP50H, Germany
Freeze-dryer	Labconco, USA
Diffractometer	Aeris - Malvern Panalytical, Netherlands
Spectrometer	ATR-FTIR Perkin-Elmer - Spectrum Two, USA
Optical Emission Spectrometer	Horiba Jobin-Yvon - Ultima model, France
Microscopy	Hitachi TM 3030Plus model, Japan
Vacuum chamber	Quorum Q150T ES, UK
CO_2 Incubator	Sanyo, USA
Microplate reader	Biotek Synergy LX multi-mode, USA
Incubator	Optic Ivymen System - Comecta, Spain
Universal testing machine	Rheometric Scientific, Minimat Firmware Version 3.1, USA
Simultaneous thermal analyzer	Netzsch STA 449 F3, Germany
Gas porosimeter	Micromeritics ASAP 2010, USA
Binocular stereo microscope	Leica M80, Germany

A.2 Cytotoxicity tests

A.2.1 Segmentation for cell viability tests

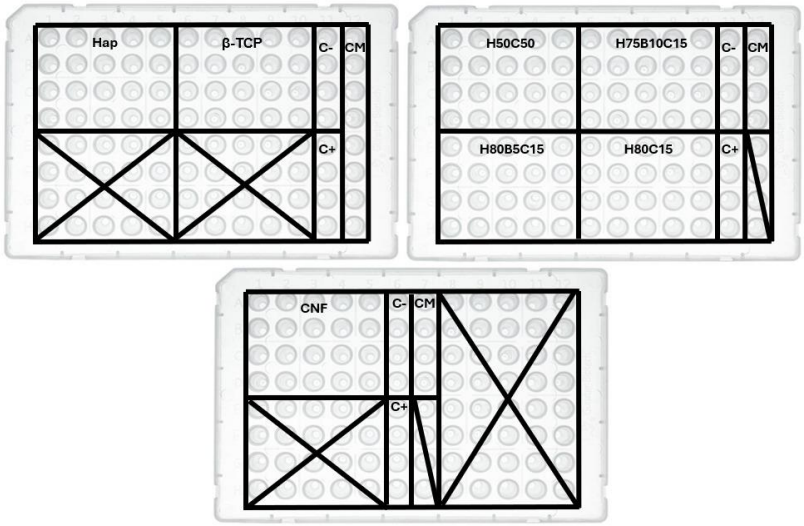

Figure A.2.1.1 - Segmentation used for cell viability tests. The left plate was used for the synthetized components of the cryogels, the right plate for the cryogels themselves and the below plate for the CNF

A.2.2 Data treatment of Cytotoxicity tests

Given the resulting absorbance values obtained, the relative cell population, P, was calculated according to the following equation A.2.1:

$$P(\%) = \frac{A_{ct}}{A_{cc}} \times 100 \qquad \textbf{(A.2.1)}$$

where A_{ct} represents the difference between the average absorbance measured at 571 nm and 601 nm for both the sample medium and the medium control, and A_{cc} represents the difference between the average absorbance measured at 571 nm and 601 nm for both the negative control and the medium control.

The standard deviation of absorbance in the sample medium, ΔA_{ct}, and in the control groups, ΔA_{cc}, was calculated using the following equation A.2.2:

$$\Delta = \sqrt{\sigma^2 + \sigma_{CM}^2} \qquad \textbf{(A.2.2)}$$

where σ is the experimental standard deviation of the replicate set and σ_{CM} is the experimental standard deviation of the medium control.

The uncertainty associated with the relative viability was calculated using uncertainty propagation, according to the following equation A.2.3:

$$\Delta = P \times \sqrt{\left(\frac{\Delta A_{ct}}{A_{ct}}\right)^2 + \left(\frac{\Delta A_{cc}}{A_{cc}}\right)^2} \qquad \textbf{(A.2.3)}$$

where P is the relative cell population, ΔA_{ct} is the uncertainty associated with the absorbance of the medium from the cells in the test condition (A_{ct}), and ΔA_{cc} is the uncertainty associated with the absorbance of the medium from the control cells (A_{cc}).

The result obtained allows us to characterize the extract's cytotoxicity according to Table A.2.2.1 below:

Table A.2.2.1 - Standard Values for Relative Cell Viability according to ISO 10993-5.

Cytotoxicity	Relative Cell Viability (%)
Non-cytotoxic	≥ 90
Slightly cytotoxic	[80, 89]
Moderately cytotoxic	[50, 79]
Severely cytotoxic	< 50

A.3 Protocol for Simulated Body Fluid solution

Table A.3.1 - Order, purity and quantity of reagents for preparing 1 L of SBF.

Order	Reagent	Chemical Formula	Entity	Purity (%)	Quantity
1	Sodium chloride	NaCl	Honeywell/Fluka, USA	99.5	7.996 g
2	Sodium hydrogen carbonate	$NaHCO_3$	Sigma-Aldrich, USA	99.5	0.350 g
3	Potassium chloride	KCl	Scharlau, Spain	99.5	0.224 g
4	Di-potassium hydrogen phosphate trihydrate	$K_2HPO_4 \cdot 3H_2O$	Sigma-Aldrich, USA	≥99.0	0.228 g
5	Magnesium chloride hexahydrate	$MgCl_2 \cdot 6H_2O$	Roth, Germany	≥99.0	0.305 g
6	Hydrochloric acid	HCl (1.0M)	-	-	40 mL
7	Calcium chloride dihydrate	$CaCl_2 \cdot 2H_2O$	Alfa Aesar, USA	≥93.0	0.0278 g
8	Sodium sulphate	Na_2SO_4	Fluka, USA	≥99.0	0.007 g
9	Tris-hydroxymethyl aminomethane	$(CH_2OH)_3CNH_2$	Alfa Aesar, USA	99.0	6.057 g

B

APPENDIX - RESULTS AND DISCUSSION

B.1 Histograms of Hap NW, CNF Diameter and β-TCP Particle Size

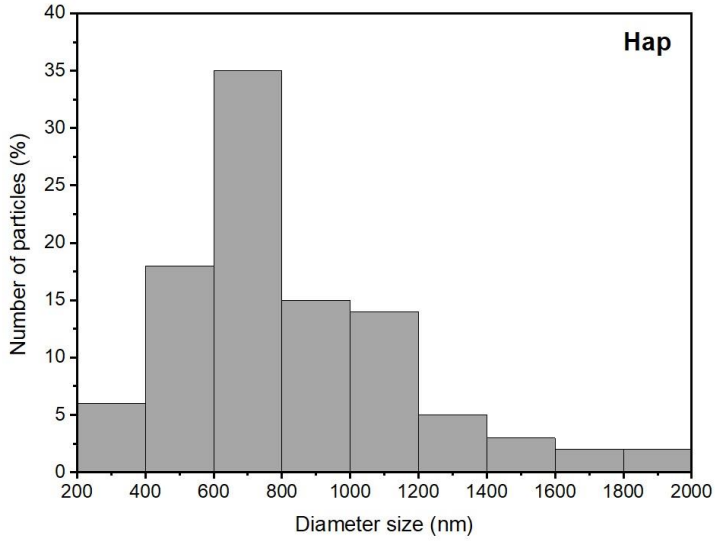

Figure B.1.1 - Histogram of the diameter distribution of Hap NW

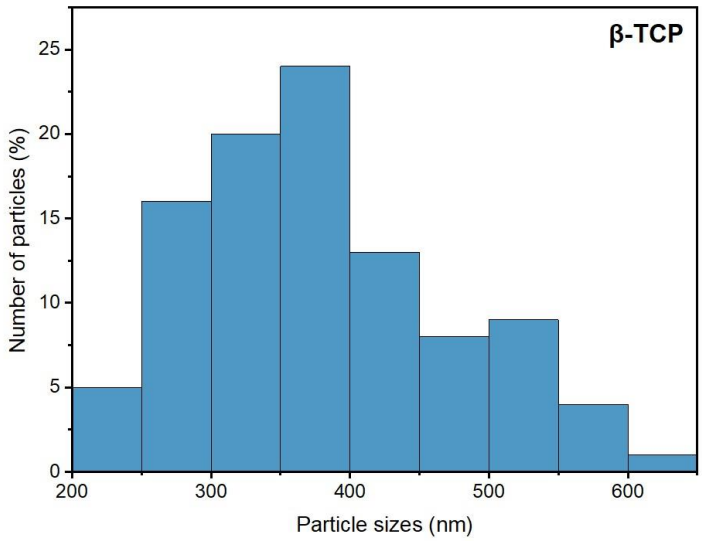

Figure B.1.2 - Histogram of the particle size distribution of β-TCP nanoparticles

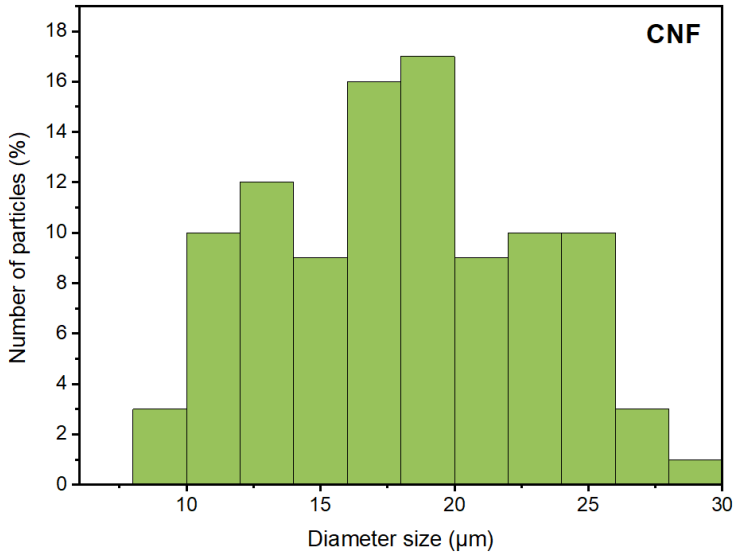

Figure B.1.3 - Histogram of the diameter distribution of CNF

B.2 Compositional results from ICP-OES

Table B.2.1 - Ca/P ratio of 5 samples of Hap NW synthetized obtained with ICP-OES.

	Ca(%)	P(%)	Ca/P
1st sample	58.80	27.90	2.11
2nd sample	43.10	21.90	1.97
3rd sample	56.46	28.81	1.96
4th sample	39.44	20.13	1.96
5th sample	58.49	32.50	1.80
Mean			1.96
Standard Deviation			0.10

Table B.2.2 - Ca/P ratio of 1 sample of β-TCP synthetized obtained with ICP-OES

	Ca(%)	P(%)	Ca/P
1st sample	59.90	32.00	1.87

B.3 Morphological Characterization

B.3.1 SEM and naked eye images of cryogels

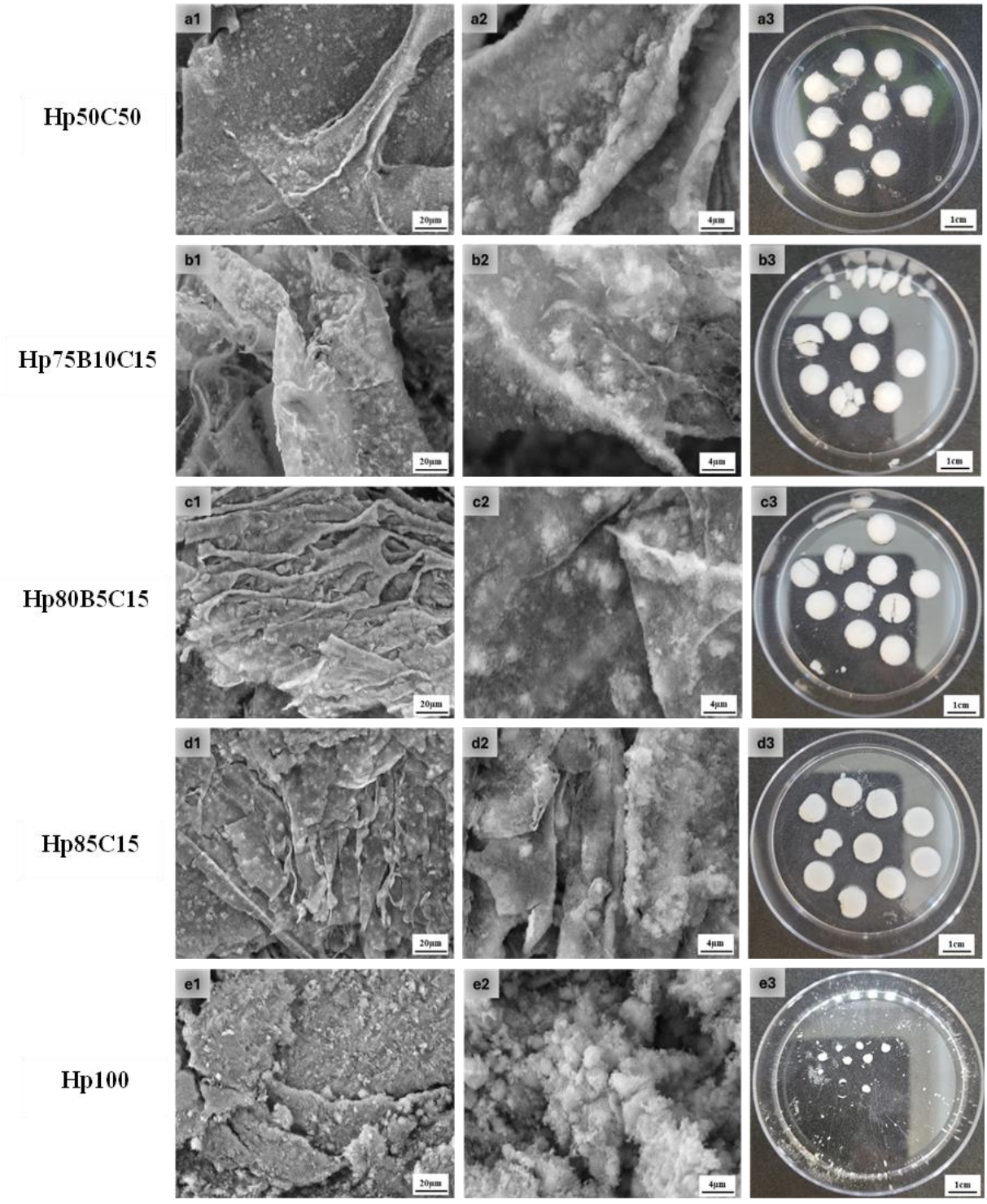

Figure B.3.1.1 - SEM analysis of cryogels with commercial Hap. Hp50C50: a1) x1K, a2) x5K and a3) naked eye morphology; Hp75B10C15: b1) x1K, b2) x5K and b3) naked eye morphology; Hp80B5C15: c1) x1K, c2) x5K and c3) naked eye morphology; Hp85C15: d1) x1K, d2) x5K and d3) naked eye morphology; H100: e1) x1K, e2) x5K and e3) naked eye morphology.

B.3.2 Quantification and mapping EDS analysis of dry cryogels

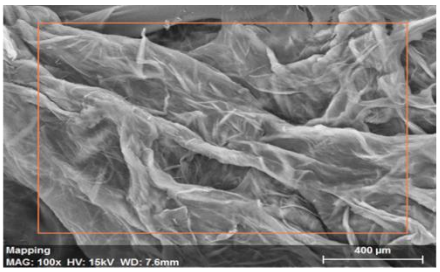

Spectrum: Point

Element	AN	Series	Net	unn. C [wt.%]	norm. C [wt.%]	Atom. C [at.%]
Oxygen	8	K-series	2069	38.33	45.52	47.00
Carbon	6	K-series	1460	25.21	29.93	41.18
Calcium	20	K-series	3257	12.48	14.82	6.11
Phosphorus	15	K-series	2698	5.82	6.91	3.68
Sodium	11	K-series	614	2.38	2.82	2.03
			Total:	84.21	100.00	100.00

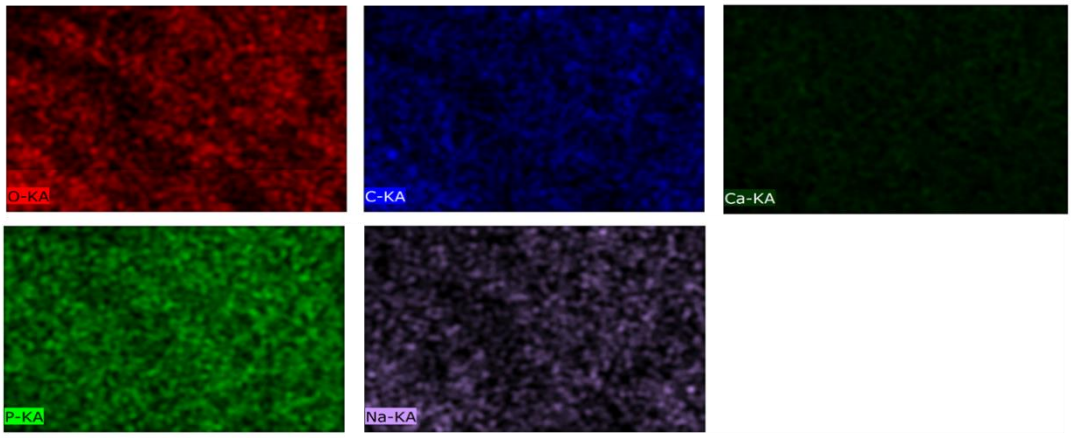

Figure B.3.2.1 - Quantification and mapping EDS analysis of the H50C50 cryogel (control sample not immersed in SBF)

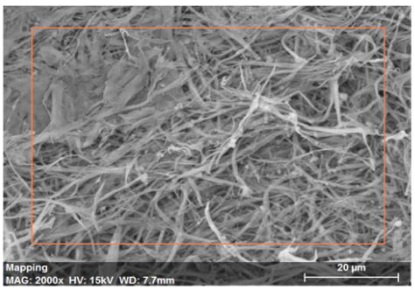

Spectrum: Point

Element	AN	Series	Net	unn. C [wt.%]	norm. C [wt.%]	Atom. C [at.%]
Oxygen	8	K-series	3012	38.53	42.88	51.82
Carbon	6	K-series	1120	14.57	16.22	26.11
Calcium	20	K-series	10998	24.10	26.82	12.94
Phosphorus	15	K-series	8297	11.21	12.48	7.79
Sodium	11	K-series	613	1.43	1.60	1.34
			Total:	89.84	100.00	100.00

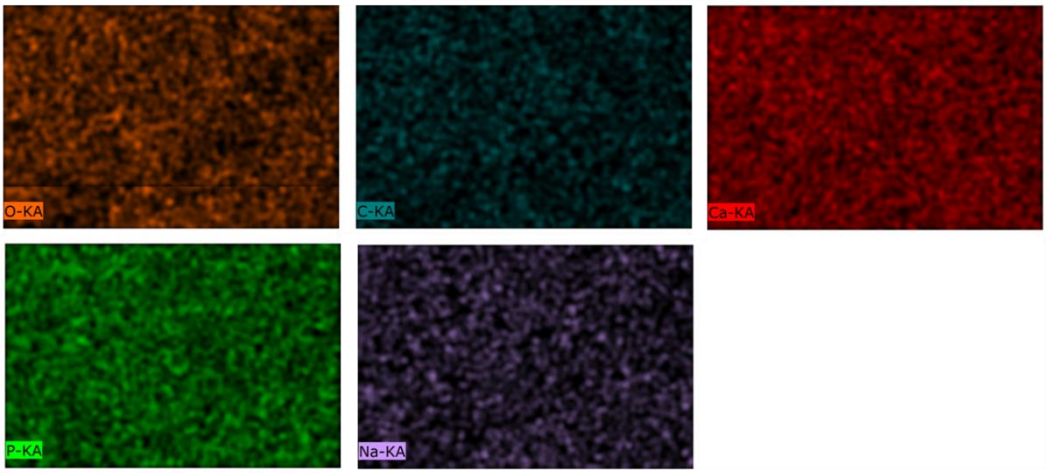

Figure B.3.2.2 - Quantification and mapping EDS analysis of the H75B10C15 cryogel (control sample not immersed in SBF)

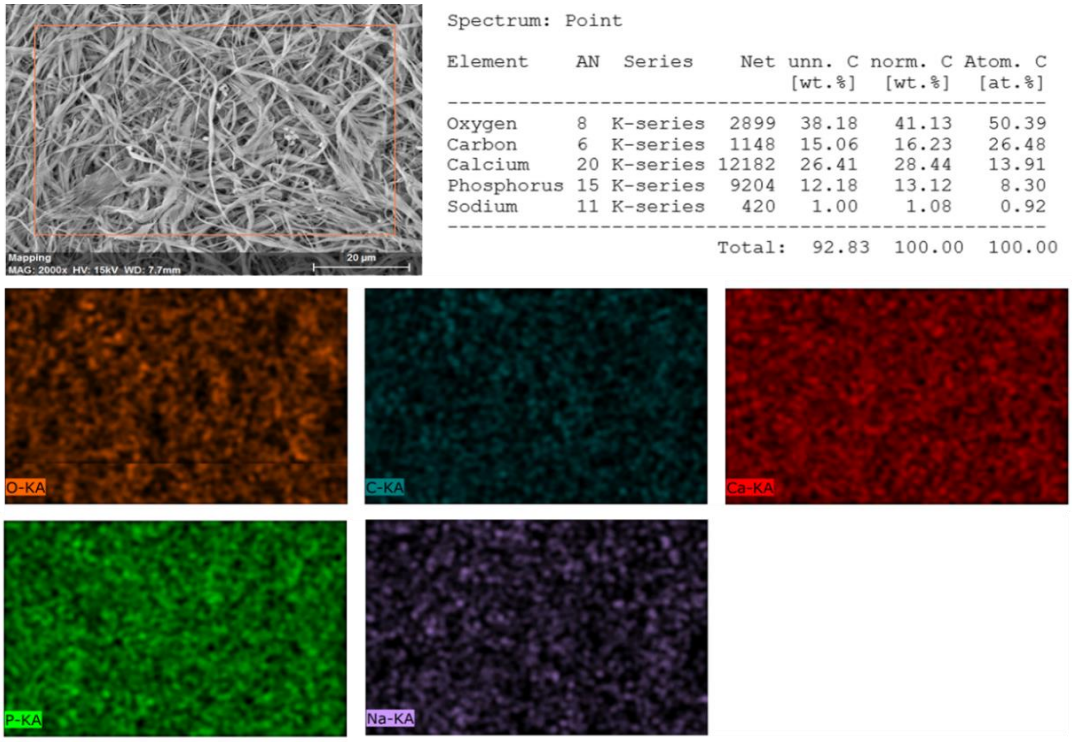

Figure B.3.2.4 - Quantification and mapping EDS analysis of the H80B5C15 cryogel (control sample not immersed in SBF)

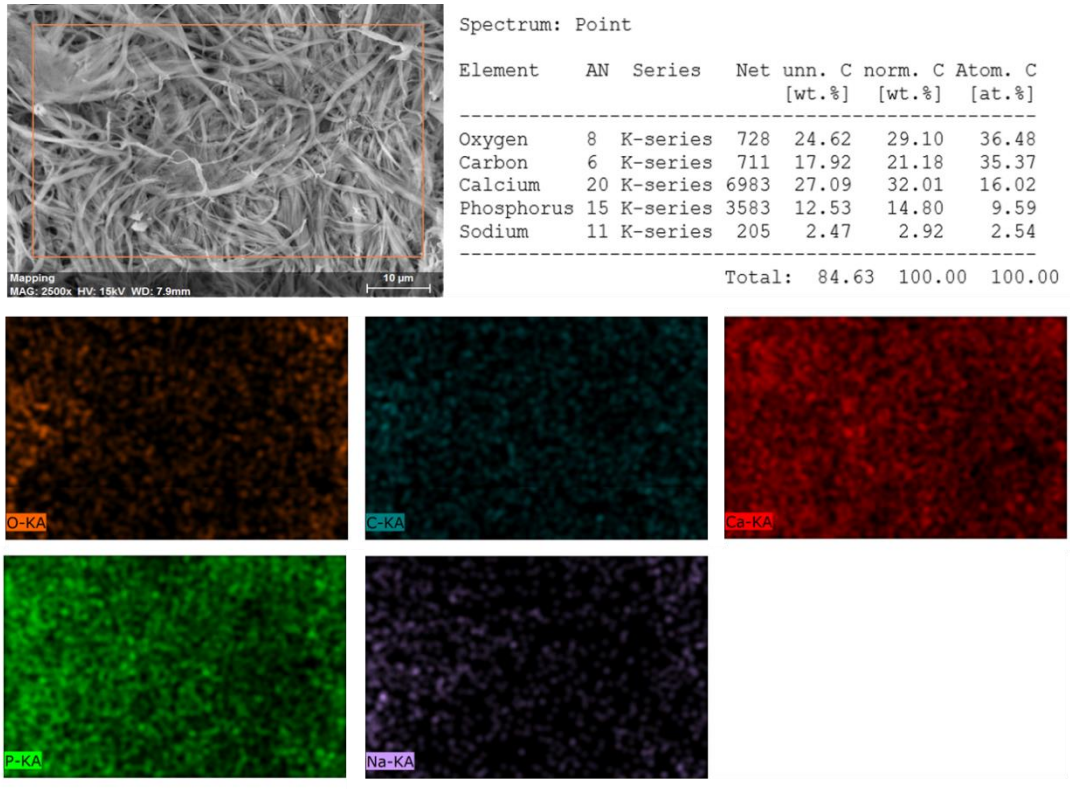

Figure B.3.2.3 - Quantification and mapping EDS analysis of the H85C15 cryogel, (control sample not immersed in SBF)

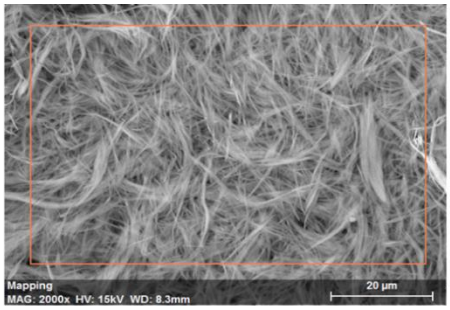

Spectrum: Point

Element	AN	Series	Net unn. C [wt.%]	norm. C [wt.%]	Atom. C [at.%]
Oxygen	8	K-series	2418	41.36	39.02	52.73
Calcium	20	K-series	15140	37.40	35.27	19.03
Carbon	6	K-series	594	9.89	9.33	16.80
Phosphorus	15	K-series	10211	17.37	16.38	11.44
		Total:	106.02	100.00	100.00	

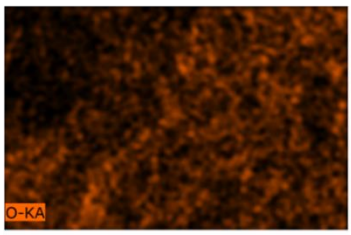

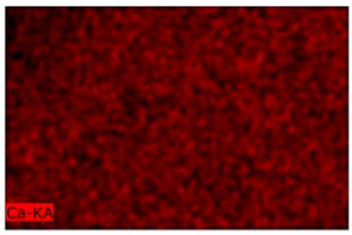

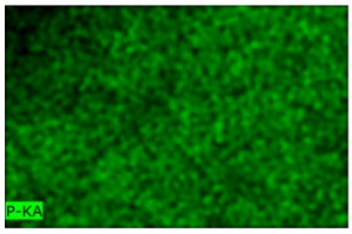

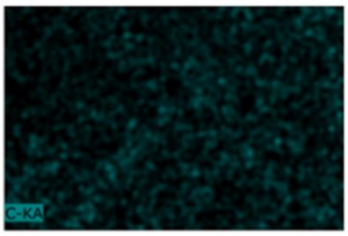

Figure B.3.2.5 - Quantification and mapping EDS analysis of the H100 cryogel (control sample not immersed in SBF)

B.4 Cytotoxicity results

Table B.4.1 - Relative cell population and relative uncertainty of cell population of Hap NW, β-TCP, CNF for each concentration (mg/mL) and for negative (C-) and positive (C+) control groups.

	Relative cell population (%)			Relative uncertainty of cell population (%)		
Dilution	Hap NW	β-TCP	CNF	Hap NW	β-TCP	CNF
20 mg/mL	93.8	101.4	40.0	5.1	8.1	24.4
10 mg/mL	105.9	107.0	67.6	5.3	8.0	5.7
5 mg/mL	107.7	103.3	77.7	5.8	7.8	6.3
2.5 mg/mL	107.1	106.8	91.8	7.1	9.3	3.0
1.25 mg/mL	106.5	109.2	95.1	7.1	8.9	4.5
C-	100.0			6.6		3.6
C+	3.9		2.0	0.7		1.4

Table B.4.2 - Relative cell population and relative uncertainty of cryogels H50C50, H75B10C15, H80B5C15 and H85C15 for each concentration (mg/mL) and for negative (C-) and positive (C+) control groups.

	Relative cell population (%)				**Relative uncertainty of cell population (%)**			
Dilution	**H50C50**	**H75B10C15**	**H80B5C15**	**H85C15**	**H50C50**	**H75B10C15**	**H80B5C15**	**H85C15**
5 mg/mL	96.9	98.4	98.6	95.3	2.1	2.0	1.8	3.4
2.5 mg/mL	99.0	99.7	102.7	97.5	5.5	3.1	2.8	4.3
1.25 mg/mL	101.8	99.6	103,5	99.2	2.8	3.1	5.0	4.8
0.625 mg/mL	99.1	100.1	100.1	98.3	1.8	1.6	2.8	4.5
0.3125 mg/mL	97.3	98.0	98.7	101.8	2.4	7.8	3.3	2.5
C-	100.0				1.1			
C+	3.2				2.1			

B.5 Bioactivity assays – SBF immersion

B.5.1 SEM results

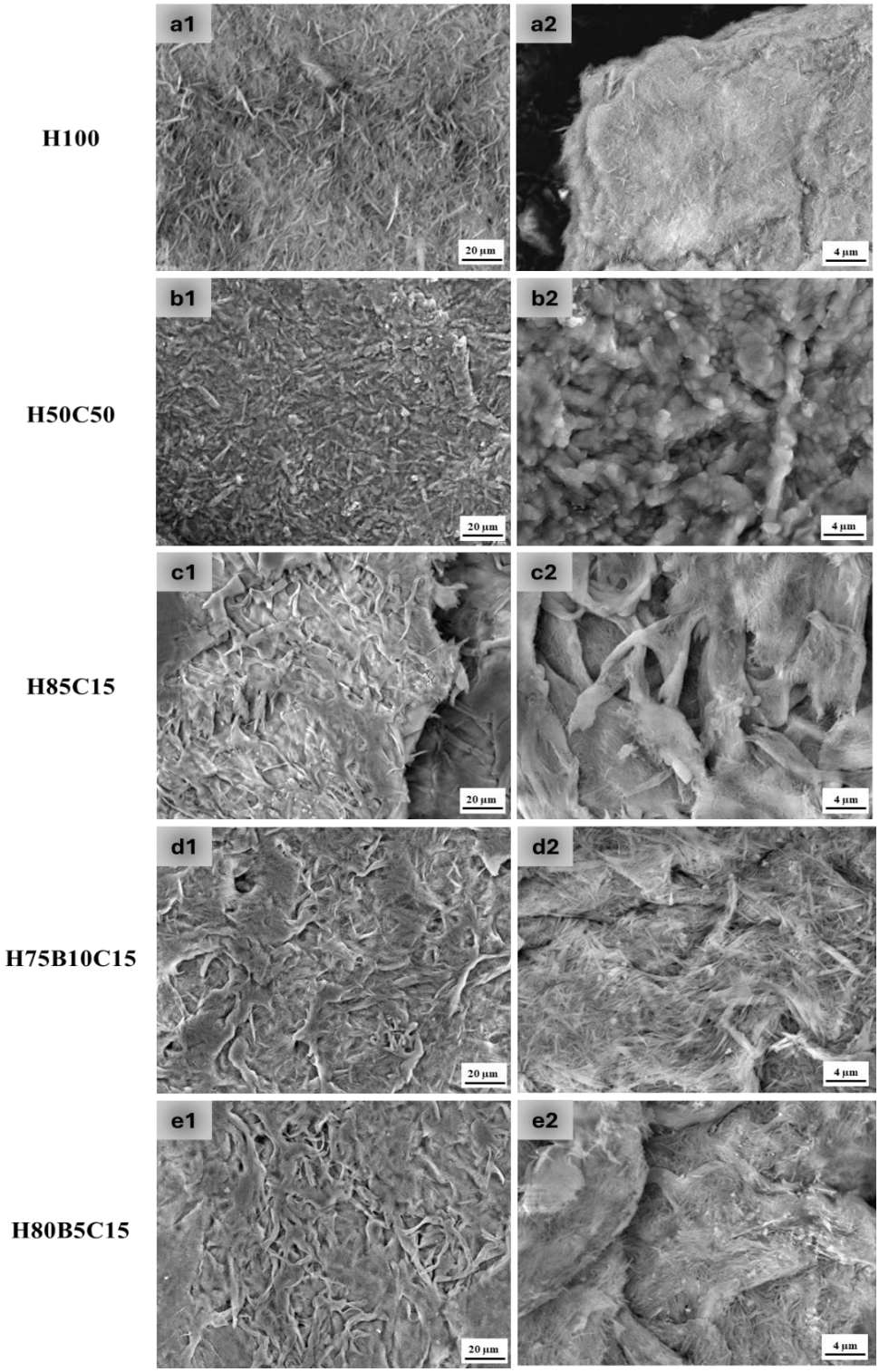

Figure B.5.1.1 - SEM analysis of cryogels after 1 day in SBF – H100: a1) x1K, a2) x5K; H50C50: b1) x1K, b2) x5K; H85C15: c1) x1K, c2) x5K; H75B10C15: d1) x1K, d2) x5K and H80B5C15: e1) x1K, e2) x5K. H –Hap, B - β-TCP and C - CNF.

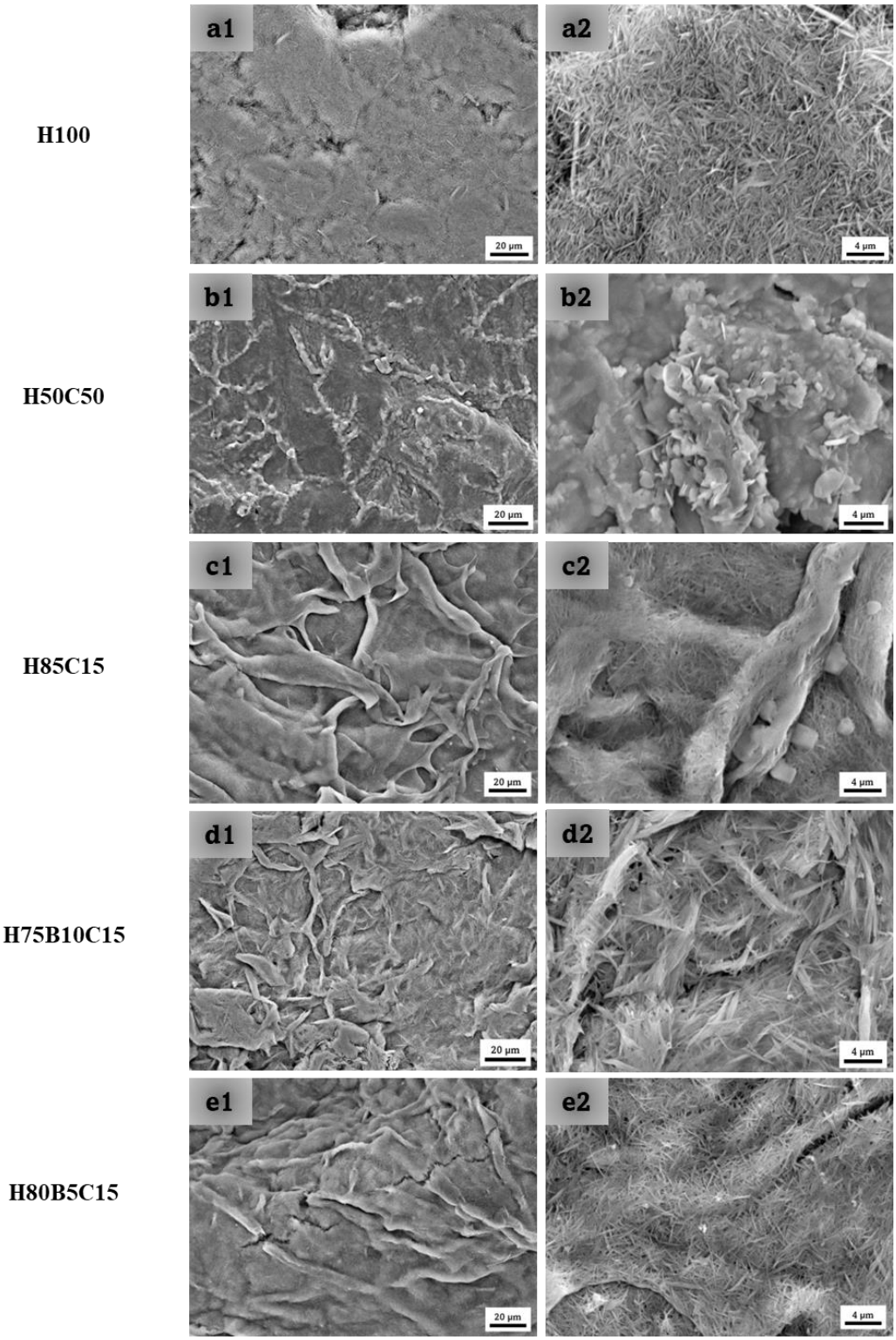

Figure B.5.1.2 - SEM analysis of cryogels after 3 days in SBF – H100: a1) x1K, a2) x5K; H50C50: b1) x1K, b2) x5K; H85C15: c1) x1K, c2) x5K; H75B10C15: d1) x1K, d2) x5K and H80B5C15: e1) x1K, e2) x5K. H –Hap, B - β-TCP and C - CNF.

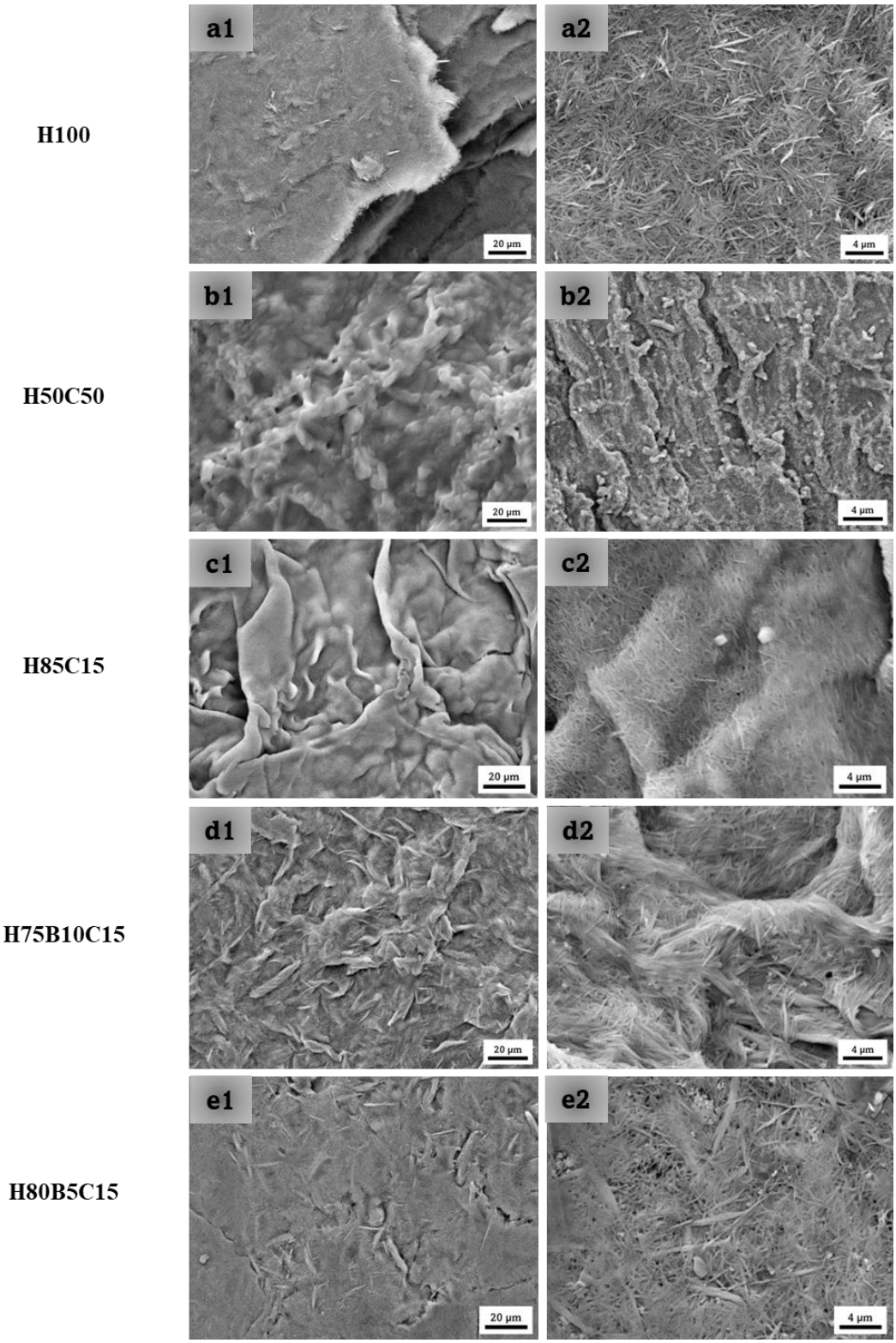

Figure B.5.1.3 - SEM analysis of cryogels after 7 days in SBF – H100: a1) x1K, a2) x5K; H50C50: b1) x1K, b2) x5K; H85C15: c1) x1K, c2) x5K; H75B10C15: d1) x1K, d2) x5K and H80B5C15: e1) x1K, e2) x5K. H –Hap, B - β-TCP and C - CNF.

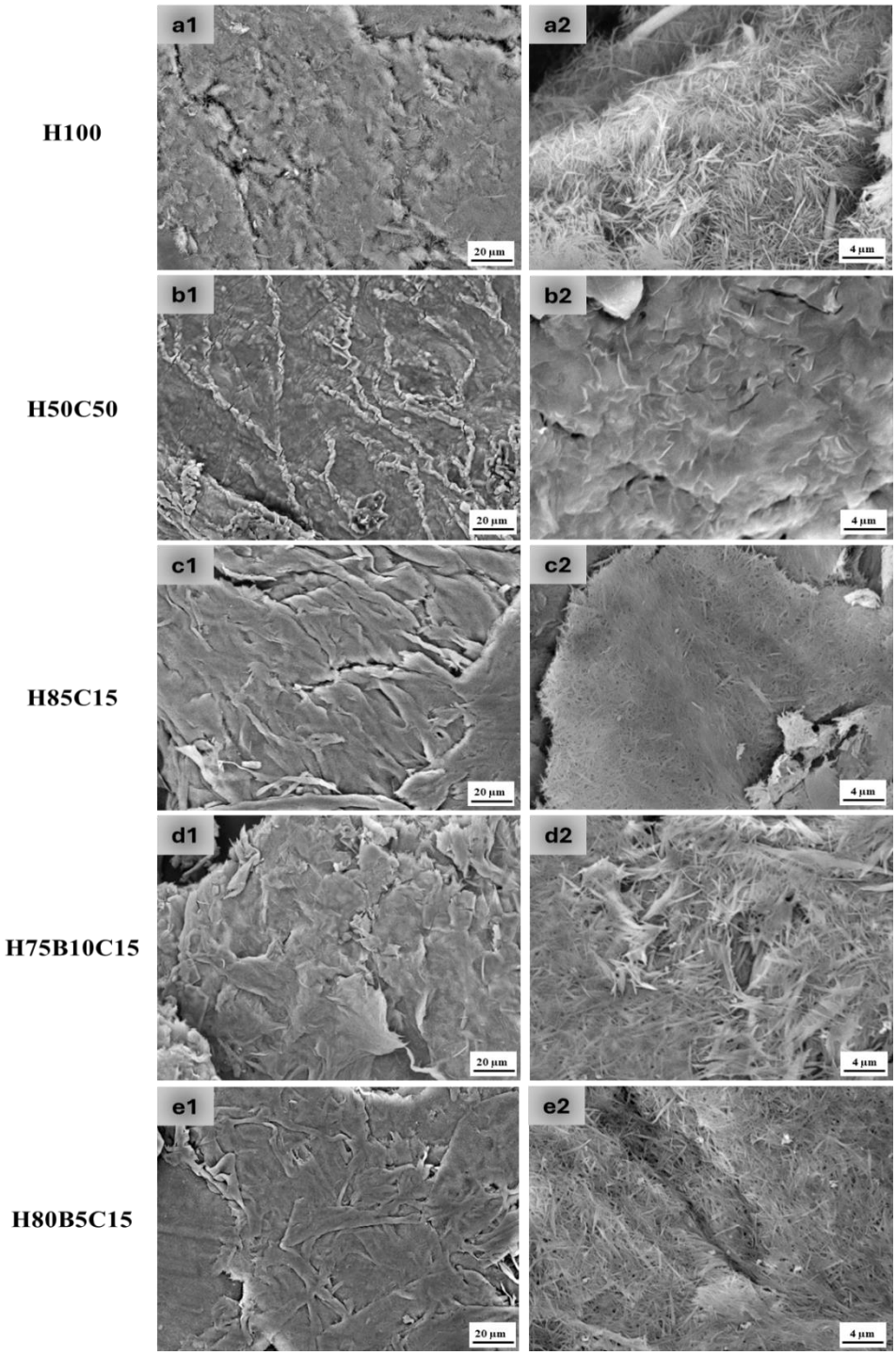

Figure B.5.1.4 - SEM analysis of cryogels after 14 days in SBF – H100: a1) x1K, a2) x5K; H50C50: b1) x1K, b2) x5K; H85C15: c1) x1K, c2) x5K; H75B10C15: d1) x1K, d2) x5K and H80B5C15: e1) x1K, e2) x5K. H–Hap, B- β-TCP and C - CNF.

B.5.2 Quantification and mapping EDS analysis

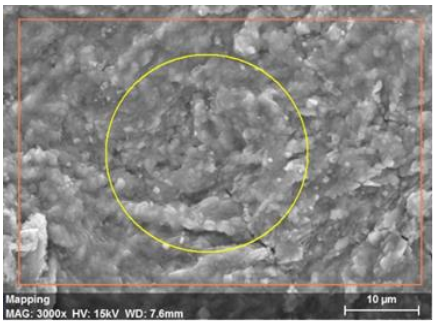

Spectrum: Point

Element	AN	Series	Net	unn. C [wt.%]	norm. C [wt.%]	Atom. C [at.%]
Carbon	6	K-series	380	16.89	20.60	36.54
Sodium	11	K-series	6429	19.30	23.54	21.82
Chlorine	17	K-series	11234	23.47	28.62	17.20
Oxygen	8	K-series	474	9.41	11.48	15.29
Calcium	20	K-series	2965	8.85	10.79	5.74
Phosphorus	15	K-series	2312	4.08	4.97	3.42
		Total:		82.00	100.00	100.00

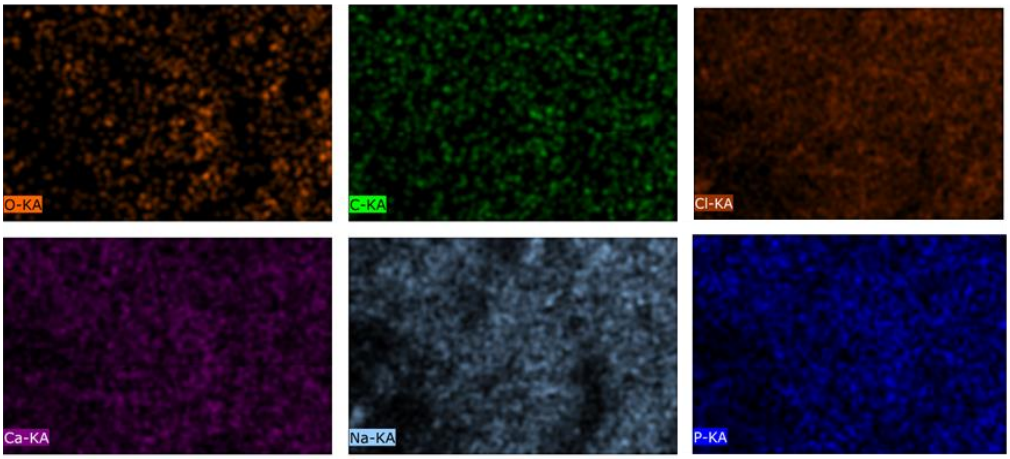

Figure B.5.2.1 - Quantification and mapping EDS analysis of the H50C50 cryogel after 1 day in SBF

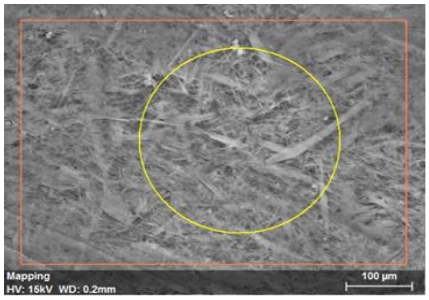

Spectrum: Point

Element	AN	Series	Net	unn. C [wt.%]	norm. C [wt.%]	Atom. C [at.%]
Oxygen	8	K-series	3485	39.66	41.91	50.52
Carbon	6	K-series	1297	16.09	17.00	27.30
Calcium	20	K-series	12543	24.25	25.62	12.33
Phosphorus	15	K-series	9663	11.37	12.02	7.48
Sodium	11	K-series	654	1.56	1.65	1.38
Chlorine	17	K-series	1225	1.70	1.80	0.98
		Total:		94.63	100.00	100.00

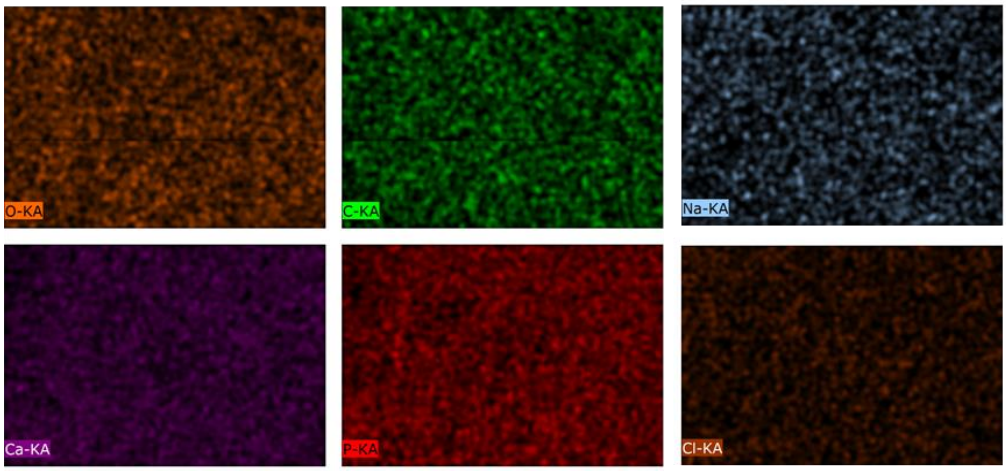

Figure B.5.2.2 - Quantification and mapping EDS analysis of the H75B10C15 cryogel after 1 day in SBF

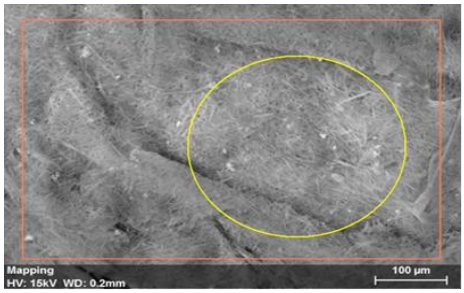

Spectrum: Point

Element	AN	Series	Net	unn. C [wt.%]	norm. C [wt.%]	Atom. C [at.%]
Oxygen	8	K-series	2609	43.45	43.74	55.60
Carbon	6	K-series	606	11.28	11.36	19.23
Calcium	20	K-series	10266	29.28	29.48	14.96
Phosphorus	15	K-series	8023	13.63	13.72	9.01
Sodium	11	K-series	269	0.73	0.74	0.65
Chlorine	17	K-series	471	0.96	0.97	0.55
			Total:	99.32	100.00	100.00

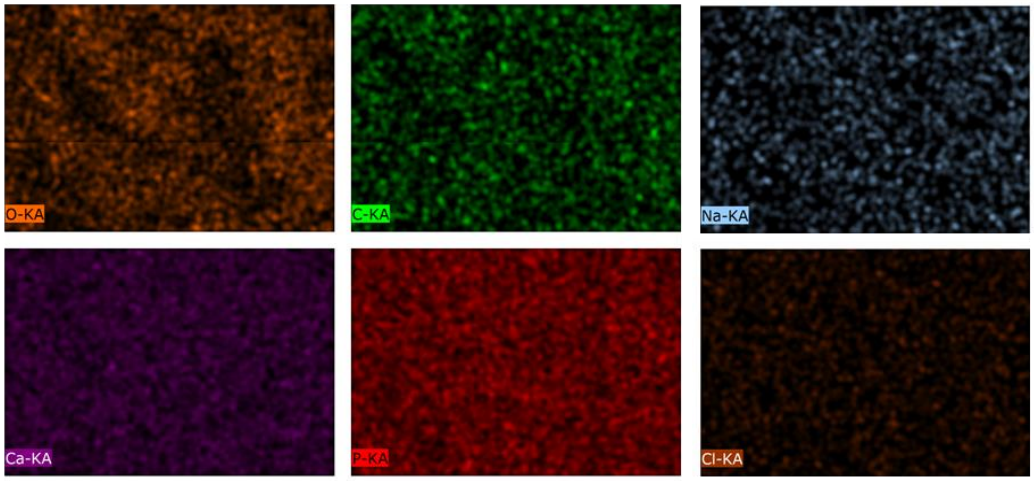

Figure B.5.2.3 - Quantification and mapping EDS analysis of the H80B5C15 cryogel after 1 day in SBF

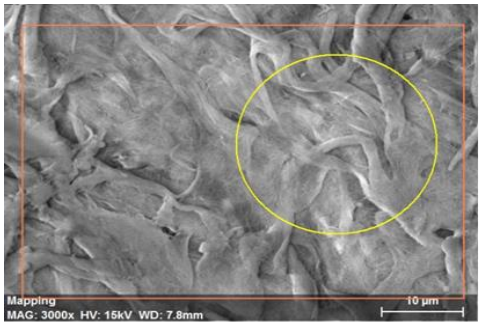

Spectrum: Point

Element	AN	Series	Net	unn. C [wt.%]	norm. C [wt.%]	Atom. C [at.%]
Oxygen	8	K-series	2063	40.16	41.38	52.49
Carbon	6	K-series	487	12.02	12.39	20.93
Calcium	20	K-series	7733	26.21	27.01	13.68
Phosphorus	15	K-series	6184	12.15	12.52	8.20
Sodium	11	K-series	680	2.69	2.77	2.45
Chlorine	17	K-series	1644	3.81	3.93	2.25
			Total:	97.04	100.00	100.00

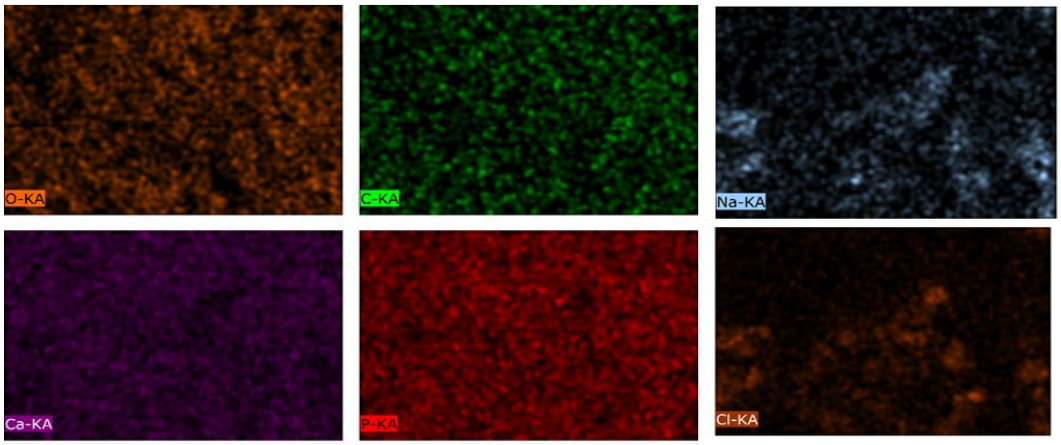

Figure B.5.2.4 - Quantification and mapping EDS analysis of the H85C15 cryogel after 1 day in SBF

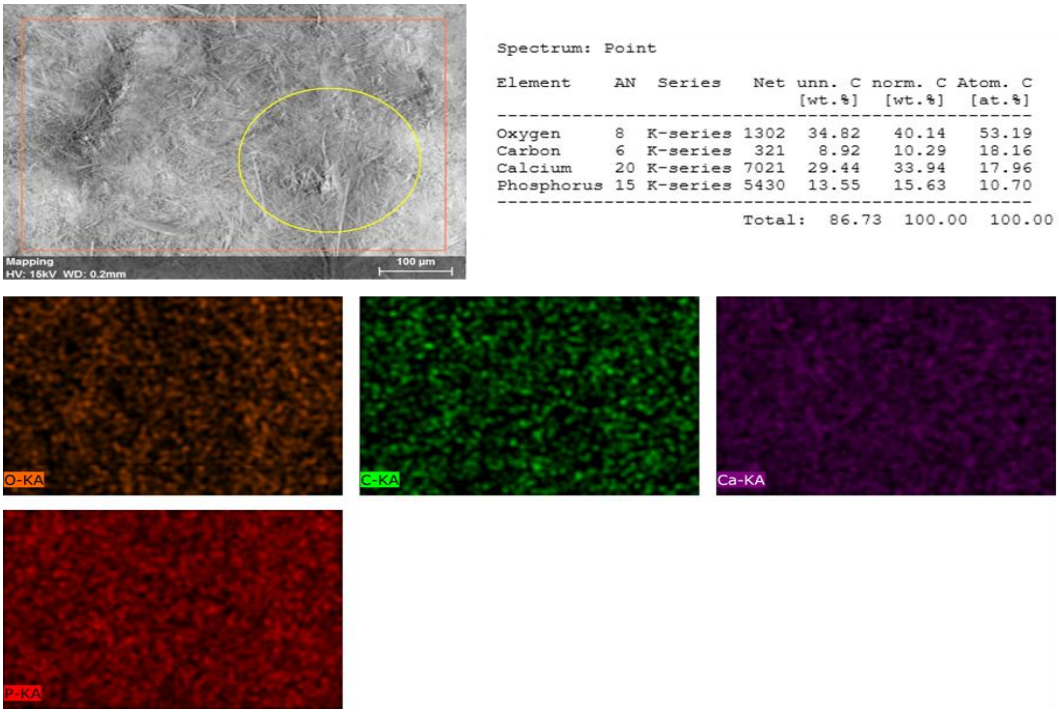

Spectrum: Point

Element	AN	Series	Net	unn. C [wt.%]	norm. C [wt.%]	Atom. C [at.%]
Oxygen	8	K-series	1302	34.82	40.14	53.19
Carbon	6	K-series	321	8.92	10.29	18.16
Calcium	20	K-series	7021	29.44	33.94	17.96
Phosphorus	15	K-series	5430	13.55	15.63	10.70
Total:				86.73	100.00	100.00

Figure B.5.2.5 - Quantification and mapping EDS analysis of the H100 cryogel after 1 day in SBF

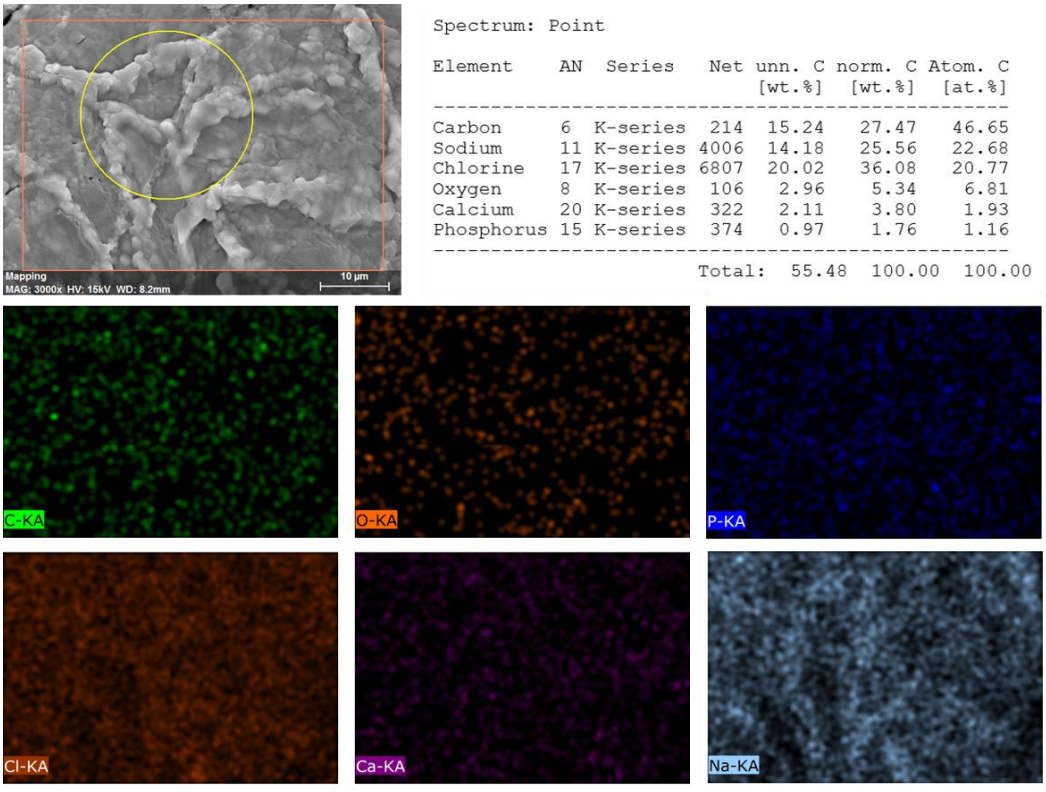

Spectrum: Point

Element	AN	Series	Net	unn. C [wt.%]	norm. C [wt.%]	Atom. C [at.%]
Carbon	6	K-series	214	15.24	27.47	46.65
Sodium	11	K-series	4006	14.18	25.56	22.68
Chlorine	17	K-series	6807	20.02	36.08	20.77
Oxygen	8	K-series	106	2.96	5.34	6.81
Calcium	20	K-series	322	2.11	3.80	1.93
Phosphorus	15	K-series	374	0.97	1.76	1.16
Total:				55.48	100.00	100.00

Figure B.5.2.6 - Quantification and mapping EDS analysis of the H50C50 cryogel after 3 days in SBF

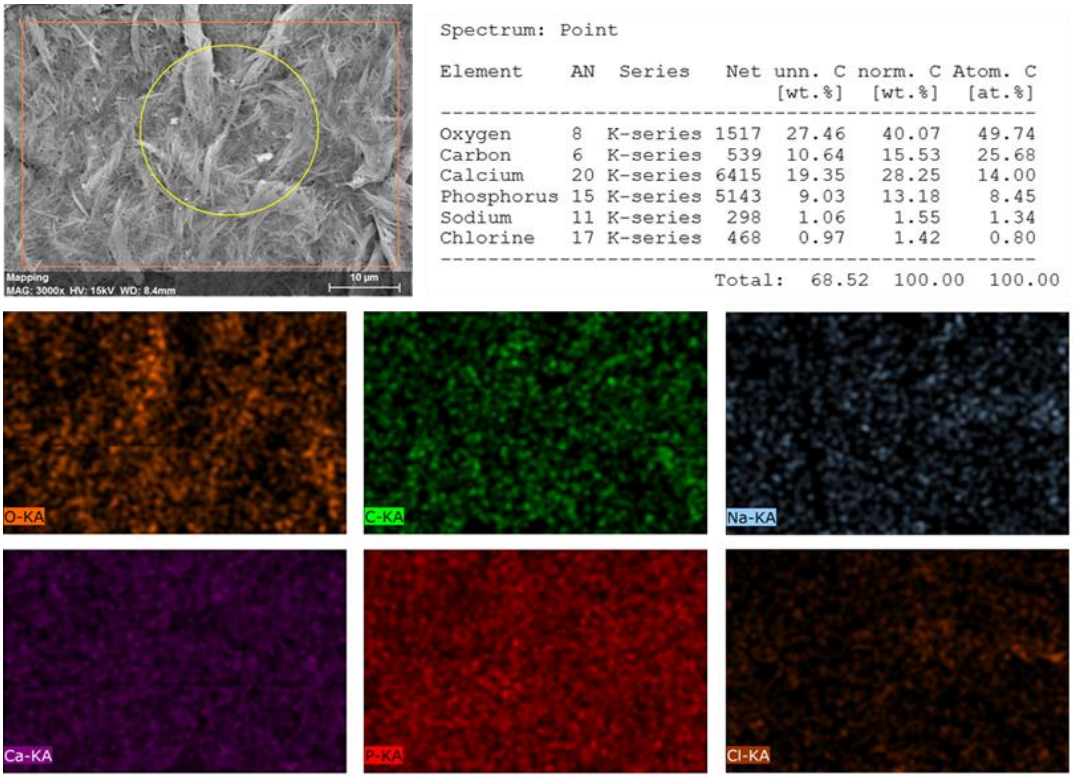

Spectrum: Point

Element	AN	Series	Net unn. C [wt.%]	norm. C [wt.%]	Atom. C [at.%]
Oxygen	8	K-series	1517	27.46	40.07	49.74
Carbon	6	K-series	539	10.64	15.53	25.68
Calcium	20	K-series	6415	19.35	28.25	14.00
Phosphorus	15	K-series	5143	9.03	13.18	8.45
Sodium	11	K-series	298	1.06	1.55	1.34
Chlorine	17	K-series	468	0.97	1.42	0.80
			Total:	68.52	100.00	100.00

Figure B.5.2.7 - Quantification and mapping EDS analysis of the H75B10C15 cryogel after 3 days in SBF

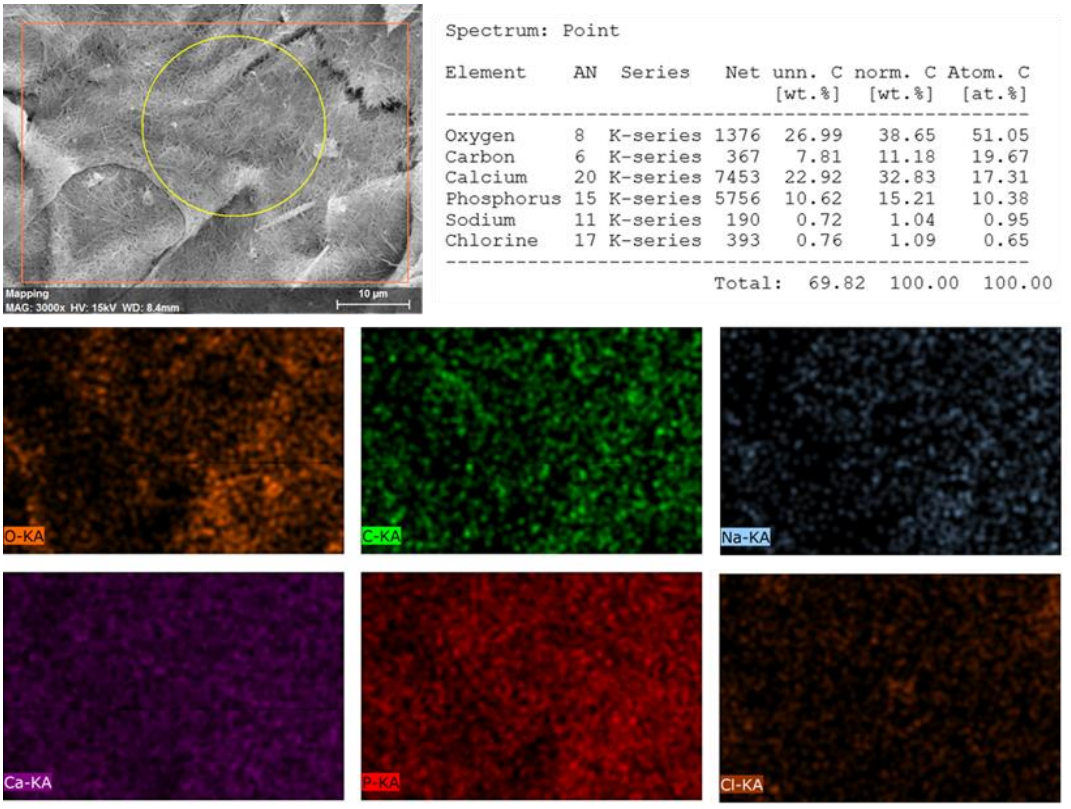

Spectrum: Point

Element	AN	Series	Net unn. C [wt.%]	norm. C [wt.%]	Atom. C [at.%]
Oxygen	8	K-series	1376	26.99	38.65	51.05
Carbon	6	K-series	367	7.81	11.18	19.67
Calcium	20	K-series	7453	22.92	32.83	17.31
Phosphorus	15	K-series	5756	10.62	15.21	10.38
Sodium	11	K-series	190	0.72	1.04	0.95
Chlorine	17	K-series	393	0.76	1.09	0.65
			Total:	69.82	100.00	100.00

Figure B.5.2.8 - Quantification and mapping EDS analysis of the H80B5C15 cryogel after 3 days in SBF

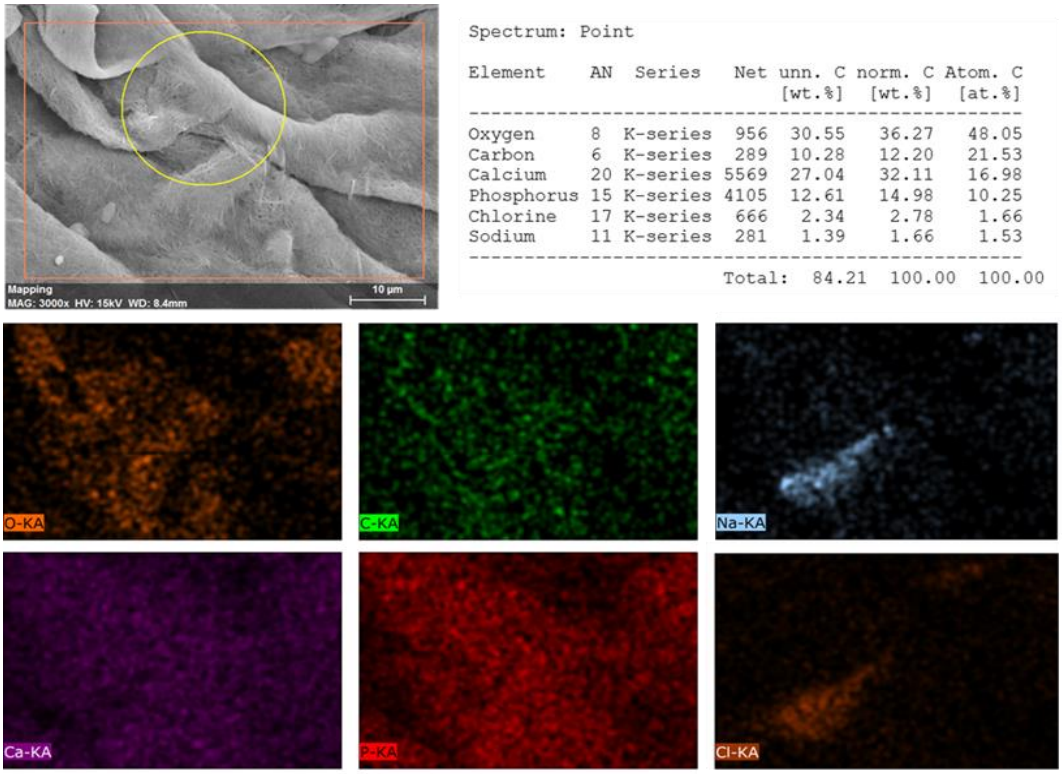

Spectrum: Point

Element	AN	Series	Net	unn. C [wt.%]	norm. C [wt.%]	Atom. C [at.%]
Oxygen	8	K-series	956	30.55	36.27	48.05
Carbon	6	K-series	289	10.28	12.20	21.53
Calcium	20	K-series	5569	27.04	32.11	16.98
Phosphorus	15	K-series	4105	12.61	14.98	10.25
Chlorine	17	K-series	666	2.34	2.78	1.66
Sodium	11	K-series	281	1.39	1.66	1.53
			Total:	84.21	100.00	100.00

Figure B.5.2.9 - Quantification and mapping EDS analysis of the H85C15 cryogel after 3 days in SBF

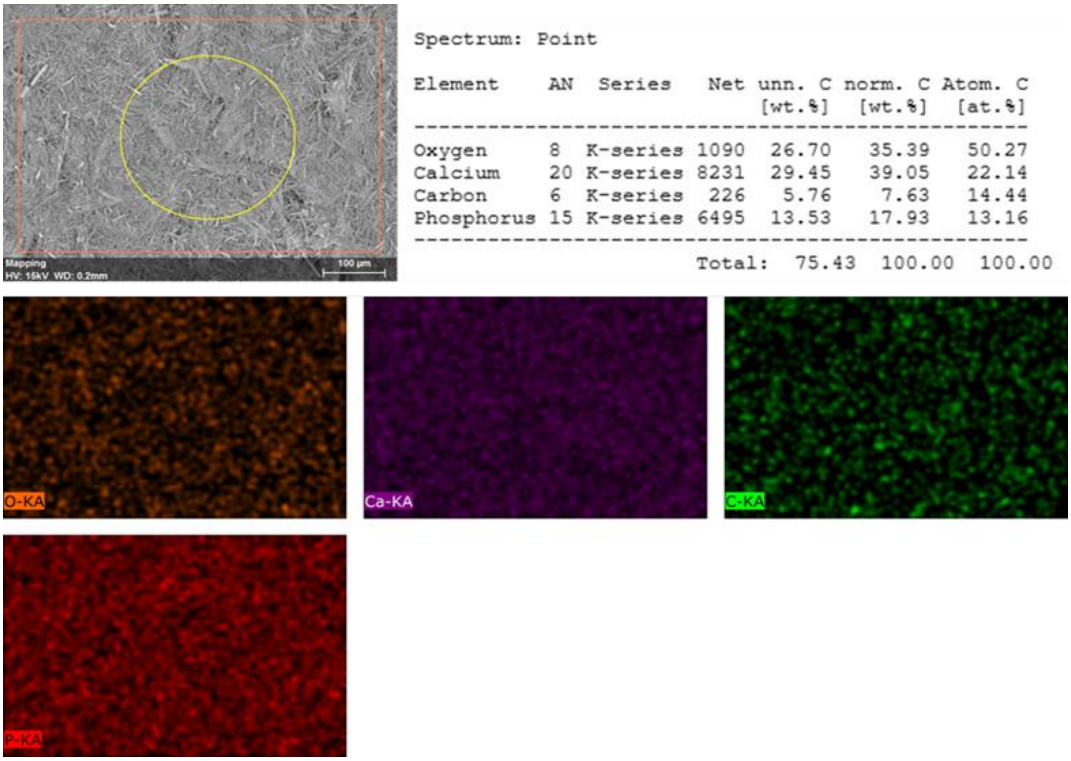

Spectrum: Point

Element	AN	Series	Net	unn. C [wt.%]	norm. C [wt.%]	Atom. C [at.%]
Oxygen	8	K-series	1090	26.70	35.39	50.27
Calcium	20	K-series	8231	29.45	39.05	22.14
Carbon	6	K-series	226	5.76	7.63	14.44
Phosphorus	15	K-series	6495	13.53	17.93	13.16
			Total:	75.43	100.00	100.00

Figure B.5.2.10 - Quantification and mapping EDS analysis of the H100 cryogel after 3 days in SBF

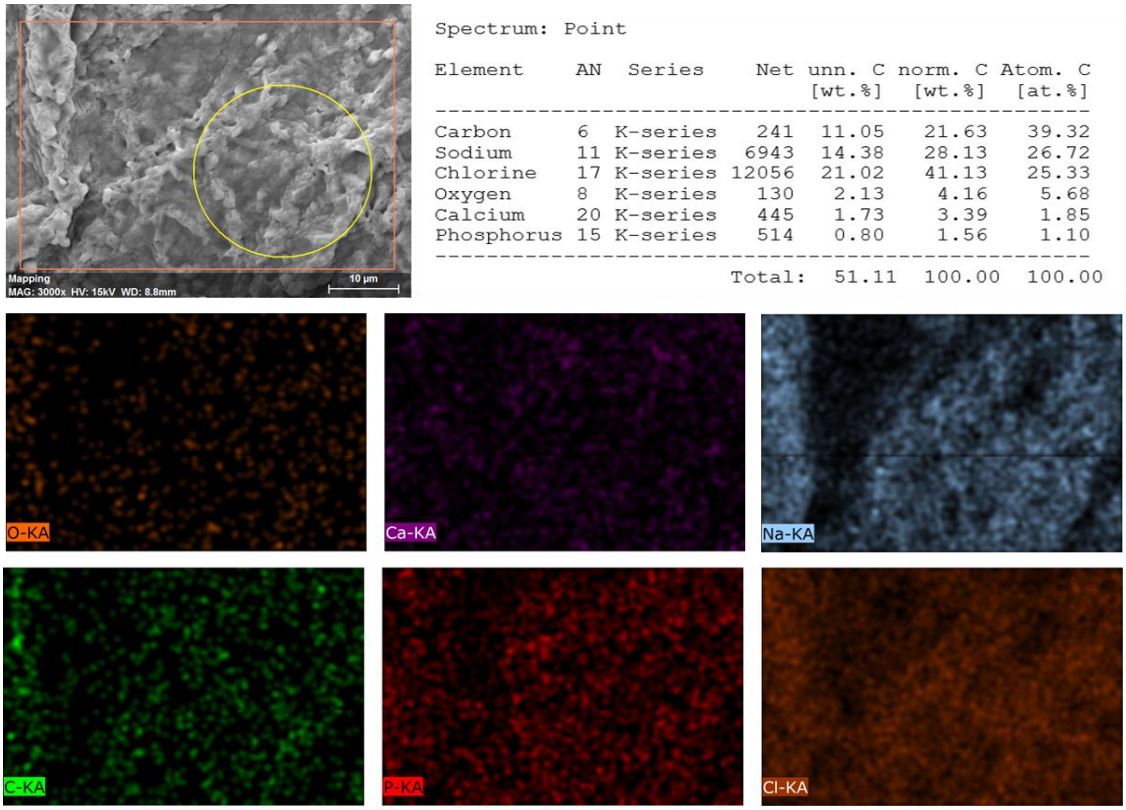

Spectrum: Point

Element	AN	Series	Net	unn. C [wt.%]	norm. C [wt.%]	Atom. C [at.%]
Carbon	6	K-series	241	11.05	21.63	39.32
Sodium	11	K-series	6943	14.38	28.13	26.72
Chlorine	17	K-series	12056	21.02	41.13	25.33
Oxygen	8	K-series	130	2.13	4.16	5.68
Calcium	20	K-series	445	1.73	3.39	1.85
Phosphorus	15	K-series	514	0.80	1.56	1.10
Total:				51.11	100.00	100.00

Figure B.5.2.11 - Quantification and mapping EDS analysis of the H50C50 cryogel after 7 days in SBF

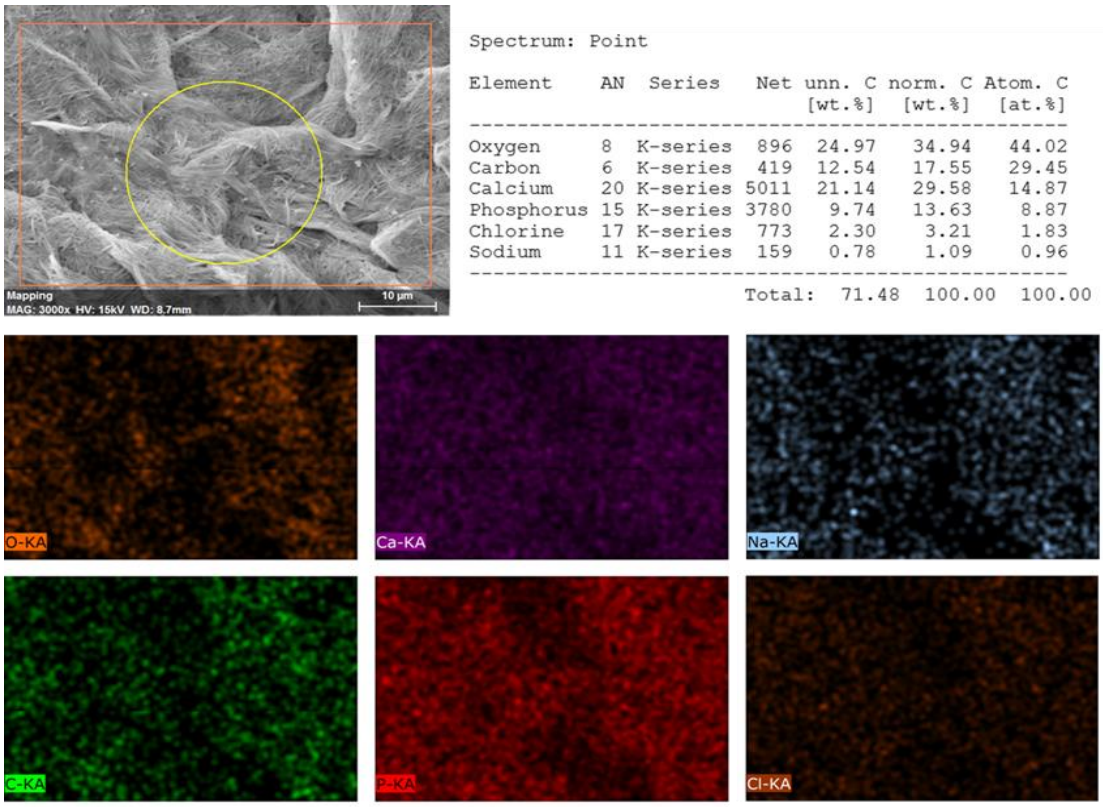

Spectrum: Point

Element	AN	Series	Net	unn. C [wt.%]	norm. C [wt.%]	Atom. C [at.%]
Oxygen	8	K-series	896	24.97	34.94	44.02
Carbon	6	K-series	419	12.54	17.55	29.45
Calcium	20	K-series	5011	21.14	29.58	14.87
Phosphorus	15	K-series	3780	9.74	13.63	8.87
Chlorine	17	K-series	773	2.30	3.21	1.83
Sodium	11	K-series	159	0.78	1.09	0.96
Total:				71.48	100.00	100.00

Figure B.5.2.12 - Quantification and mapping EDS analysis of the H75B10C15 cryogel after 7 days in SBF

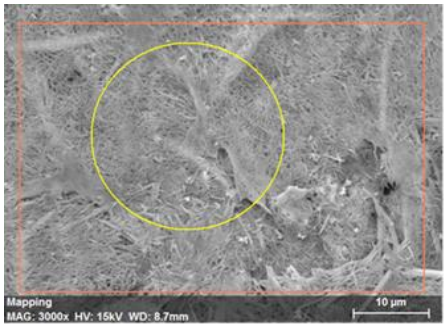

Spectrum: Point

Element	AN	Series	Net	unn. C [wt.%]	norm. C [wt.%]	Atom. C [at.%]
Oxygen	8	K-series	1200	26.12	37.18	46.65
Carbon	6	K-series	448	11.52	16.40	27.42
Calcium	20	K-series	5523	19.79	28.16	14.11
Phosphorus	15	K-series	4597	9.14	13.02	8.44
Chlorine	17	K-series	1145	2.71	3.86	2.19
Sodium	11	K-series	242	0.97	1.38	1.21
			Total:	70.26	100.00	100.00

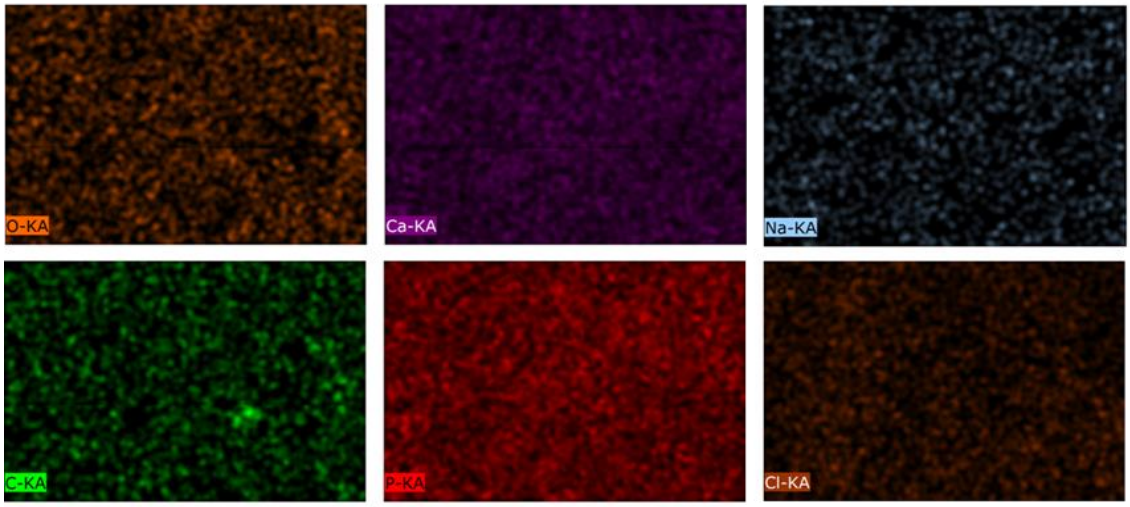

Figure B.5.2.13 - Quantification and mapping EDS analysis of the H80B5C15 cryogel after 7 days in SBF

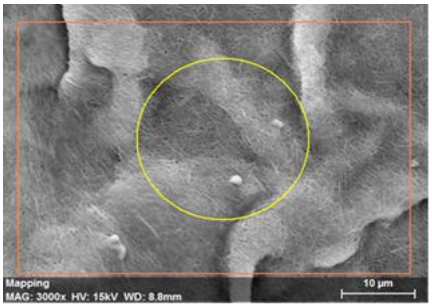

Spectrum: Point

Element	AN	Series	Net	unn. C [wt.%]	norm. C [wt.%]	Atom. C [at.%]
Oxygen	8	K-series	834	22.41	33.57	42.55
Carbon	6	K-series	372	11.65	17.46	29.47
Calcium	20	K-series	4591	19.45	29.14	14.74
Phosphorus	15	K-series	3699	9.04	13.55	8.87
Chlorine	17	K-series	1057	2.55	3.81	2.18
Sodium	11	K-series	322	1.65	2.47	2.18
			Total:	66.75	100.00	100.00

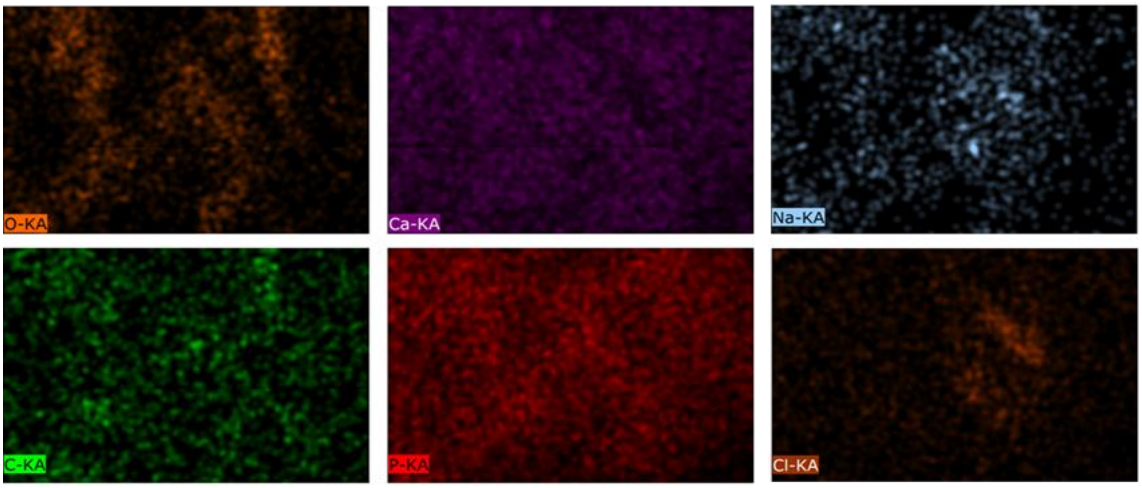

Figure B.5.2.14 - Quantification and mapping EDS analysis of the H85C15 cryogel after 7 days in SBF

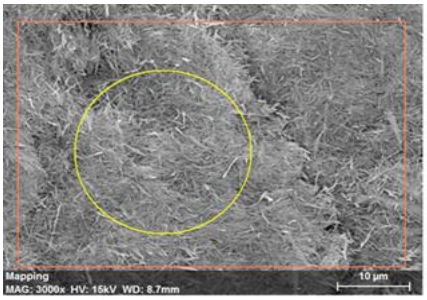

Spectrum: Point

Element	AN	Series	Net unn. C [wt.%]	norm. C [wt.%]	Atom. C [at.%]
Oxygen	8	K-series	1036	22.78	37.33	50.32
Calcium	20	K-series	6368	21.72	35.60	19.15
Carbon	6	K-series	282	6.49	10.63	19.09
Phosphorus	15	K-series	5220	10.03	16.44	11.44
Total:				61.02	100.00	100.00

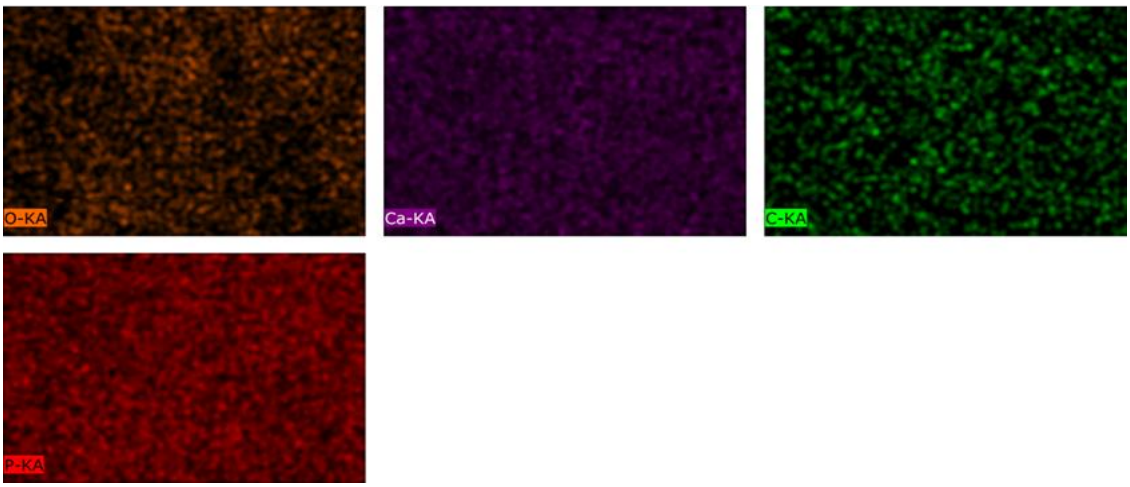

Figure B.5.2.15 - Quantification and mapping EDS analysis of the H100 cryogel after 7 days in SBF

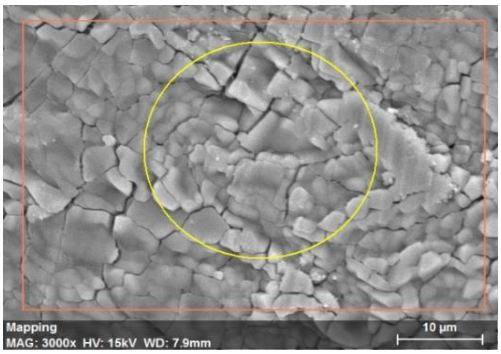

Spectrum: Point

Element	AN	Series	Net unn. C [wt.%]	norm. C [wt.%]	Atom. C [at.%]
Carbon	6	K-series	254	10.98	19.01	34.79
Sodium	11	K-series	8028	17.43	30.16	28.84
Chlorine	17	K-series	12018	20.10	34.80	21.57
Oxygen	8	K-series	246	3.88	6.71	9.22
Calcium	20	K-series	1007	3.67	6.35	3.48
Phosphorus	15	K-series	1041	1.71	2.97	2.10
Total:				57.77	100.00	100.00

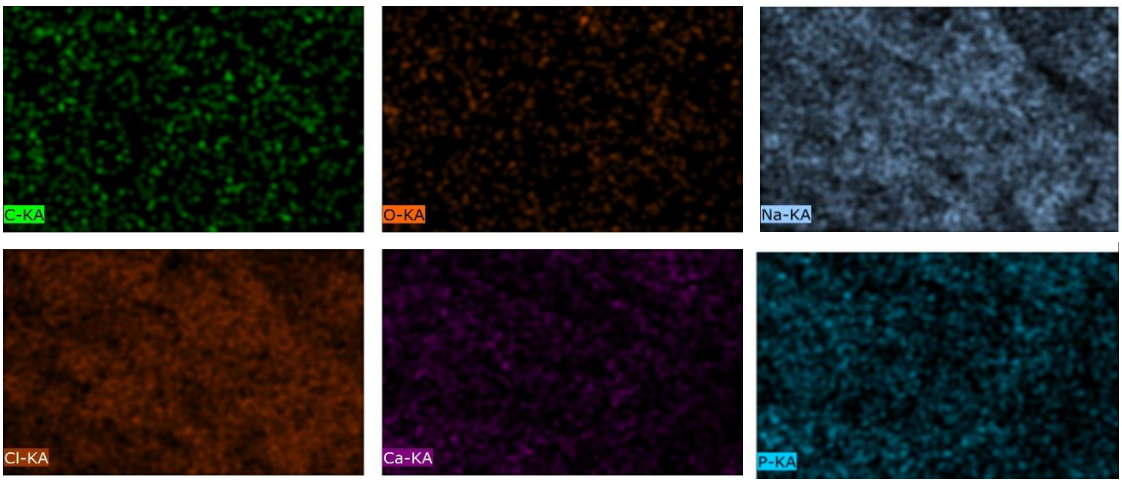

Figure B.5.2.16 - Quantification and mapping EDS analysis of the H50C50 cryogel after 14 days in SBF

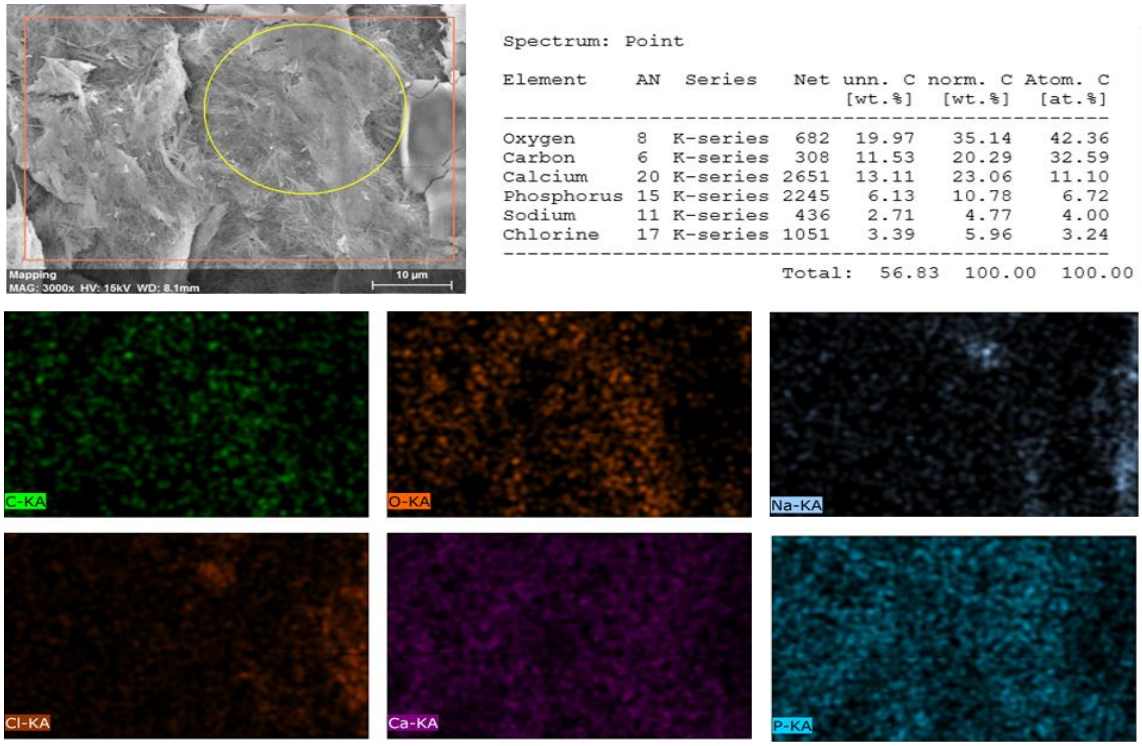

Spectrum: Point

Element	AN	Series	Net	unn. C [wt.%]	norm. C [wt.%]	Atom. C [at.%]
Oxygen	8	K-series	682	19.97	35.14	42.36
Carbon	6	K-series	308	11.53	20.29	32.59
Calcium	20	K-series	2651	13.11	23.06	11.10
Phosphorus	15	K-series	2245	6.13	10.78	6.72
Sodium	11	K-series	436	2.71	4.77	4.00
Chlorine	17	K-series	1051	3.39	5.96	3.24
Total:				56.83	100.00	100.00

Figure B.5.2.17 - Quantification and mapping EDS analysis of the H75B10C15 cryogel after 14 days in SBF

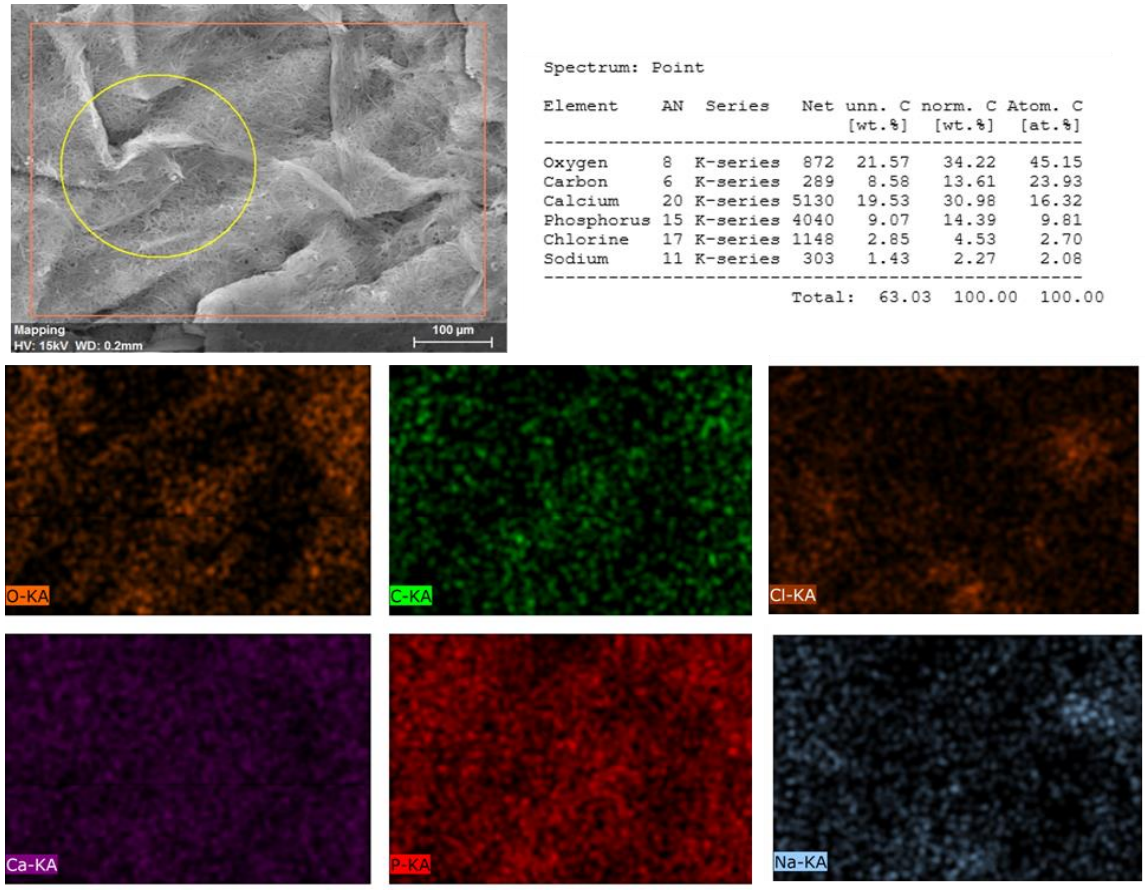

Spectrum: Point

Element	AN	Series	Net	unn. C [wt.%]	norm. C [wt.%]	Atom. C [at.%]
Oxygen	8	K-series	872	21.57	34.22	45.15
Carbon	6	K-series	289	8.58	13.61	23.93
Calcium	20	K-series	5130	19.53	30.98	16.32
Phosphorus	15	K-series	4040	9.07	14.39	9.81
Chlorine	17	K-series	1148	2.85	4.53	2.70
Sodium	11	K-series	303	1.43	2.27	2.08
Total:				63.03	100.00	100.00

Figure B.5.2.18 - Quantification and mapping EDS analysis of the H80B5C15 cryogel after 14 days in SBF

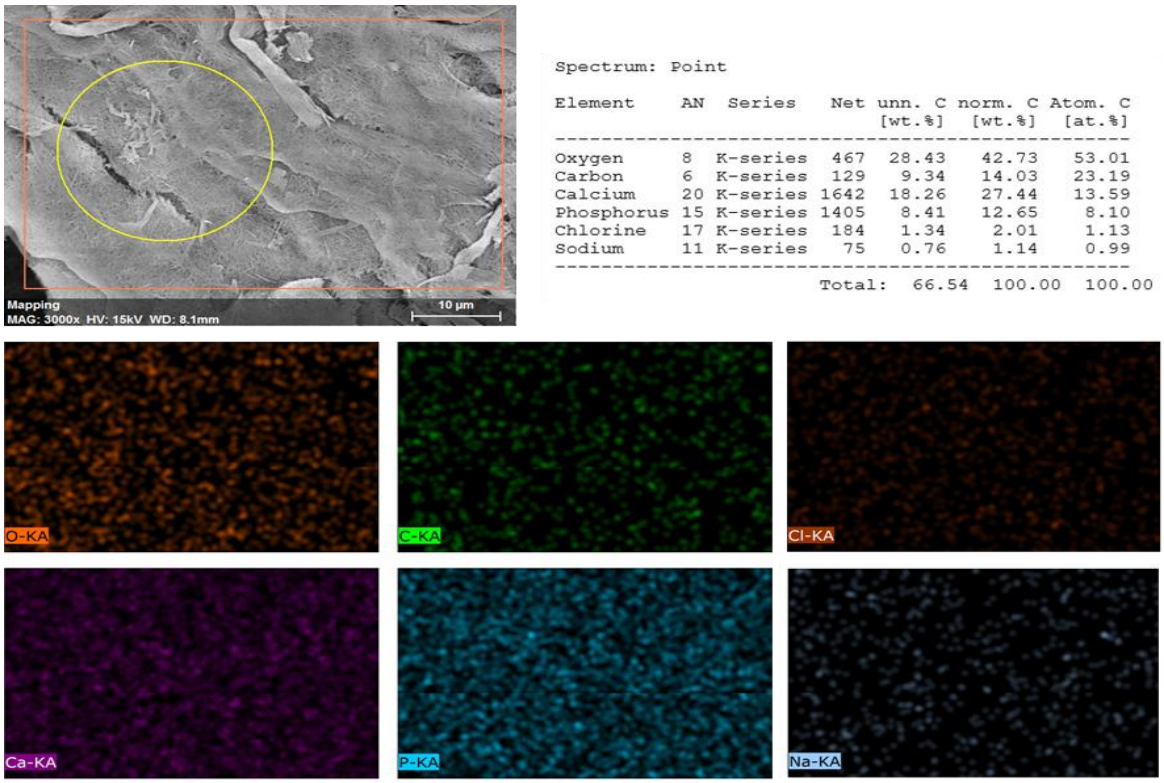

Spectrum: Point

Element	AN	Series	Net	unn. C [wt.%]	norm. C [wt.%]	Atom. C [at.%]
Oxygen	8	K-series	467	28.43	42.73	53.01
Carbon	6	K-series	129	9.34	14.03	23.19
Calcium	20	K-series	1642	18.26	27.44	13.59
Phosphorus	15	K-series	1405	8.41	12.65	8.10
Chlorine	17	K-series	184	1.34	2.01	1.13
Sodium	11	K-series	75	0.76	1.14	0.99
		Total:		66.54	100.00	100.00

Figure B.5.2.19 - Quantification and mapping EDS analysis of the H85C15 cryogel after 14 days in SBF

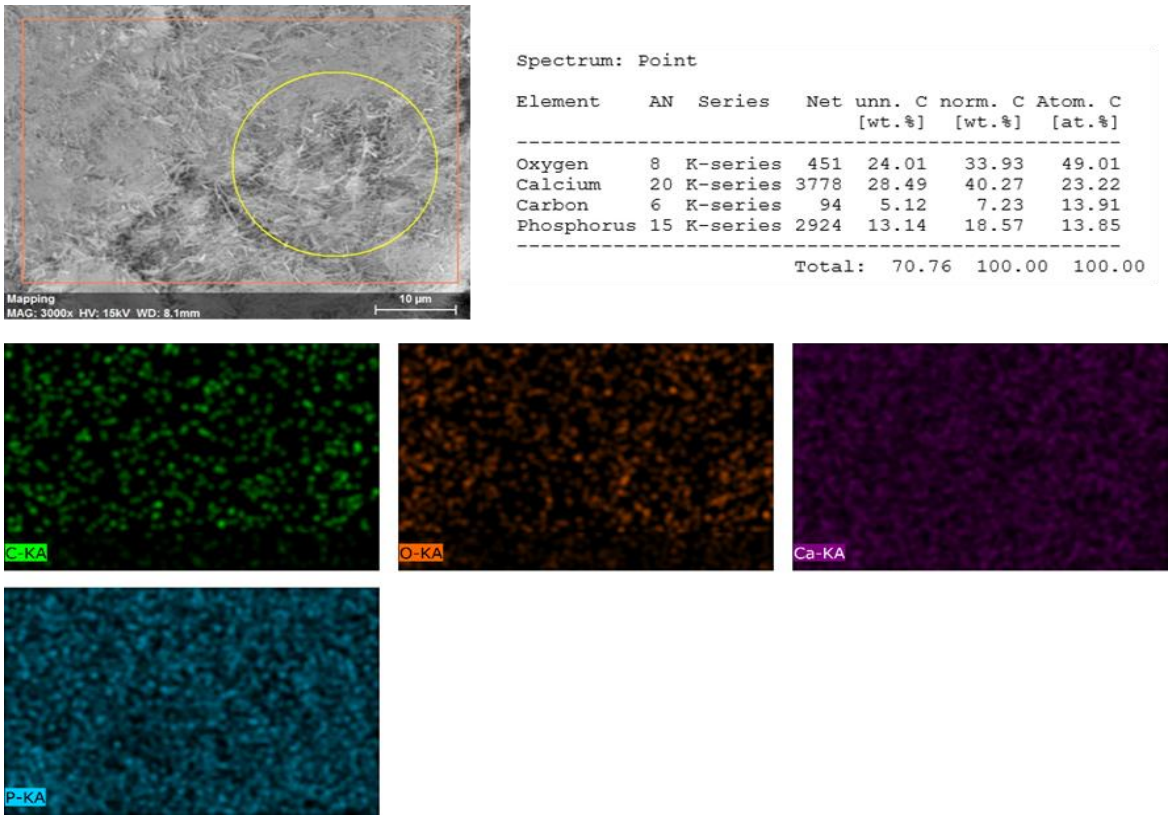

Spectrum: Point

Element	AN	Series	Net	unn. C [wt.%]	norm. C [wt.%]	Atom. C [at.%]
Oxygen	8	K-series	451	24.01	33.93	49.01
Calcium	20	K-series	3778	28.49	40.27	23.22
Carbon	6	K-series	94	5.12	7.23	13.91
Phosphorus	15	K-series	2924	13.14	18.57	13.85
		Total:		70.76	100.00	100.00

Figure B.5.2.20 - Quantification and mapping EDS analysis of the H100 cryogel after 14 days in SBF

B.6 Mechanical tests – Young's Modulus

Table B.6.1 - Young's Modulus and the corresponding average of each one of the 5 samples tested for each cryogel

	C100	H50C50	H75B10C15	H80B5C15	H85C15
Young's Modulus (KPa)	18.2	18.3	5.5	5.8	10.6
	18.6	17.3	3.5	7.6	13.3
	22.3	16.2	3.7	7.5	12.8
	24.5	14.7	4.6	6.6	9.0
	25.5	25.5	5.0	6.3	8.9
Mean	21.8 ± 3.0	18.4 ± 3.7	4.5 ± 0.8	6.8 ± 0.7	10.9 ± 1.8

B.7 Binocular stereo microscope

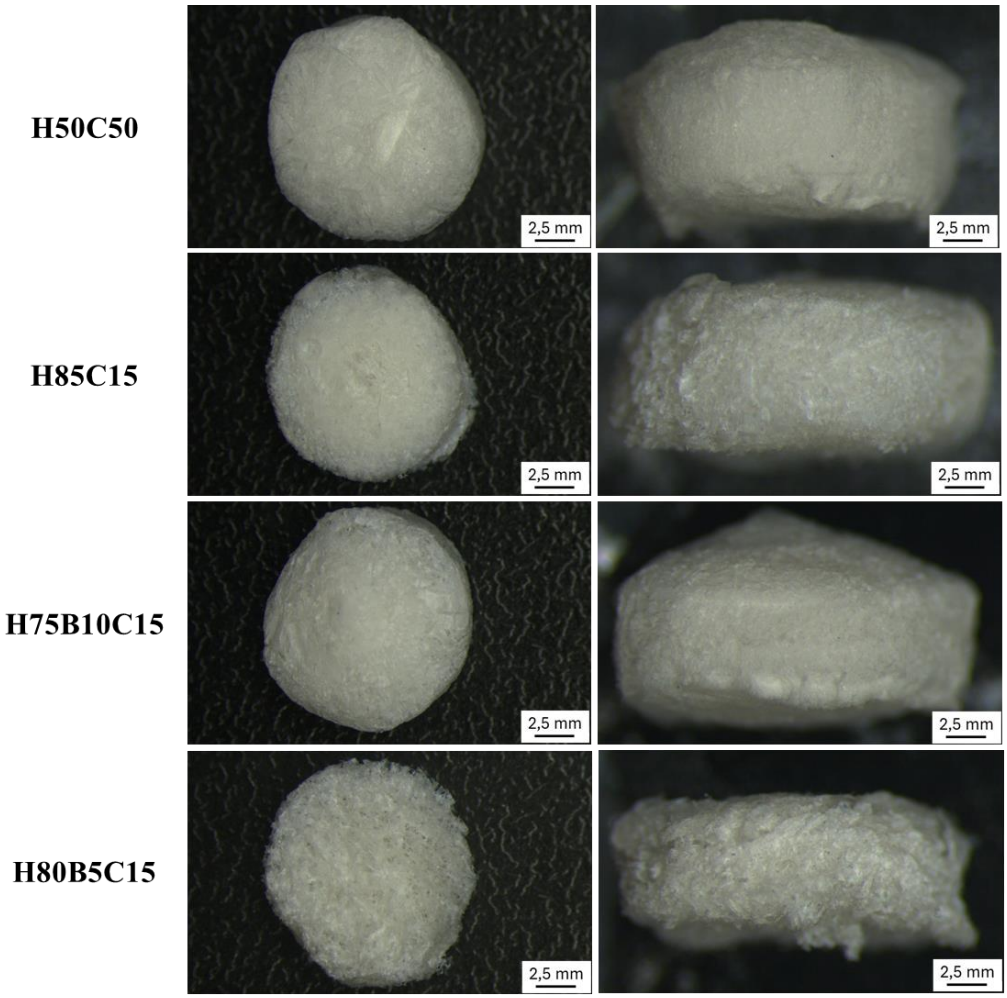

Figure B.7.1 - Cryogels visualized with binocular stereo microscope.